ABSTRACT

Title of Dissertation: A GAS-INJECTION NEGATIVE ION SOURCE FOR ACCELERATOR MASS SPECTROMETRY

Scott Joseph Tumey, Doctor of Philosophy, 2004

Dissertation directed by: Professor Alice C. Mignerey
Department of Chemistry & Biochemistry

Accelerator mass spectrometry is an ultra-sensitive isotopic analysis technique that allows for the determination of rare long-lived radionuclides such as radiocarbon. Historically, the technique has required that samples be processed into graphite prior to analysis. The processing is time and labor intensive and limits the technique due to contamination. There has been recent interest to develop an ion source that would allow direct injection of gaseous samples, thus eliminating the processing. Previous attempts to build such an ion source have been limited by low mass usage efficiency and severe memory effects. This dissertation describes the development of a plasma negative ion source that allows direct injection of gaseous material. This ion source was able to produce a $^{12}C^-$ ion beam of approximately 4.5 μA from carbon dioxide. This beam intensity is lower than both of the competing designs. However, this ion source was able to operate with a mass efficiency of nearly 0.15% which exceeds one of the competing designs. It was also free from significant memory effects which plagued the other competing design. There are many improvements to the design of this ion source that would further enhance its performance. These results are promising and show that this type of ion source could be used effectively in an accelerator mass spectrometry system.

A GAS INJECTION NEGATIVE ION SOURCE FOR ACCELERATOR MASS SPECTROMETRY

By

Scott Joseph Tumey

Dissertation submitted to the Faculty of the Graduate School of the
University of Maryland, College Park in partial fulfillment
of the requirements for the degree of
Doctor of Philosophy
2004

Advisory Committee:

Professor Alice C. Mignerey, Chair
Professor William B. Walters
Professor Robert A. Walker
Professor George R. Helz
Professor Phillip G. Roos

Dedication

I am sure that the single most common recipients of doctoral dissertation dedications are parents, and with good reason. My parents have unquestionably had the greatest influence on my life and I would not have been able to complete this doctoral dissertation without their many years of love and support. I therefore dedicate this work to them and hope that it brings them great joy to know that they can finally contact my first grade teacher Mrs. Childs and tell her how wrong she was.

Acknowledgements

As every Ph.D. is well aware, a doctoral dissertation is the culmination of years of toil and sacrifice. The doctoral candidate is not alone in this endeavor, however. For this reason, I would like to acknowledge the individuals who have assisted and guided me throughout this long journey. Alice Mignerey has been my advisor and her patience and willingness to allow me to work independently have been critical to my success. Ken Grabowski provided direction to my research and insight into the multidisciplinary nature of scientific research. Finally, David Knies's technical instruction has been invaluable to me and it is not an understatement to say that without it, I would never have been able to complete this research.

Table of Contents

List of Tables

List of Figures

I Introduction

I.1 Accelerator Mass Spectrometry

I.1.A Background

Accelerator mass spectrometry (AMS) is an ultra-sensitive analysis technique that allows direct measurement of both radioactive and stable isotopes. As in conventional mass spectrometry (MS), atoms are extracted from a sample, ionized, accelerated, separated by mass, charge, and energy, and finally detected. The primary difference between AMS and MS is the use of a tandem accelerator, which provides orders of magnitude greater acceleration. This acceleration provides interference attenuation via molecular break-up in the stripper canal, as well as nuclear energy loss techniques of separation and detection. Consequently, AMS can provide up to a factor of 10^5 lower detection limits than MS, which allows for isotopic determination of rare long-lived radionuclides (1).

The most important application of AMS has been radiocarbon dating where it has replaced decay counting as the primary analysis tool in many applications (2, 3). In the AMS technique, individual atoms are counted rather than the decay events of ^{14}C. This approach suffers less from background, and therefore is inherently more sensitive. Additionally, less material is required for AMS. Whereas decay counting requires half a day to attain acceptable statistics from a gram of modern carbon, AMS can provide the same precision in a matter of minutes with only a few milligrams of modern carbon. This increase in throughput and sensitivity has revolutionized the radiocarbon field and expanded it into areas beyond the traditional role in archaeology. Radiocarbon analysis is now an important tool in such diverse disciplines as environmental science (4-

11) and pharmacology (11-17). The technique has been used in such notable applications as the dating of the Shroud of Turin (18) and to authenticate historical documents revealing a new version of the conquest of Peru by Pizarro in the early 1530s (19).

Besides its widespread use in determination of radiocarbon, AMS has been applied to a wide range of other isotopes. Argon, iodine, and chlorine have been used in tracing both ocean and ground waters (20, 21). Exposure age of rocks and sediments has been performed using beryllium (22, 23). Uranium and plutonium isotope ratios can be determined by AMS for nuclear weapons non-proliferation (24, 25). The AMS technique has also been used to support nuclear physics by providing tritium depth profiling of samples from fusion experiments (26) and for determination of the cosmic radioactivity of titanium (27).

I.1.B Technique

A block diagram of the AMS system at the Naval Research Laboratory (NRL) (28-30) is shown in Figure I-1. While this system has some components which make it unique (31-33), the general operation is typical of most AMS facilities. The major components of the system are the ion source, the pretzel magnet, the tandem accelerator, the three-degree electrostatic bend (TDB), the electrostatic analyzer (ESA), and finally the split-pole mass spectrograph. Since the power of AMS lies in the use of a tandem accelerator, the ion source used in AMS systems must be able to provide negative ions. More specific details regarding ion sources are discussed in Section I.2.

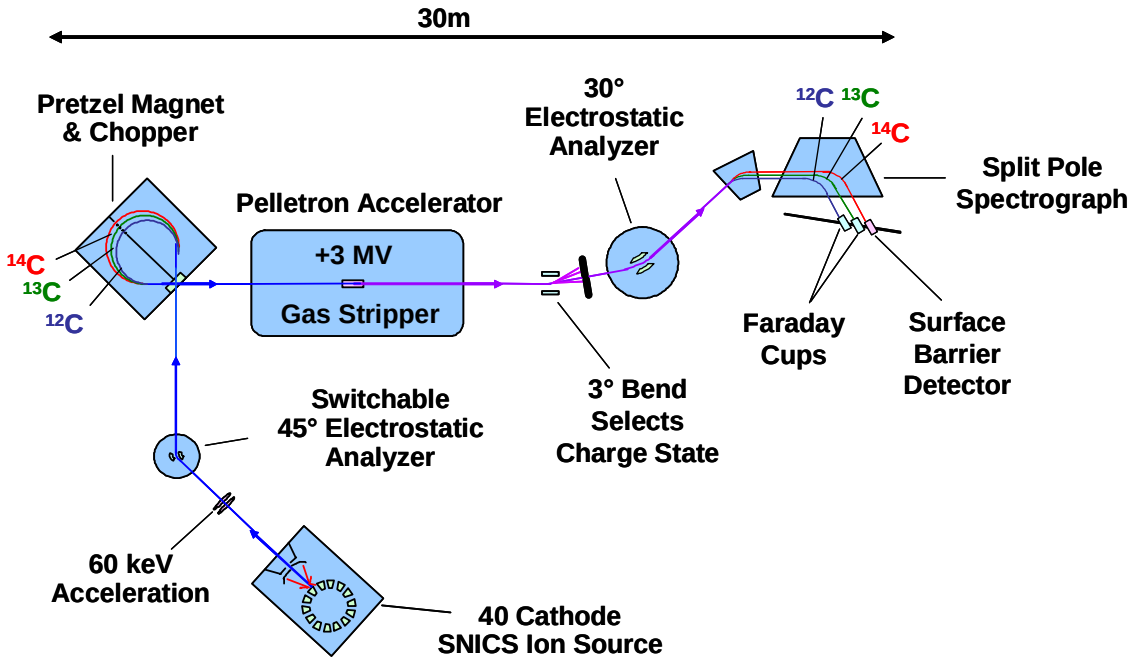

Figure I-1. The NRL AMS system configured for ^{14}C analysis

The beam extracted from the ion source is composed of atomic and molecular species of the elements in the sample. Even though the targets loaded into the ion source are processed to purify the element of interest, there are still ubiquitous contaminants that end up in the sample. For example, in radiocarbon AMS samples are processed into graphite prior to analysis. This graphite typically contains large amounts of oxygen and, to a lesser extent, hydrogen and nitrogen. It is undesirable to inject all of these species into the accelerator due to the loading of the terminal that would occur as a result. Additionally, break up of molecules in the stripper canal of the accelerator can produce look-alike beams that would interfere with the measurement of the isotopes of interest. For this reason, the pretzel magnet is used to filter out these undesirable species.

The trajectory of ions through the pretzel magnet is shown in Figure I-2. The ions are dispersed through a radius r according to their mass m, charge q, and energy E by:

$$B^2 r^2 = k \frac{mE}{q^2}, \tag{I-1}$$

where B is the magnetic field strength, and k is a constant defined by the geometry of the magnet. At this point, however, all of the ions have nearly the same energy, and almost all have a charge of negative one. Therefore, the pretzel magnet is merely acting as a pure mass separator. A mask placed along the magnet's axis of symmetry can effectively block all masses except those to be injected into the accelerator, which in the case of carbon are masses 12, 13, and 14. The mass separated ion beams are then recombined for injection into the tandem accelerator. The resulting beam is free of interferences from oxygen and hydrogen, as well as the hydrides of oxygen and nitrogen. It is important to note that the hydrides of ^{12}C and ^{13}C, as well as the dihydride of ^{12}C are not filtered out.

The ion beam is then injected into the tandem accelerator, so called because there are two stages of acceleration. The terminal of the accelerator is charged to a high positive potential, V_t, typically 3 MV for the NRL machine. Negative ions injected with energy E_{inj} are accelerated to the terminal and then stripped of one or more electrons in the stripper canal. The stripper canal is also responsible for molecular breakup, with the energy being elastically distributed between the molecule fragments. The resulting positive ions are accelerated away from the terminal based on their charge and end up with an energy E_{ext} given by:

$$E_{ext} = \frac{m_{out}}{m_{in}}\left(E_{inj} + V_t e\right) + qV_t e\,, \tag{I-2}$$

where m_{out} is the extracted ion mass, m_{in} is the injected ion mass, and e is the charge of an electron. The resulting ion beam has a charge state distribution that is determined by the mass and density of the stripping material, and the mass and energy of the incident ion.

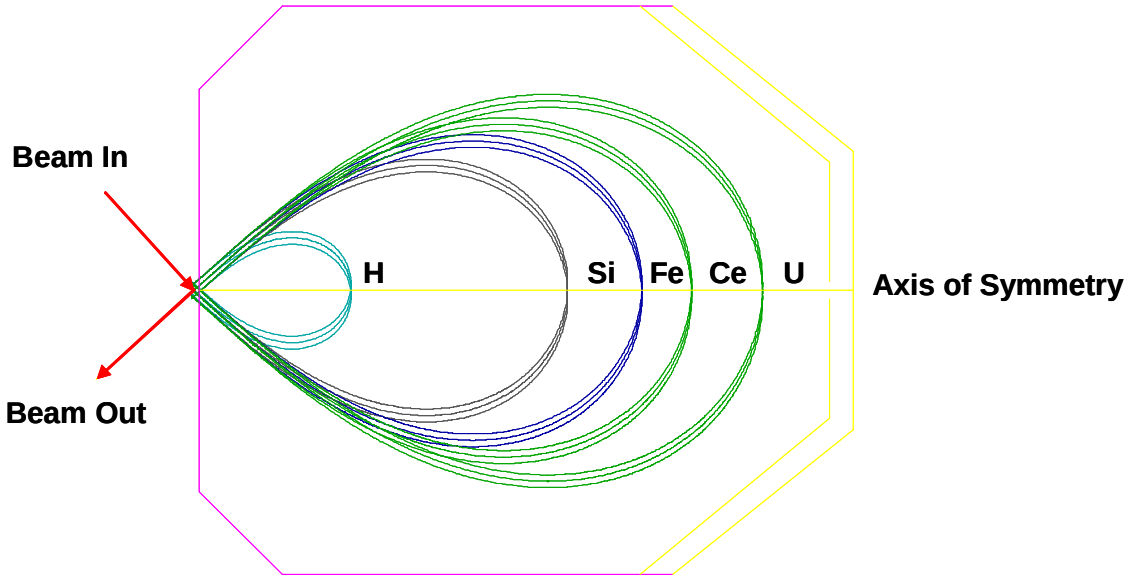

Figure I-2. The trajectories of ions through the NRL pretzel magnet. The plot was generated by the ion beam modeling software package SIMION (34).

The next element in the NRL AMS system is the three-degree bend, which allows for a specific charge state to be selected before being injected into the electrostatic analyzer. As mentioned, the ion beam extracted from the accelerator is made up of several charge states. Ions are dispersed by an electrostatic field as follows:

$$r = k_2 \frac{E}{q}\,. \tag{I-3}$$

Since it is a high resolution device, it is important to filter out the unwanted charge states before the ESA. These unwanted charge states would strike the electrodes of the ESA and impair its ability to hold voltage. By dumping the unwanted charge states onto water-cooled slits before the ESA, this problem is avoided.

While the TDB selects a single charge state, it lacks the resolution to filter out breakup fragments of ^{13}CH and $^{12}CH_2$. Under normal operating conditions (E_{inj}=65 keV, V_t=3 MV, q=3), it requires an energy resolution (E/ΔE) of roughly 55 to distinguish between ^{14}C and ^{13}C from the breakup of ^{13}CH. The ESA has an energy resolution of approximately 300, and is more than capable of removing these unwanted species. This step is important, because although these other charge states would show up at a different location along the focal plane of the split-pole, they could still cause stray signals in the ^{14}C detector from scattering events. Since $^{14}C/^{12}C$ ratio in modern carbon is about 1 part in 10^{12}, even a small fraction of scattering events from these other charge states would raise the background enough to interfere substantially with the measurement.

The final component of the NRL AMS system is the split-pole. As in the pretzel magnet, ions are dispersed according to Equation I-1, and the trajectories can be seen in Figure I-3. By placing a detector array along the focal plane, accurate measurements of both the $^{14}C/^{12}C$ and $^{13}C/^{12}C$ ratios can be made. The detector array consists of two electrically and geometrically suppressed Faraday cups, for measurement of the stable isotopes, and a surface barrier detector, for detection of ^{14}C. Despite the great pains to filter out all unwanted species from the ion beam, it is possible for some interferences to end up in the ^{14}C detector (e.g. isobaric interferences). By using a surface barrier detector equipped with a foil, some of the interfering counts can be rejected by the difference in energy loss through the foil.

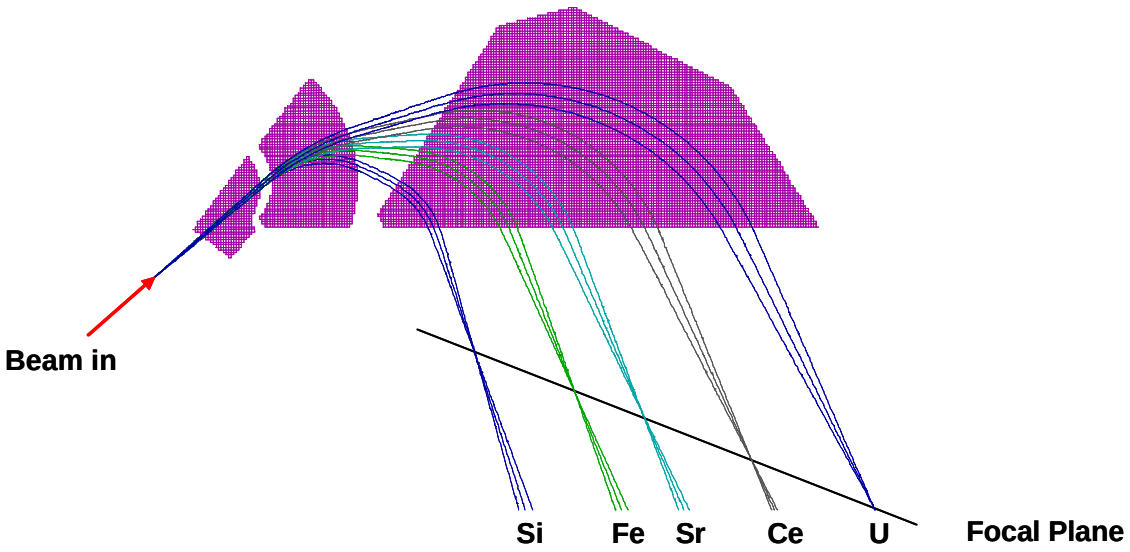

Figure I-3. The trajectories of ions through the NRL split-pole mass spectrograph. The plot was generated by the ion beam modeling software package SIMION (34).

I.2 Traditional AMS Ion Source

I.2.A Background

Historically, AMS systems have almost exclusively employed cesium sputter ion sources, the reason being that this type of ion source is capable of producing high quality, intense beams of negative ions (35-37). Also, most first generation AMS systems shared beam time with nuclear physics labs, which often used cesium sputter sources. While these ion sources performed well, there were some limitations that have spawned interest in the AMS community to develop a better ion source in hopes of improving the capabilities of the technique and opening up new applications (38-40).

I.2.B Theory of Operation

The general operation of a traditional cesium sputter ion source is illustrated in Figure I-4. A solid sample is packed into a hollow cathode and the cathode is inserted into the source chamber. Cesium is introduced to the chamber from a reservoir and thermally ionized by a resistively heated ionizer. The positive ions are

focused onto the negatively biased cathode surface and sample material is sputtered away. The sputtered material is made up of atoms and molecules, most of which are neutral or cationic; however, a small fraction come off as negative ions. The negative ion yield is enhanced by condensation of residual cesium vapor on the sample surface, which lowers the work function. The negative ions are repelled from the cathode surface and extracted from the ion source.

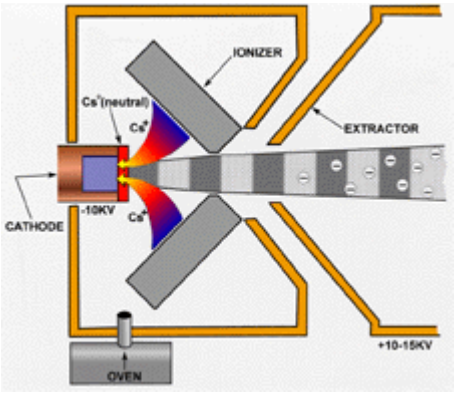

Figure I-4. The general operation of a traditional cesium sputter ion source (41).

I.2.C Interest in a Gas-fed AMS Ion Source

The range of different types of samples that can be analyzed by AMS is as wide as the range of fields that use the technique. Some examples are wood for dendrochronology (42), bone for archaeology (43), water (44), sediment (6), and shells (45) for oceanography, and blood and urine samples for medical applications (12, 13, 15, 16). Fluid samples are incompatible with a traditional cesium sputter source, and therefore require chemical processing in order to extract the carbon and convert it to solid form (46-50). Even solid samples require processing to remove impurities and concentrate their carbon. This processing maximizes negative ion production, as well as makes the beam output more consistent between different samples. This leads to more reproducible analyses.

The first step in processing is typically a pretreatment step. Pretreatment can be as simple as an acid-alkaline-acid wash to remove inorganic carbon from organic matter, but can also include more complicated steps in order to remove compounds that could poison the rest of the processing. Once pretreated, carbon must be liberated from the sample, typically by combustion, or reaction with acid. It is important that this liberation phase be carried to completion in order to avoid isotopic fractionation. As a result, this step can take many hours. The resulting CO_2 must then be purified by cryogenic distillation to remove byproducts of the liberation stage (e.g. water vapor). Finally, the CO_2 is reduced to graphite using a catalyst, typically iron. Again, this process must be carried to completion to avoid isotopic fractionation.

Processing of samples for AMS is a time and labor intensive process. By replacing the traditional cesium sputter source with an ion source that accepts gaseous material, a significant time savings could be gained. Obviously, liberation of carbon from solid samples would be necessary, but the resulting CO_2 could be injected directly into the ion source, negating the need for graphitization. The advantage is even greater with liquid samples that could simply be vaporized and fed into the ion source. The ultimate goal of a gas-fed ion source is the capability to directly couple a gas (GC) or even liquid (LC) chromatograph to an AMS system (38, 39, 40, 51-53). Such a device would be akin to a GC-MS or LC-MS system, and would allow for real-time analysis of multi-component samples. Quite often samples are a complex mixture of compounds and each component may have a different carbon source. The ability to date each individual component could provide more insight into the nature of the sample than a bulk analysis of the entire sample.

Besides the convenience of throughput enhancement, there is another important reason for pursuing the development of a gas-fed ion source for AMS. Radiocarbon concentrations are typically expressed as a fraction of modern carbon; 50% modern is equivalent to one half-life, 25% modern to two half-lives, etc. The current limit of detection for state-of-the-art AMS systems is approximately 2‰ (30, 54-58), which corresponds to an age of about 51,000 years. This limit is primarily due to the chemical processing necessary with a traditional cesium sputter source. At NRL, graphite produced from petroleum products is used as a machine blank. Analysis of this material yields noticeably lower radiocarbon content than the same material that has undergone chemical processing. By eliminating the need for chemical processing, a gas-fed ion source could lower the detection limit of AMS measurements and push the technique to allow for analysis of older samples.

II Ion Sources

II.1 Design Considerations for a Gas-fed AMS Ion Source

II.1.A Beam Intensity

There are many factors to consider in the design of a gas injection negative ion source for AMS. Since AMS users demand high sample throughput, the most important requirement is the ability of the ion source to produce intense beams. For traditional cesium sputter sources, beam currents of 100-200 μA are typical. This allows for 1% counting statistics (i.e. 10,000 counts) to be obtained from modern material in roughly one minute. It is important that any gas-fed ion source be capable of producing beam intensities near this range in order to meet the throughput demands. Also, in order for a GC-AMS system to be successful, the AMS analysis time must be similar to the GC retention time.

II.1.B Beam Quality

High beam intensity is of little use if the quality of the beam is poor. Beam quality refers to the transportability of the beam and is measured by the emittance of the beam. At a particular point, an ion beam can be defined by its displacement (x and y) and slope (x' and y') in both of the transverse beam axes. A plot of slope versus displacement in one of the beam axes yields an ellipse. The area of this ellipse is referred to as the emittance of the ion beam. According to Liouville's theorem, the emittance of an ion beam is invariant along its trajectory if the forces on the beam are conservative. Ion beams with high emittance are difficult to transport through the many components of an AMS system. In most systems, the limiting aperture is the stripper canal of the

accelerator, so the emittance of the ion source can not be greater than the acceptance of the accelerator in order to maximize beam transmission.

II.1.C Mass Efficiency

The next important consideration is the mass efficiency of an ion source. Due to the high activation barrier for electron attachment, traditional negative ion sources produce only a few negative ions for every hundred molecules or atoms of analyte introduced into the source. For modern material, this means that at least 4 μg of graphite is required to yield sufficient $^{14}C^-$ ions to provide 1% counting statistics. This number increases to around 12 μg when machine transmission is taken into account. For older samples, even more material is required. For some applications, obtaining an adequate amount of material presents little challenge. More and more, however, AMS is being applied to very complex problems where sample material is at a premium. One example of this is the use of biomarkers in the study of carbon sequestration by the formation of methane hydrates in ocean sediments (6, 58). In order to be really useful, any gas-fed ion source design must maximize the mass usage efficiency in order to allow analysis of small samples.

II.1.D Memory Effects

Probably the toughest aspect to address when designing an ion source is the time sample material spends in the ion source. To achieve maximum gas efficiency it is desirable for analytes to spend as much time in the source as possible. However, residual material from one sample can interfere with the analysis of subsequent samples. This phenomenon is known as a memory effect and can be quite severe when the samples of interest have widely different radiocarbon concentrations. A successful gas-fed ion

source design needs to balance the benefits of increased negative ion production with the undesirable memory effects that occur with a long sample residence time.

II.2 Existing Gas-fed AMS Ion Source Designs

II.2.A Hybrid Cesium Sputter Source

Since it is the predominant type of ion source used in AMS, it makes sense that the first design for a gas-fed ion source was a modified version of a cesium sputter source. A similar design was developed both at Oxford (59-61), and by a company in Boston called Newton Scientific (38, 39, 51). Gas injection was accomplished by fitting a standard cathode with a titanium frit through which gas could flow. Sample passing through the frit was ionized by the incident cesium beam. Carbon dioxide has a relatively high negative ion yield so samples were first passed through an oxidation furnace before being fed into the ion source. Not only did this maximize source efficiency, but it also produced more consistent beam output. Ionization efficiency was also enhanced by virtue of the adsorption affinity of titanium for CO_2, thus increasing the residence time of analyte on the cathode surface.

While the hybrid cesium sputter source design was successful in producing negative carbon beams for AMS, it suffered from some critical limitations. First, the beam intensity was about a factor of ten lower than the output of a traditional cesium sputter source. This reduced output negated the time saved by bypassing the graphitization process required for traditional cesium sputter ion sources. The more significant limitation of this design was the pervasive memory effect that occurred as sample material built up on the titanium frit. This effect is illustrated in Figure II-1. This background increase interfered with the measurement of older samples following near

modern samples. Since the standards used in radiocarbon measurements are actually above modern, analysis of old samples was virtually impossible. Consequently, this ion source design has been limited to qualitative applications dealing with samples of comparable ages.

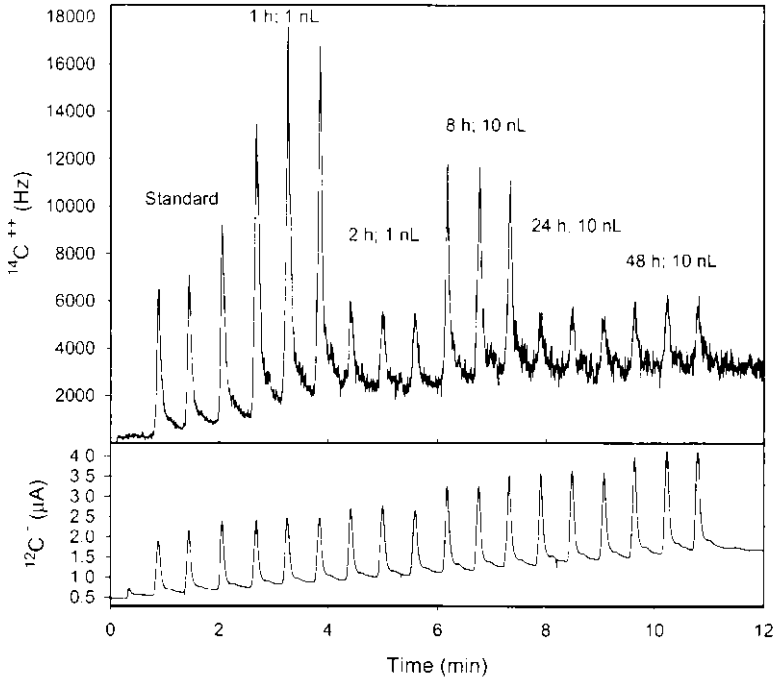

Figure II-1. The memory effects of the Newton Scientific gas hybrid cesium sputter source. The top plot shows the ^{14}C count rate in the final detector, while the bottom plot shows the ^{12}C current measured in an off axis faraday cup before the accelerator. The peaks correspond to injections of samples of male rat plasma spiked with a ^{14}C tracer and collected at various time intervals (52).

National Electrostatics Corporation addressed the memory effect problem experienced in the hybrid cesium sputter source by modifying its multi-cathode design in a similar manner (62). Since this ion source employed a wheel of forty cathodes, it was possible to advance to a fresh cathode between each sample. This approach was a definite improvement over the single-cathode design; however it still experienced some memory effects. As samples were fed into the ion source, not all of the material was ionized by the cesium beam and this residual gas adsorbed on other surfaces in the source

chamber. Adsorbed gas on the other cathodes of the wheel caused a noticeable memory effect. This approach also presented a practical limitation due to the finite number of cathodes available on a single wheel. Measurement of many different components of a complex sample was problematic. Finally, the ion beam output of this source was still below that obtained from a traditional cesium sputter source.

II.2.B Electron Cyclotron Resonance Ion Source

The cesium sputter sources discussed were direct sources for negative ions. Since intense positive ion beams are inherently easier to produce, an alternative strategy for producing a negative ion beam was to use a positive ion source coupled with a charge exchange cell. This strategy was employed by the Woods Hole Oceanographic Institute using an electron cyclotron resonance (ECR) type ion source (63-67). Microwaves tuned to the ECR frequency cause ionization of sample gas in the source chamber. The resulting electrons were heated by absorption of these microwaves and ionized additional gas molecules via electron bombardment. Positive ion beams of over 1 mA were easily obtainable from this ion source. The positive ion beam was then fed into a charge exchange cell filled with an electropositive vapor, such as magnesium. A fraction of the positive ions stripped two electrons from the vapor and formed negative ions. This charge exchange efficiency was limited to about 10%, which results in a negative ion beam that was comparable to that obtained from a traditional cesium sputter source.

While the ECR source was able to match the beam intensity of a traditional cesium sputter source, it suffered from other limitations. Unlike the hybrid cesium sputter source which suffered from a chronic memory effect, the ECR source

seemed to be free from this effect. However, it had a very long material consumption time constant, as shown in Figure II-2. This long decay time made coupling of a GC to this ion source nearly impossible. Another limitation of this ion source was the very low mass efficiency of 0.09%, which was almost 20 times lower than the efficiency of cesium sputter sources. Consequently, the ECR ion source was limited to applications where small samples are not required.

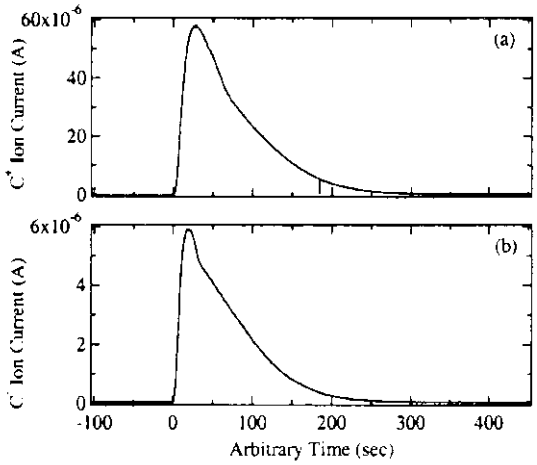

Figure II-2. Positive (a) and negative (b) ^{12}C ion current peaks resulting from injections of CO_2 into the Woods Hole ECR ion source. The scales of the y-axes differ by a factor of ten reflecting the charge exchange efficiency (63).

II.3 Multi-cusp Ion Sources

II.3.A History

Multi-cusp ion sources have been used for over 20 years in fusion research because of their ability to produce very intense beams of H^- (68-76). These ion sources are typically very large, using gridded extraction schemes with active areas of tens of square centimeters. Recently, attempts have been made to compact the design for use in accelerator applications such as ion implantation, as well as in industrial applications like ion beam lithography (77-80). While uses of multi-cusp ion sources are expanding, they have almost exclusively been used with hydrogen.

II.3.B Theory of Operation

Multi-cusp ion sources are part of a larger family of sources known as volume ion sources, so called because ionization occurs in the volume of a plasma discharge. There are several mechanisms for plasma generation but the simplest is through thermionic emission of electrons from a hot cathode. When sufficient current is passed through a filament electrons boil off the surface. The electron yield J_e is given by the Richardson Equation (81):

$$J_e = \frac{4\pi m_e k^2 e}{h^3} T^2 e^{-\frac{\Phi}{kT}}, \qquad \text{(II-1)}$$

where m_e is the electron rest mass, k is the Boltzmann constant, e is the electron charge, h is the Planck constant, T is the filament temperature, and Φ is the work function of the filament material. These primary electrons collide with gaseous species in the source chamber resulting in ionization, most often by knocking off an outer shell electron. Ionization is enhanced by a positively biased electrode which acts as an anode to which the electrons are accelerated. Once sufficient ionization has occurred, typically 1-2%, the electrons and ions are effectively shielded from external electric forces and a plasma discharge is created. Due to the difference in mobility between the ions and electrons, a boundary layer forms that surrounds the plasma. Unlike in the plasma ions and electrons in this boundary layer have some interaction with external forces, and it is from this plasma sheath that ions can be extracted.

The distinguishing feature of the multi-cusp type ion source is the use of permanent magnets to confine the plasma. While the electrons in a plasma discharge are effectively shielded from external electric forces, they are still influenced by magnetic

field lines. By placing an array of permanent magnets around the source chamber, the plasma is confined to a specific geometry determined by the arrangement of the magnets. The most widely used configuration is an alternating multi-pole geometry, as illustrated in Figure II-3. In this arrangement, the field lines form cusps that surround the source chamber. Since the electron gyroradius is inversely proportional to the field strength, electrons closer to the center of the chamber have a longer path length than those at the edge. As a result, they spend more time in the plasma before being lost to the chamber, or the anode. The result is an increased plasma density for a fixed filament output, which leads to a higher ionization efficiency.

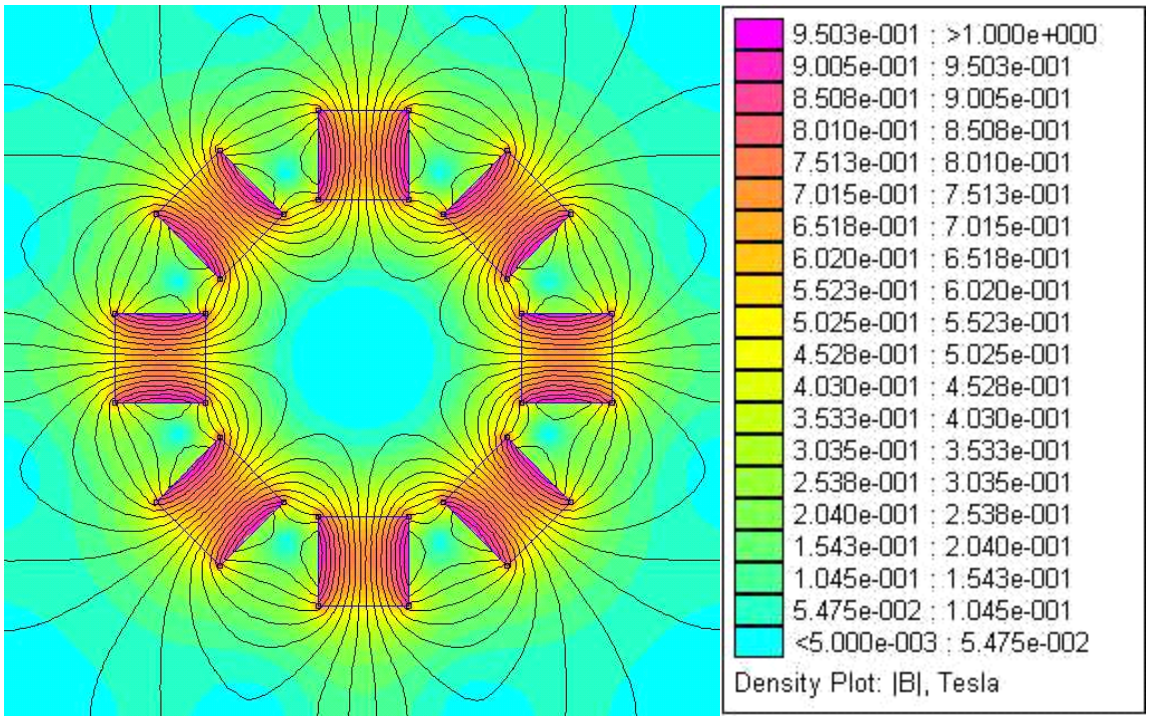

Figure II-3. The magnetic field lines and field density in a multi-cusp arrangement. The plot was generated by the magnetic analysis package FEMM (v3.0)

Since only the ions in the plasma sheath facing the extraction aperture are extracted from the ion source, the extraction efficiency can be enhanced by concentrating ion production in this region. The most effective method for accomplishing this is the

use of a magnetic filter which is composed of a weak magnetic field oriented perpendicular to the beam axis (76, 82-84). To understand the functionality of this filter, it is important to study the primary mechanism for negative ion production (68, 76, 85, 86), which is dissociative attachment:

$$H_2 + e \rightarrow H^- + H \,. \qquad \text{(II-2)}$$

The cross section for dissociative attachment is quite low for hydrogen in the ground state, but achieves a strong peak when the molecule is in a vibrationally excited state, typically $\upsilon > 5$. The cross section for the excitation reaction

$$H_2 + e \rightarrow H_2^* + e' \qquad \text{(II-3)}$$

has a peak at an electron energy of about 40 eV (81), while the dissociative attachment cross section peaks at an electron energy of about 1 eV. The purpose of the magnetic filter is to separate the source chamber into an excitation region, and an extraction region. High energy electrons can not diffuse through the filter and are concentrated in the excitation region. The colder electrons, as well as the vibrationally excited molecules, can pass through the filter allowing most of the dissociative attachment to occur on the other side. By positioning the filter very close to the extraction aperture, extraction of negative ions is maximized.

Another important feature of the multi-cusp ion sources is the use of cesium (68, 86-88). While the exact mechanisms are not well understood, it has been shown that a small amount of cesium introduced into the source chamber can increase the negative ion yield by nearly a factor of ten. This enhancement is coupled with an increase in plasma potential, a decrease in plasma temperature, as well as an increase in

the relative density, $\frac{n_{H^-}}{n_e}$, in the extraction region. The drawback to using cesium is the reduction in the service life of the source as cesium deposits will tend to short out electrodes. However, since cesium is used as a seed, rather than being consumed as is the case with the cesium sputter sources described above, this drawback is rather small.

II.3.C Typical Performance

Multi-cusp ion sources are widely used because of their ability to deliver very intense beams of H^-, typically in the range of hundreds of milliamps up to tens of amps (81, 89). It is important to note that these sources have very large extraction apertures so the size of the extracted beam is on the order of a several centimeters. Beams of this size are difficult to transport through an accelerator, which typically has a limiting aperture of 6-8 mm. So the more important measure of the ion source output is the current density of the beam. Multi-cusp ion sources are capable of providing current densities well over 100 mA/cm^2. For a nominal aperture size (2 mm), this would yield roughly a 3 mA beam, which is over a factor of 20 higher than the maximum beams obtained from cesium sputter sources. Additionally, since ions are ideally extracted from the flat, uniform, surface of the plasma sheath, the emittance of the ion beam is generally lower than from a cesium sputter source, which suffers from geometrical effects as the shape of the cathode surface is eroded by sputtering.

Another attractive feature of the multi-cusp sources is their gas efficiency, which has been reported to be as much as 75% (81, 89). This is an order of magnitude higher than the efficiency of a cesium sputter source. In addition to the ability to analyze samples more quickly because of increased beam intensity, multi-cusp ion sources have

the potential to dramatically reduce the amount of sample necessary to even perform a measurement. For these reasons, multi-cusp ion sources seem to be a strong candidate for a gas-fed ion source for AMS.

III Prototype

III.1 Ion Source

III.1.A Chamber

A multi-cusp type negative ion source as described in Section II.3 was constructed for use in the NRL AMS system (93). While this type ion source has been used for over 20 years, it has not been applied to an AMS system before. Consequently, it was important to examine the special requirements that influenced the specific construction of the NRL plasma ion source. First, in order to minimize memory effects caused by residual analyte remaining in a plasma ion source, the source chamber volume should be as small as possible.

Another important reason for making the source chamber compact is the maximization of negative ion extraction efficiency, and therefore mass usage efficiency. Since ions from a plasma ion source are extracted only from the surface of the plasma sheath that faces the extraction aperture on the plasma electrode, the extraction aperture to chamber diameter ratio must be as large as possible. The extraction aperture in a multi-cusp ion source determines both the emittance of the extracted ion beam, as well as the gas flow rate from the ion source. If the aperture is too large, the emittance of the extracted beam will exceeded the acceptance of the accelerator. This problem would be compounded further by the beam scattering that would occur due to the increased pressure in the beamline caused by the increased gas load. As a result, the aperture diameter has a practical upper limit for this type ion source to be used in an AMS system. Additionally, the length of the source chamber should be as short as possible. This reduces the distance that negative ions formed in the center of the plasma must travel

before reaching the extraction region, thus lowering the likelihood of their destruction. For these reasons, the both the diameter and the length of the source chamber of the NRL plasma ion source was minimized.

Besides the dimensions of the chamber, the mechanical connection to the AMS system was also considered. Most multi-cusp ion sources operate with a gas pressure between 1 and 100 mTorr, so a UHV type flange is unnecessary. However, the plasma generates an appreciable thermal load, so an o-ring seal, which would be susceptible to heat damage, is inappropriate. For this reason, a standard 2.75" copper gasket flanged (Del-Seal) full nipple was selected as the source chamber for the NRL plasma ion source and is shown in Figure III-1. The chamber was constructed from 316-stainless steel, was 3.5" long, and had one rotateable flange and one fixed flange.

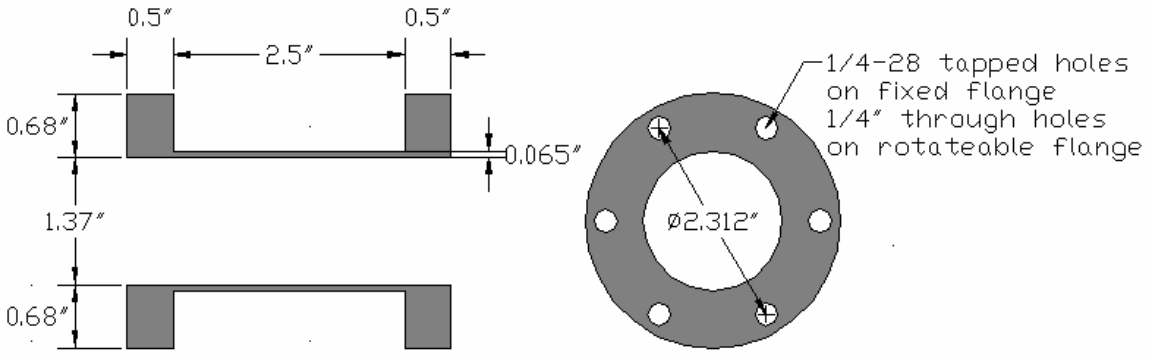

Figure III-1. A side and front view of the chamber selected for the NRL ion source.

III.1.B Filament

Since the NRL plasma ion source was a prototype, and had to be built on a very limited budget, the simplicity of construction and operation was an important concern. As a result, a filament driven ion source was selected. While filament-driven ion sources are inexpensive and simple to operate, they suffer from a few drawbacks.

The main drawback is the inherent dirtiness caused by evaporated filament material that condenses on the inner surface of the source chamber. This deposited material can trap sample gases that could later be released and interfere with the measurement of a subsequent sample.

The second concern with a filament is the large heat load generated. Typical filament driven ion sources use tungsten filaments on the order of 1 mm in diameter, which require about 50 A to heat them to 2500 K (81, 89). This temperature achieves a good balance between electron emission, and filament lifetime. For a nominal length of 10 cm, the voltage drop across this filament would be about 5 V, corresponding to a power draw of about 250 W. These ion sources are bigger than the compact NRL source, and as a result have better cooling from radiation and conduction. Sources with even higher power demands are often constructed using copper, and have specially designed cooling channels. Due to the compactness of the NRL ion source, a smaller filament (0.508 mm) was selected. For the same length, this filament requires roughly one third the heat load to attain 2500 K, so cooling of the source chamber was provided by forced convection. In future revisions of this prototype, the sacrifice in electron emission and filament lifetime by using the smaller filament could be regained by implementation of more sophisticated cooling designs.

Electrical connection to the filament of the NRL ion source was made by inserting the ends of the filament into small holes drilled into the ends of both vacuum-side conductors of a medium current (150 A) power feedthrough bonded to a 2.75” Del-Seal flange. Set screws used to crimp the filament into place. While the current rating of these feedthroughs was significantly more than was required for the selected filament,

they will allow for an easy switch to bigger filaments if the cooling of the ion source is upgraded. The filament was made by bending a 7.5-cm long piece of the tungsten wire mentioned above into a loop, as shown in Figure III-2.

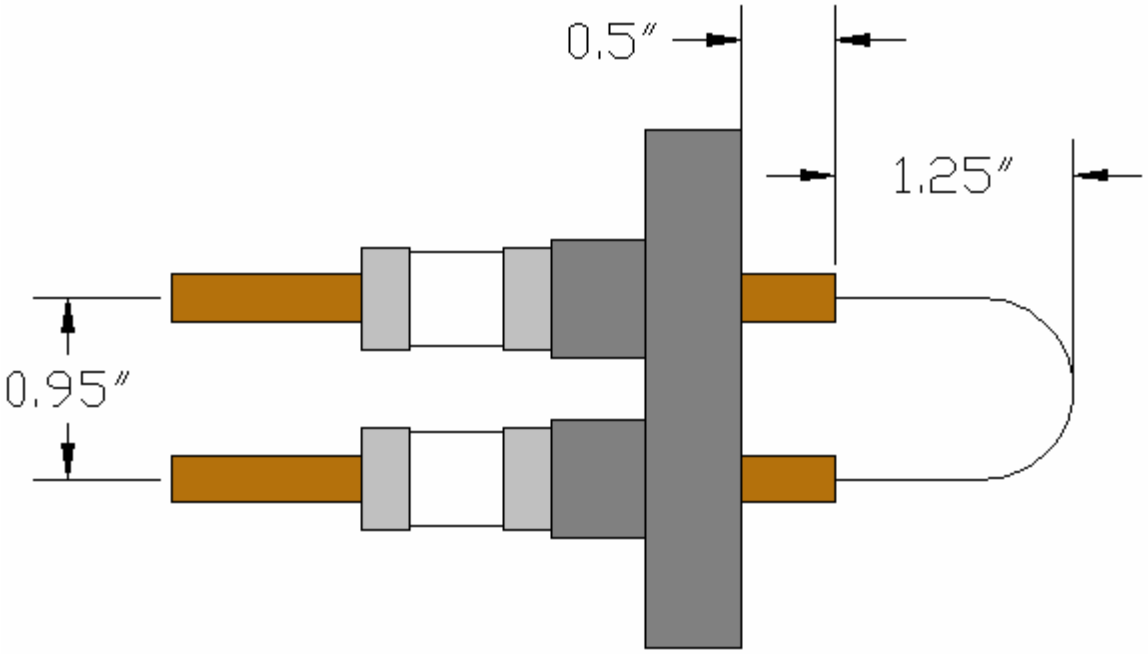

Figure III-2. A side view of the filament and flange assembly.

III.1.C Plasma Electrode

The design of the plasma electrode was important because its shape and position affect the behavior of both the plasma as well as the ion beam that is extracted from the source. Since the size of the aperture on the plasma electrode of a plasma ion source directly influences the size of the extracted ion beam and the extraction efficiency, large aperture is desirable. However, there are two factors that limit the maximum size of the aperture. First, as the diameter grows, the electric field across the aperture becomes less uniform resulting in optical aberrations in the extracted ion beam. Second, the conductance of an aperture increases linearly with the diameter. So for a fixed pressure

in the source chamber, the mass flow rate, and thus the pressure through the entire beamline increases with aperture diameter. Given the chamber of the NRL ion source, a nominal pressure of 50 mTorr of air at 20ºC would result in viscous flow through an aperture (90). In this flow regime, the conductance of the plasma electrode aperture would be roughly 20 times the cross sectional area. For an aperture of 2 mm in diameter, this would yield a conductance of 0.628 L/s and therefore a mass flow rate of 0.0314 Torr·L/s. As a general rule, the pressure in a beamline should be less than about 5×10^{-5} Torr to prevent molecular collisions from perturbing a transported ion beam. To attain this pressure, the pumping speed in the beamline following the ion source would have to be roughly 630 L/s, which represents an upper limit to the pumping capacity in most ion beam systems.

Another important factor concerning the shape of the plasma electrode in a plasma ion source is the geometry with respect to the extraction electrode which follows (81, 89). Most electrodes used in beam extraction systems are not flat, but either conical or spherical in nature, since electrodes with these shapes provide field lines that do not cross the beam axis. An example of this is the Pierce-shape extraction system. The extraction system to be used with the NRL ion source was obtained from a decommissioned source of a different design. Therefore, the plasma electrode had to be made to match the shape of the extraction electrode. As a result, the plasma electrode was constructed from copper, with the geometry illustrated in Figure III-3. Electrical isolation of the plasma electrode was provided by an insulating shroud made from a commercially available high-temperature machineable ceramic (Macor) also shown in Figure III-3.

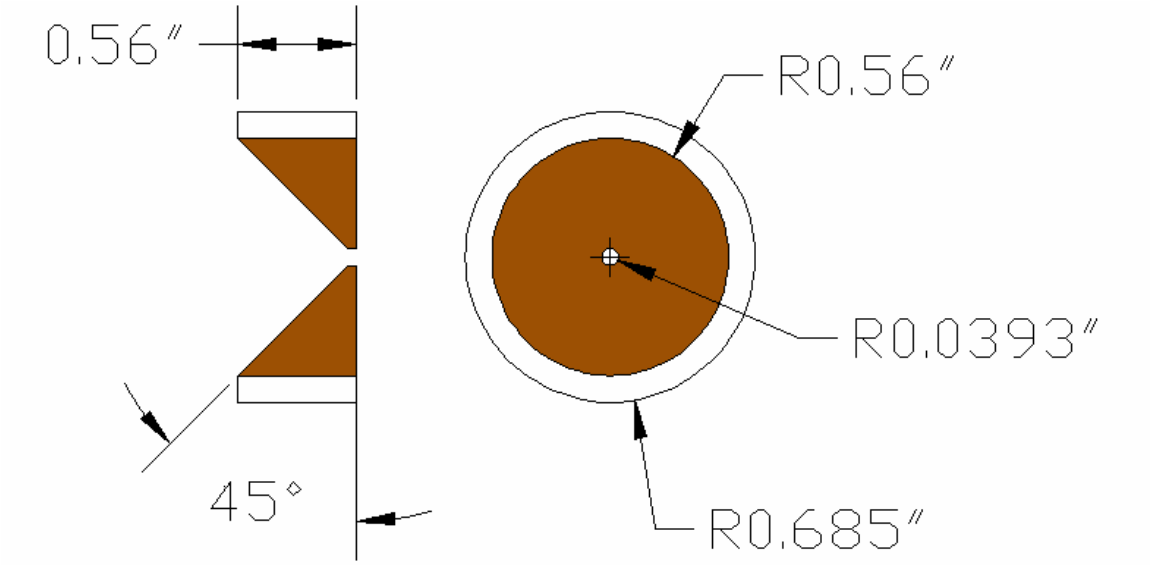

Figure III-3. A side and front view of the plasma electrode and Macor insulating shroud.

III.1.D Magnets

While it is possible to generate the multi-cusp magnetic confinement pattern using electromagnets, in practice, permanent magnets are cheaper and easier to implement. Of the two main varieties of permanent magnets, SmCo and NdFeB, NdFeB magnets can generate higher fields and are cheaper. The drawback is the lower Curie temperature which makes them more heat sensitive. However, since the heat load on the source chamber has been minimized, excessive temperatures should be avoided. As a result, the magnets selected were NdFeB measuring 1.5” in length, and 0.5” in width and thickness, and measuring about 4200 Gauss on the surface.

A yolk was constructed to support the magnets. An aluminum rod was turned down to a diameter of 2.75” and then cut to the length of the magnets. The piece was then bored out to match the outer diameter of the chamber, and eight grooves, 0.5” wide and 0.5” deep, were cut at equidistant positions around the perimeter. The piece was then cut in half so that it could be clamped around the chamber body. The final

piece is shown in Figure III-4. By making the design this way, it was easy to install and remove the magnets for investigation of source performance with and without magnetic confinement. An additional benefit of this design was the increased cooling since the aluminum piece will conduct heat away from the surface of the source body and radiate the heat more efficiently.

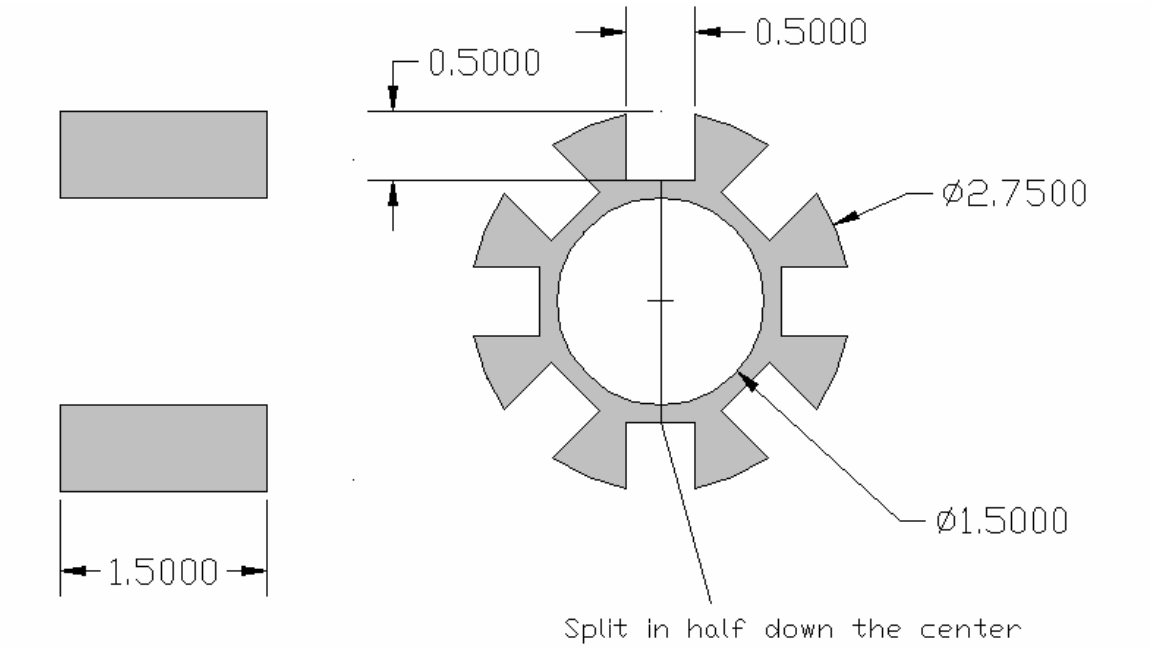

Figure III-4. A side and front view of the magnet support yolk.

III.1.E Feedthroughs

There are a number of feedthroughs that were required for the NRL ion source, as shown in Figure III-5. In order to ensure vacuum tightness of the source chamber, these feedthroughs were welded to the body. The first feedthrough is a 1/4" Swagelok fitting which was designated for a support gas inlet. A tee was connected to this feedthrough with one port attached to a Teledyne-Hastings model DV-6 thermocouple tube which allowed measurement of the pressure in the source chamber. The other port of the tee was connected to plastic tubing which lead to a metering valve

(Swagelok model SS-4-BMG) attached to a gas cylinder. Adjustment of the metering valve allowed the source chamber to be loaded with a specific pressure of a support gas for the plasma. Additionally, by closing the needle valve, the gas cylinder could be changed to a different gas without having to vent the entire source.

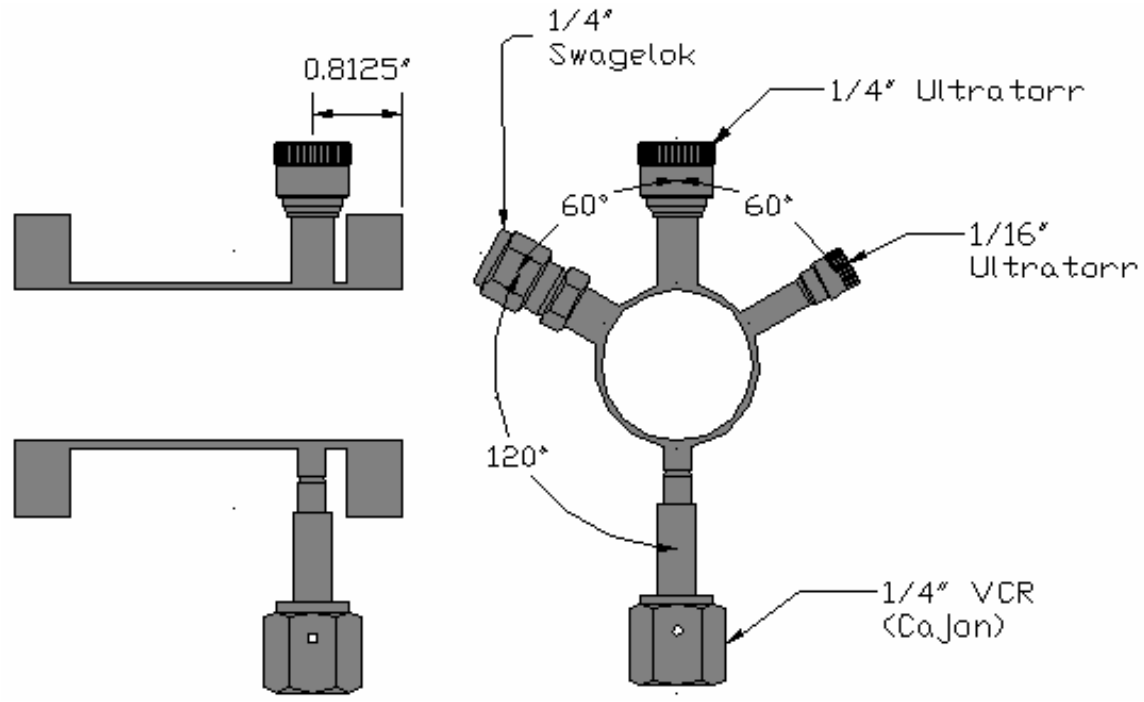

Figure III-5. A side and front view of the feedthroughs that were welded onto the body of the source chamber.

During initial troubleshooting and characterization of the NRL ion source, pure support gases were used. However, the source also needed the capability to accept injected aliquots of sample gas. Since the ion source was intended to be coupled with a GC the second feedthrough was a 1/16" Ultra-Torr fitting that allowed the attachment of capillary tubing. Implementation of this injection system is described in Section VII.2.A.

The third feedthrough was a 1/4" Ultra-Torr feedthrough which was designated for insertion of a Langmuir probe. A Langmuir probe is a device for

measurement of certain plasma parameters such as electron density and temperature, ion density and temperature, as well as the plasma potential. The specific operation of the Langmuir probe is described in Section VI.1.A. The measurement of these parameters was important in understanding the behavior of the plasma and correlating it to the extracted ion beam. The construction and use of the Langmuir probe in Section VI.1.

The final feedthrough was a 1/4" Cajon VCR fitting and was intended for the cesium inlet. A reservoir loaded with cesium could be attached and when sufficiently heated would allow cesium vapor to flow through this inlet. Since cesium condenses at room temperature, the inlet line must also be heated. A valve between the reservoir and the line would allow isolation during source maintenance preventing poisoning of the cesium. It is important that the entire assembly be heat resistant since it will be heated to around 200ºC to vaporize the cesium. Unfortunately, due to time and logistical constraints, the cesium reservoir was not fully implemented, but this assembly provides for future experimentation.

III.1.F Adapter Flanges

In order to couple the NRL ion source chamber to the rest of the ion beamline, two adapter flanges were constructed. The first adapter flange, shown in Figure III-6, was a 2.75" OD to 6" OD Del-Seal zero-length reducer which has been modified by adding a BNC feedthrough. A 14-gauge braided copper wire was attached to the vacuum side connector pin of this feedthrough and fed to the plasma electrode. The end of the wire was silver soldered onto the face of the plasma electrode to provide a solid electrical connection, as well as good thermal contact. The inner diameter of the

flange has also been counter-bored to allow adequate clearance for the extraction electrode that followed, as well as to increase vacuum pumping.

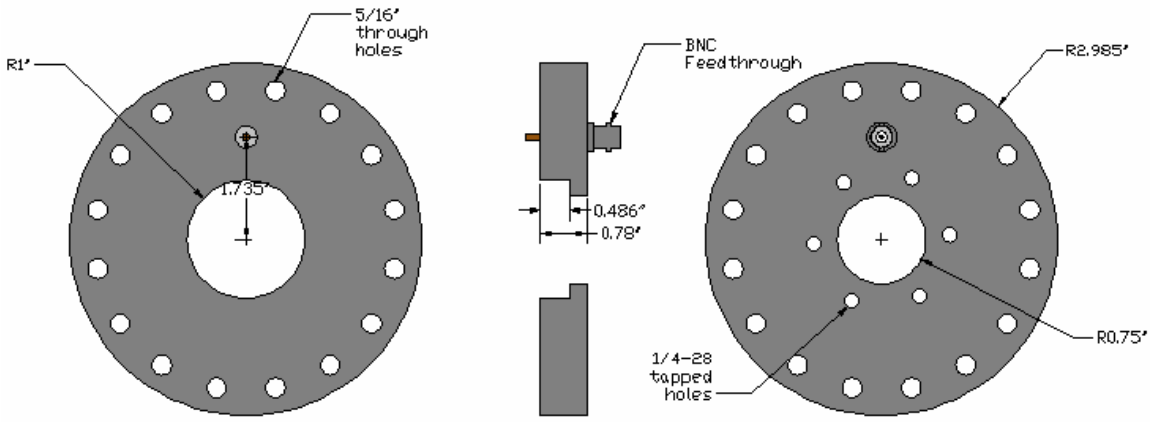

Figure III-6. A side, front, and rear view of the first adapter flange.

The second adapter, shown in Figure III-7, was a custom-built flange which joins the 6" Del-Seal side of the first adapter to the 8" OD NEC style flange that was on the extractor assembly that followed. The NEC style flange uses an aluminum gasket to provide the vacuum seal. It is important to note that the wider inner bore of this flange provided the necessary clearance for the first element of the extractor assembly. The assembled source and adapter flanges are shown in Figure III-8.

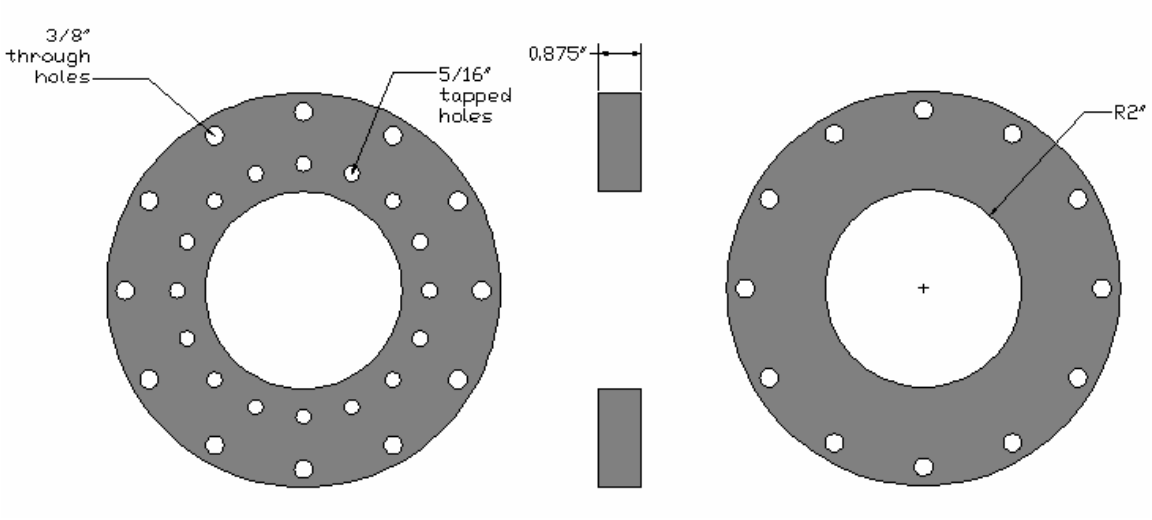

Figure III-7. A side and front view of the second adapter flange.

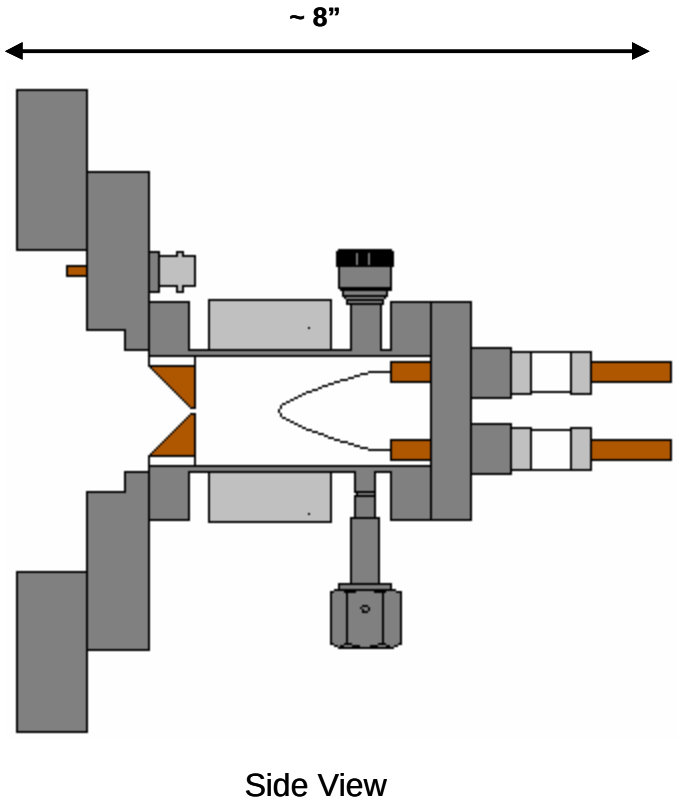

Figure III-8. A side view of the entire assembled source.

III.2 Ion Beam Extraction

III.2.A Extractor/Einzel Lens

An extraction system is necessary in order to form an ion beam from ions in the plasma sheath. The simplest extraction configuration is a two-electrode system (81, 89). The first electrode is the plasma electrode which serves to define the size and shape of the emissive surface of the ion source. The source chamber is typically biased to a negative potential with respect to ground, and the plasma electrode is biased slightly positive with respect to the source chamber. The second electrode is the extraction electrode and is grounded so that negative ions are accelerated to it. This extraction strategy has a limited beam energy maximum (<1 keV). For injection into a tandem accelerator, a beam energy of around 50 keV is ideal. As a result, more advanced designs, utilizing intermediate electrodes, are employed.

The most common arrangement is a tetrode system (81, 89). As in the two-electrode system, the source chamber is biased negatively with respect to ground, and the plasma electrode is biased positively with respect to the chamber. The extraction electrode can either be grounded, or biased at a voltage intermediate to the source chamber and ground. A third electrode, referred to as the focusing electrode, is biased negatively with respect to the extraction electrode, and decelerates the beam slightly, before the final, grounded, electrode reaccelerates the beam. Due to the functionality of the electrodes, this extraction system is also referred to as a decel-accel extraction system. Not only can this strategy produce beams of higher energy, the beams are also better focused, an important parameter if transport over long distances is required.

The extraction system selected for the NRL ion source was the extractor assembly from a commercially available cesium sputter type ion source (NEC, SNICS-II Model), which is the decel-accel type. The geometry of the extractor, as well as the

placement of the electrodes with respect to the plasma electrode, is shown in Figure III-9. In this design, the extraction electrode was held at local ground, and a power supply was used to apply a negative bias to the source chamber. The focusing electrode was attached to a positive power supply which floated from the source chamber potential.

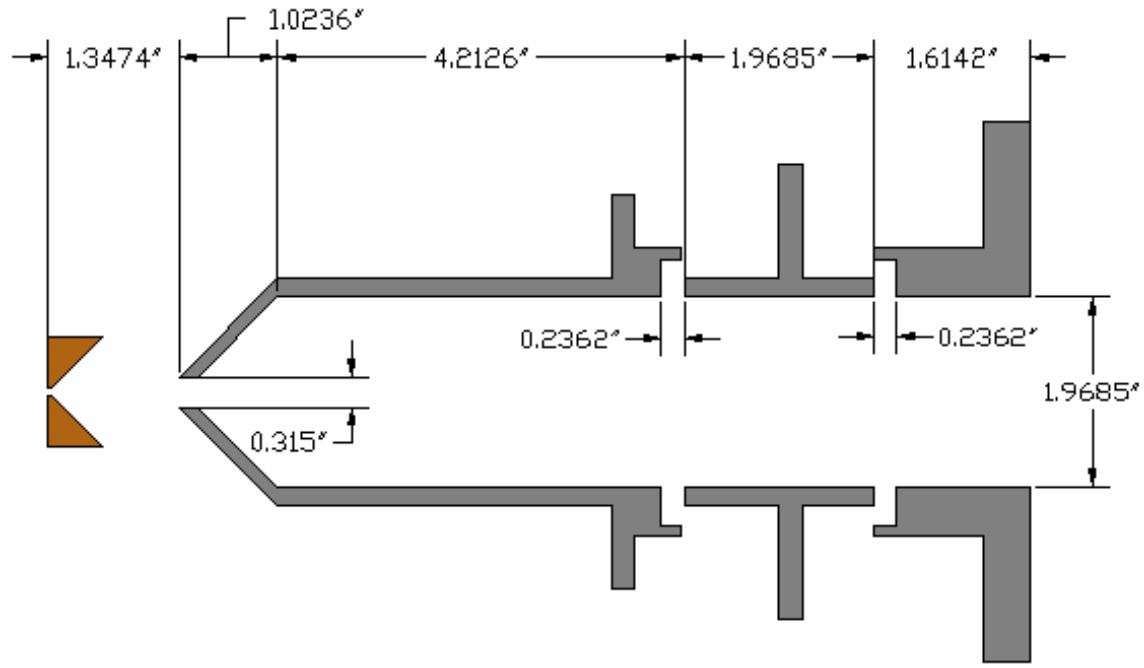

Figure III-9. A side view of the extractor assembly showing its orientation with respect to the plasma electrode.

III.2.B Acceleration Tube

Since the extraction system was limited to beam energies of tens of keV, which would still be problematic to inject into the tandem accelerator, a simple accelerator tube was employed immediately following the extractor assembly. The accelerator tube was obtained from the same ion source as the extractor, and its configuration and orientation with respect to the extractor, is shown in Figure III-10. One end of the tube attached to the extractor assembly was connected to a power supply, while the other end was grounded. The nine intermediate sections were connected by a

resistor chain (150 MΩ each), which assured a uniform voltage gradient, and nominal current draw on the power supply.

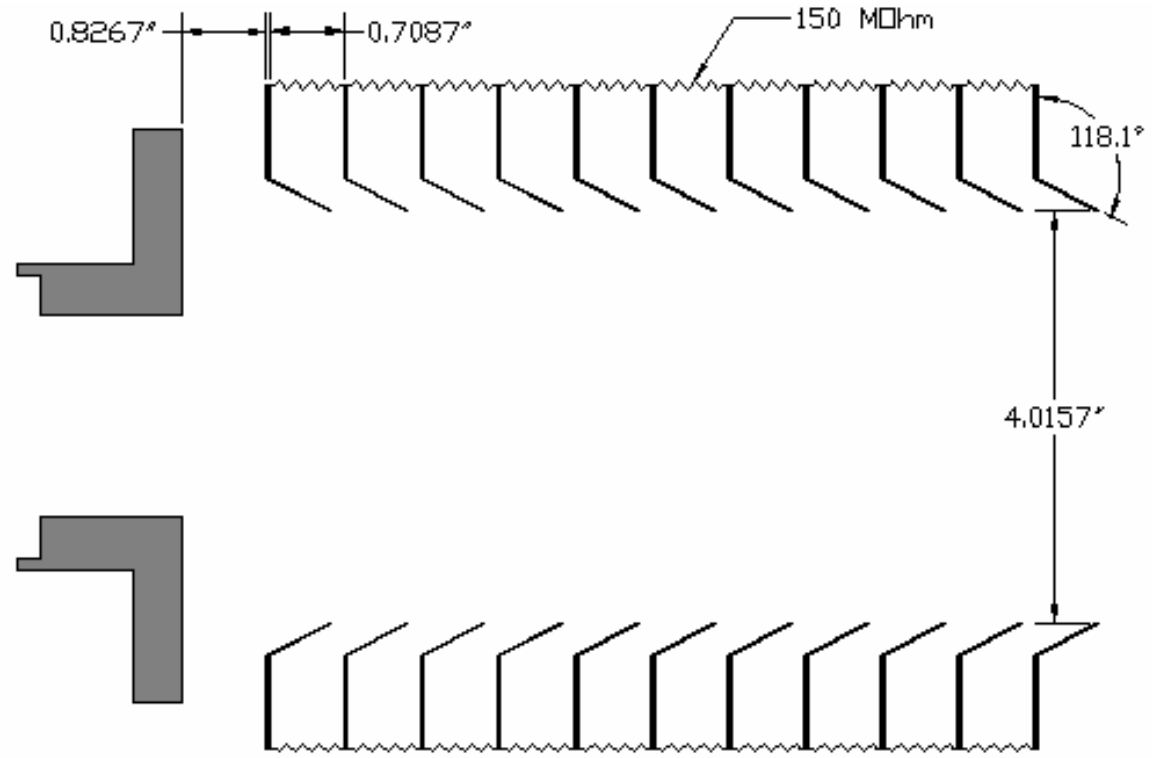

Figure III-10. A side view of the accelerator tube showing its orientation with respect to the third element of the extractor.

III.2.C Electrical Configuration

Figure III-11 shows an illustration of the entire source chamber/extractor/accelerator tube assembly with the relevant electrical connections. Table III-1 lists the specifications for all of the power supplies used. All of the power supplies, with the exception of the accelerator tube power supply, were mounted in a standard 19" electronics rack that was approximately five feet tall. The accelerator tube supply was mounted elsewhere and had a good connection to earth ground. The output of the accelerator tube supply was connected to a terminal on the extractor end of the accelerator tube using a high voltage cable. This terminal was also in electrical contact with the first and third elements of the extractor assembly. The ground of the electronics

rack was connected to a terminal on the source end of the extractor, creating a local ground, also referred to as the source deck potential. Power (110 VAC) to the electronics rack was transmitted through an isolation transformer (Universal Voltronics, model ITO-2-2-5-50), which allowed the entire rack to electrically float. The extractor power supply was connected to the same terminal as the accelerator tube supply, however, since this point is electronically fixed and the source deck is floating, this effectively lowered the deck potential up to 15 kV below the accelerator tube bias. This yielded a maximum deck potential of 75 kV below earth ground. A 10 MΩ resistor was attached between the accelerator tube/extractor terminal and the source deck ground in order to prevent a dead short between the two.

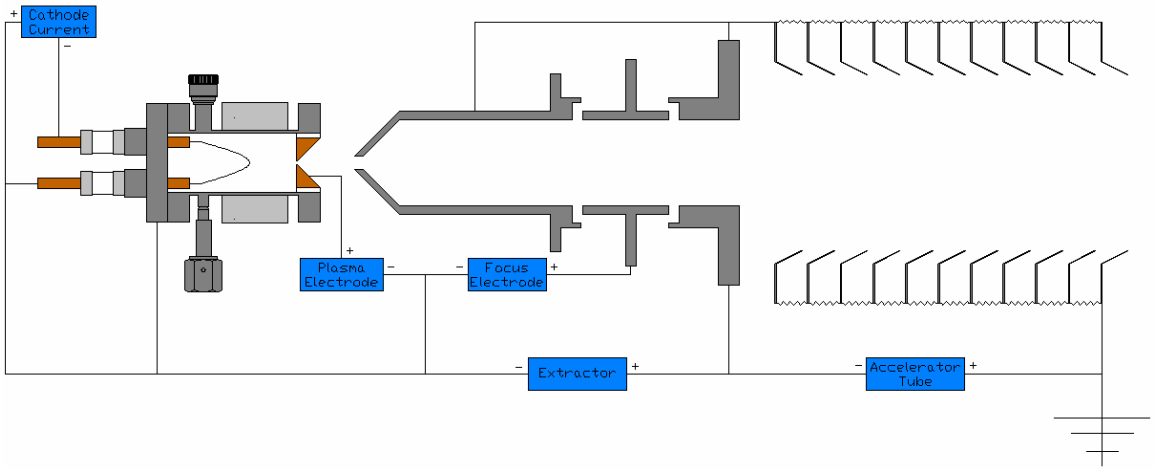

Figure III-11. A schematic drawing showing the electrical connections to the ion source, extractor, and accelerator tube.

Table III-1. A List of the Power Supplies Used with the NRL Ion Source Assembly.

Description	Manufacturer	Model #	Voltage Rating (V)	Current Rating (A)
Filament Current	Sorensen	SRL 10-50	10	50
Plasma Electrode	Sorensen	DCR 300-5A	300	5
Extractor	Glassman	PS/LG-15P-8-NEC	15k	5m
Focus	Glassman	PS/LG-15P-8-NEC	15k	5m
Accelerator Tube	Spellman	RHR60ON60	60k	2m

Since it was mounted in the source deck, the focus element supply allowed the middle element of the extractor to be biased above deck potential. Again, a bleeder resistor (1 MΩ) was attached between the focus element and deck to protect the power supply from a dead short. This resistor also limited the focus element bias to a maximum of 5 kV. A bleeder resistor was not necessary for the cathode (filament) or anode (plasma electrode) supplies since they operated at a low voltage. Since the needle on the front panel of the anode supply did not provide very fine resolution, a digital multimeter (Keithley Model 197) was placed in series with the supply. This allowed accurate measurements of the current draw on this supply, which was effectively the plasma discharge current. In addition to these power supplies, a Hastings Model DV-6 thermocouple reader was also installed on the source deck to allow monitoring of the pressure in the source chamber. Finally, a cooling fan was mounted on the source deck and aimed at the source chamber.

III.3 Testbench

III.3.A First Section

In order to evaluate the performance of the ion source, a testbench was required. The ideal testbench should allow measurement of the intensity and emittance of the extracted ion beam, as well as provide energy and mass analysis. Fortunately, a system with all of these capabilities was already available on the NRL AMS system. The testbench can be divided into three logical units, the first of which is shown in Figure III-12.

The first component of this section is an electrostatic steerer (NEC, model ES6) which allowed for correction of minor misalignment of the extracted ion beam. The

steerer was constructed with a tee so that a vacuum pump can be placed on the off axis port. Due to the gas load associated with this ion source, a fast turbo pump (Pfeiffer-Balzers, model TMU100C) was selected for this pumping port. There are also two smaller side ports on the steerer. On one port a valve was installed and used to vent the source, or to attach a leak checker. A full-range vacuum gauge (Pfeiffer-Balzers, model PKR 251) was installed on the second side port to measure the pressure in the beamline. The next component is a slit assembly (homemade). Since these slits are moveable and electrically isolated from the chamber, they allowed for assessment of beam position as well as size. Following the slits is a Faraday cup (homemade) which was used to measure the total beam intensity from the source. Due to space limitations, it was not possible to construct the cup with sufficient aspect ratio to provide geometric suppression of secondary electron emission. Therefore, the cup was mounted between two permanent magnets to provide magnetic suppression. Alignment of this section with the rest of the testbench was possible because of the bellows which follow the Faraday cup. This section can also be isolated from the rest of the testbench by actuating the gate valve after the bellows. This feature was useful since it allowed the source to be serviced without venting the entire testbench. Following the gate valve is the switching ESA, which is the first component of the second section of the testbench. It is important to note that the components between the steerer and the ESA were selected with comparatively narrow tube diameters. This was done to create a diaphragm effect in order to limit the gas load on the rest of the system.

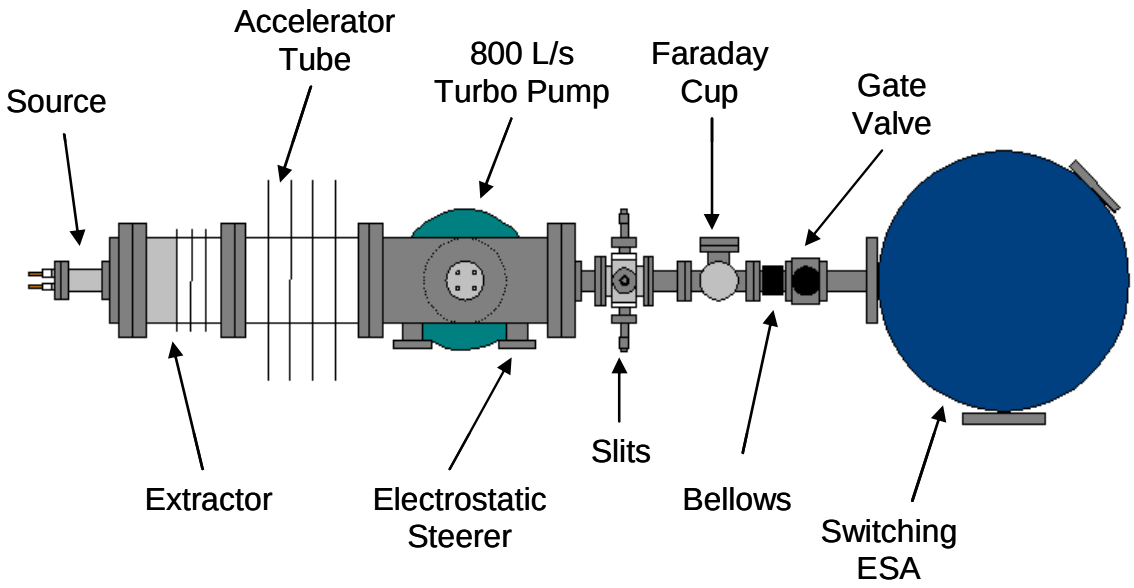

Figure III-12. The first section of the testbench that was used to evaluate the performance of the ion source.

III.3.B Second Section

The second section of the testbench, shown in Figure III-13, begins with the NEC switching ESA. The ESA has a pneumatically actuated rotating table so it can be quickly switched between input ports. The ion source was installed on the 135º (with respect to the output port) input port. The ESA disperses ions based on their energy to charge quotient. Since nearly all of the ions were in the -1 charge state, the ESA provided energy analysis to assess the energy spread of the ion beam. Following the ESA is another electrostatic steerer (NEC model ES5L), which serves the same purpose as the steerer described in Section III.3.A. This particular steerer differs from the previously described model in that it does not have the extra ports for the vacuum pump, rough out valve, and vacuum gauge. However, this steerer is coupled with a beam profile monitor (BPM). The BPM is a helical wire that rotates at a 45º angle within the beam. Due to this geometry, the BPM can measure the size and position of the x and y components of

the beam. Not only does this serve as a useful diagnostic tool, but it also allows for a basic determination of emittance by measurement of the size of a beam that has been limited to a known size by the slits in the first section of the testbench. Following the steerer/BPM module is a Faraday cup/slit assembly (custom-built). These slits are not instrumented, so only serve to fix the beam size and position. The Faraday cup is electrically suppressed. The next component is an Einzel lens (NEC, Model EL44-50 which focuses the beam into the pretzel magnet which is the first component of the third section of this testbench. As in the first section, a bellows and a gate valve allow for alignment and isolation, respectively, of this section of the beamline.

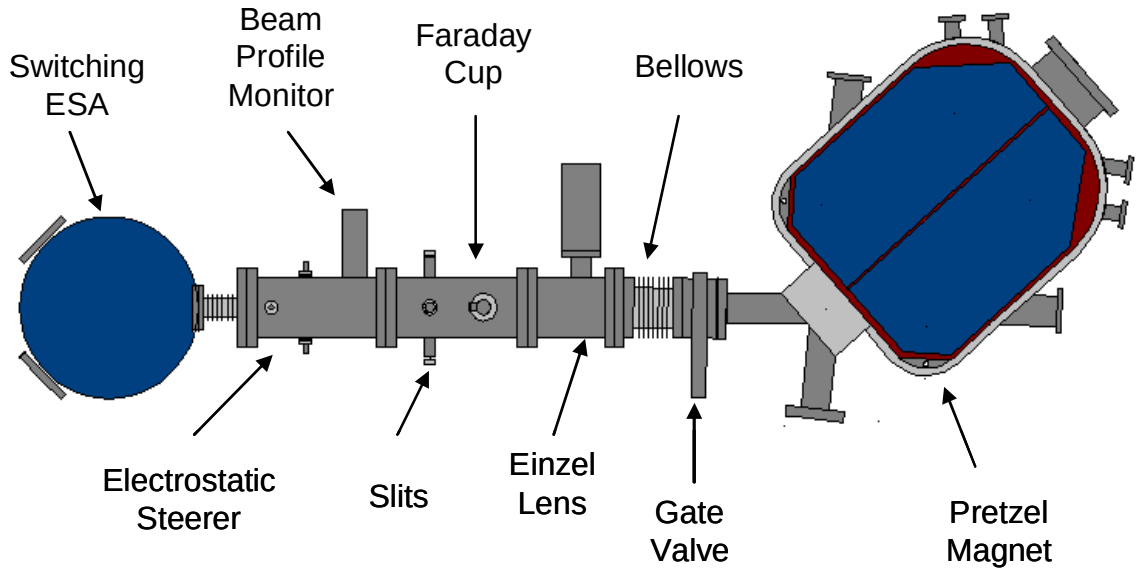

Figure III-13. The second section of the testbench that was used to evaluate the performance of the ion source.

III.3.C Third Section

The first component final section of the testbench, shown in Figure III-14, is the pretzel magnet. Since the ions at this point have the same charge state and nearly the same energy, the pretzel magnet will disperse them according to their mass. By placing a mask with an aperture with a width corresponding to 1 amu along the plane of

symmetry of the magnet, an ion beam of a single mass can be transmitted. By measuring this ion beam on the Faraday cup (NEC, model FC-26) following the magnet, mass spectra of the injected beam can be generated. The electrostatic quadrupole triplet (NEC, model EQTA76-15) focuses the beam, and the steerer (NEC, model ES5) steers the beam onto the Faraday cup. Again, a gate valve and bellows are included in the system for vacuum isolation and alignment purposes. The layout of the entire testbench is shown in Figure III-15.

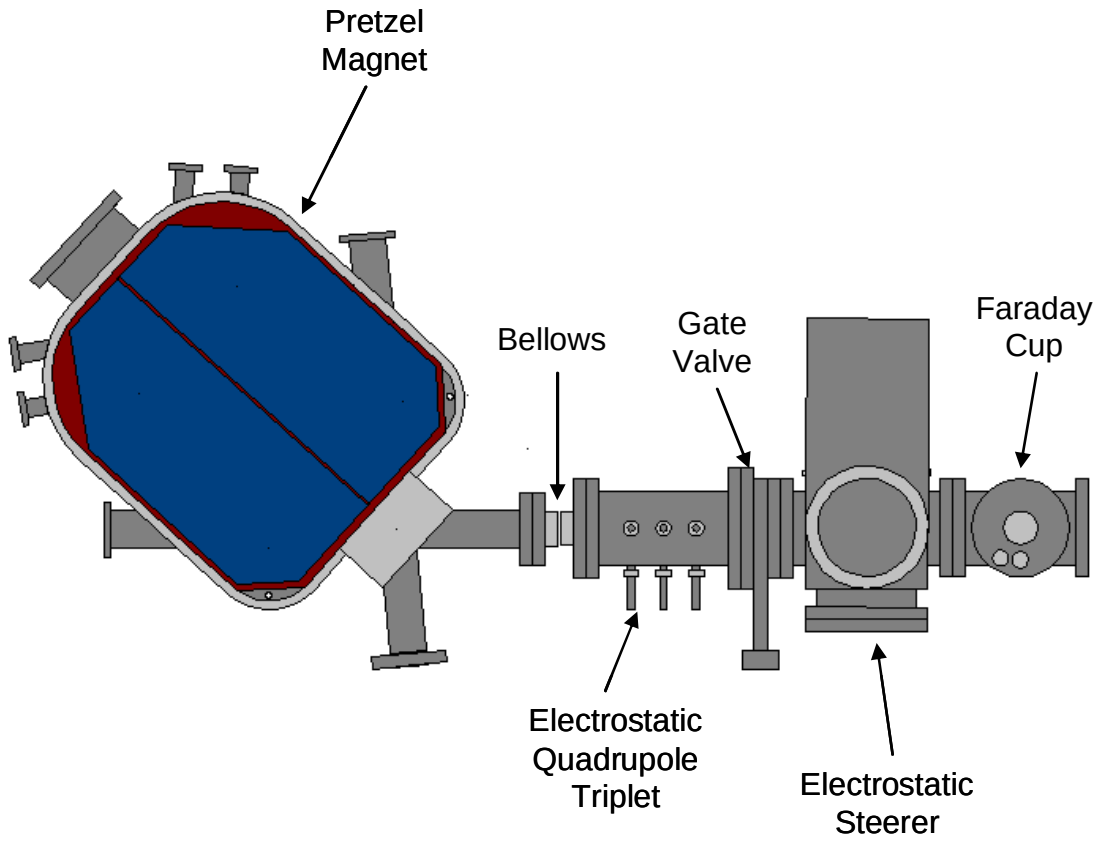

Figure III-14. The third section of the testbench that was used to evaluate the performance of the ion source.

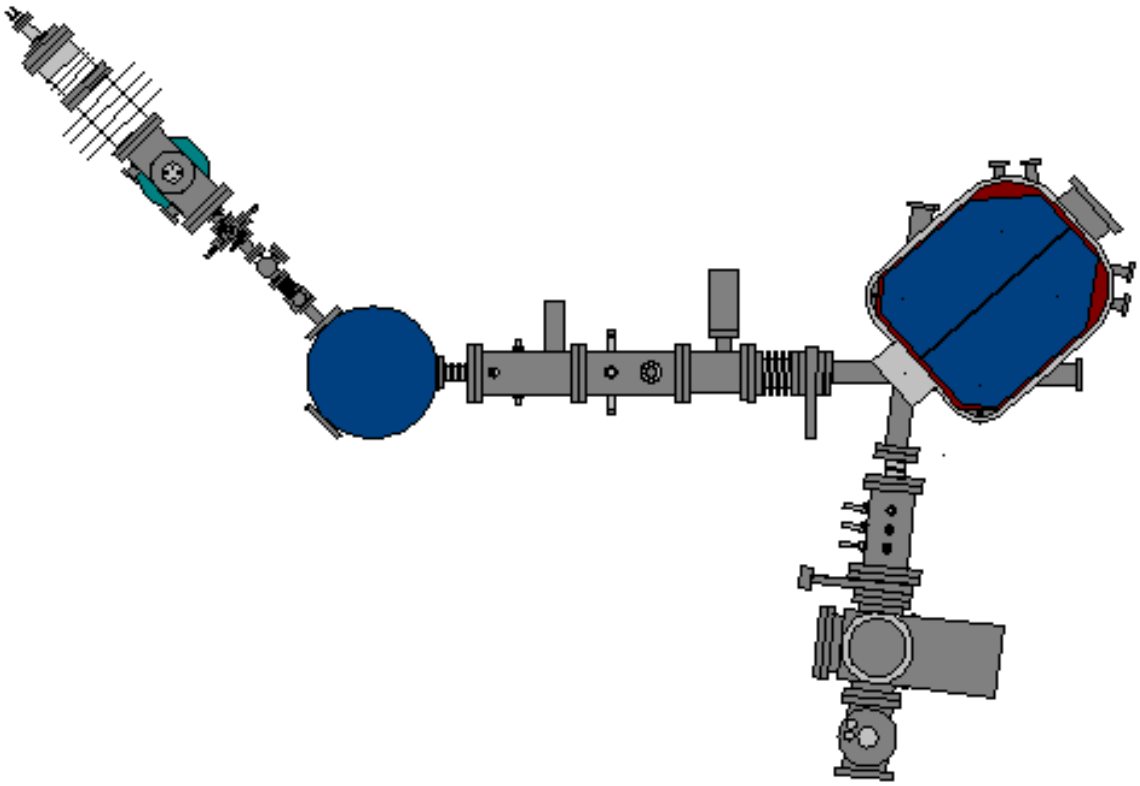

Figure III-15. The entire testbench that was used to evaluate the performance of the ion source.

IV Simulation & Preliminary Data

IV.1 Ion Source Model

IV.1.A Background

Computer models are often used to aid in design of an ion source and to predict its performance. SIMION is a widely used software package that models the trajectories of charged particles in electrostatic and magnetic fields (34). The models are constructed by creating arrays that describe the geometry of the potential surfaces in a given system. The elements of the array can be scaled to quickly adjust the potentials (i.e. change the voltage of a steering plate) without having to rebuild the entire array. An ion, which is defined by its starting position, charge, mass, and kinetic energy, can then be "flown" through a model, and its trajectory predicted by the potential arrays.

IV.1.B Method

A model was created using SIMION based on the configuration of the ion source described in Chapter III (93). By defining the potentials, equipotential contour lines were generated and are displayed in Figure IV-1. While the figure shows the entire source, extractor, accelerator tube assembly, the entire model also includes a 70-cm drift space. The drift space was included in order to assess the ability of the source to generate a beam focused at a point approximately 70 mm from the end of accelerator tube, the object position of the switching electrostatic analyzer.

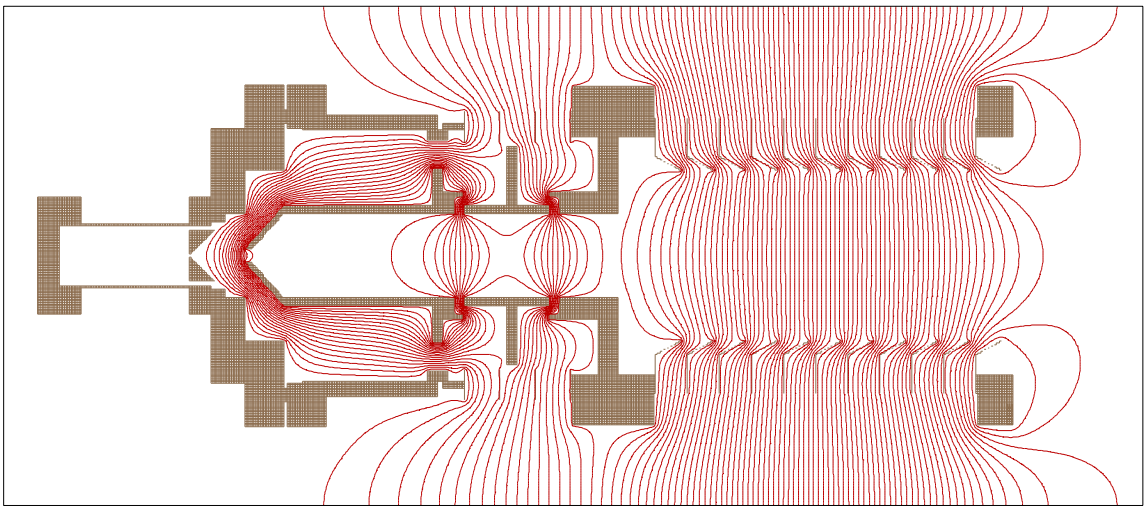

Figure IV-1. The ion source with equipotential contour lines.

Since SIMION only models the flight of ions through the source, some assumptions had to be made about the extraction of these ions from the plasma. First, since ions can only be extracted from the plasma sheath, the source can be thought of as an emissive surface within the projection of the plasma electrode aperture onto the plasma sheath facing the electrode. This surface is not necessarily flat, but rather forms a meniscus. The shape (i.e. flat, concave or convex) of this meniscus is influenced by many factors, the most important being the electron density and temperature in the plasma, the extraction voltage and geometry, and the current density of ions being extracted. Since SIMION can not predict the shape of the meniscus, all three cases were investigated. Besides the initial position, the kinetic energy of the ions had to be assumed. While the electron temperature in this type of plasma can be as high as tens of eV, the less mobile ions typically exist at thermal energies. Therefore an initial energy of 0.3 eV was assumed. However, since the voltage gradient in this region of the ion source is so high, the behavior of a 3-eV ion and a 0.3-eV ion are nearly the same. So this assumption was not critical to the effectiveness of the model. Finally, ions were assumed to have a mass of 12 and a charge of -1. Since there are no magnetic components in the

model, the mass of the ions is not important. Also, since multiply charged negative ions are so rare, they can be neglected from the model.

IV.1.C Results

Figure IV-2, Figure IV-3, and Figure IV-4 show the extraction of an ion beam from a flat, concave, and convex meniscus respectively. While the flat meniscus was the ideal beam formation situation, the size of the extracted beam from these three cases did not vary significantly. However, it is important to recognize that the SIMION code calculates the trajectory of each ion individually. As a result, the effect of charge repulsion from other ions in the beam was not accounted for in the model. This space charge effect would be most pronounced wherever there is sharp focusing of the ion beam. Consequently, the convex meniscus case would be expected to suffer from more optical aberrations and produce a poorer quality beam.

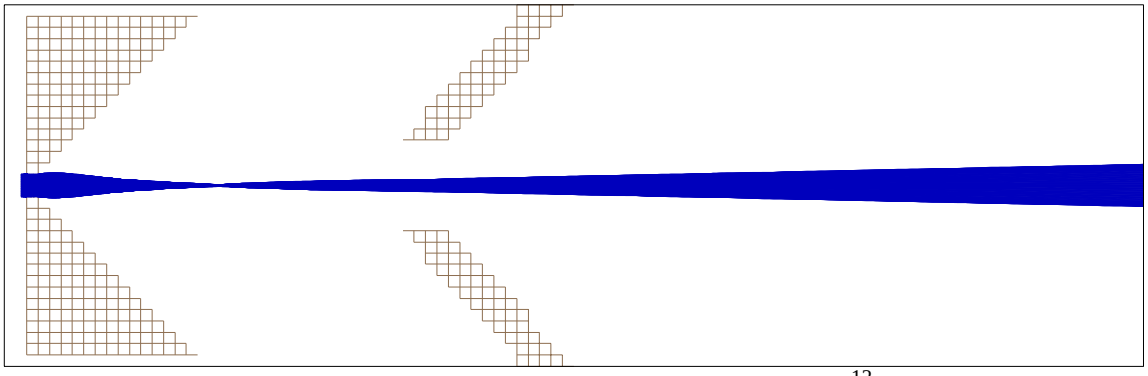

Figure IV-2. The transport of a beam initially formed from 0.3-eV $^{12}C^-$ ions from a flat meniscus located 0.5 mm behind the plasma electrode aperture.

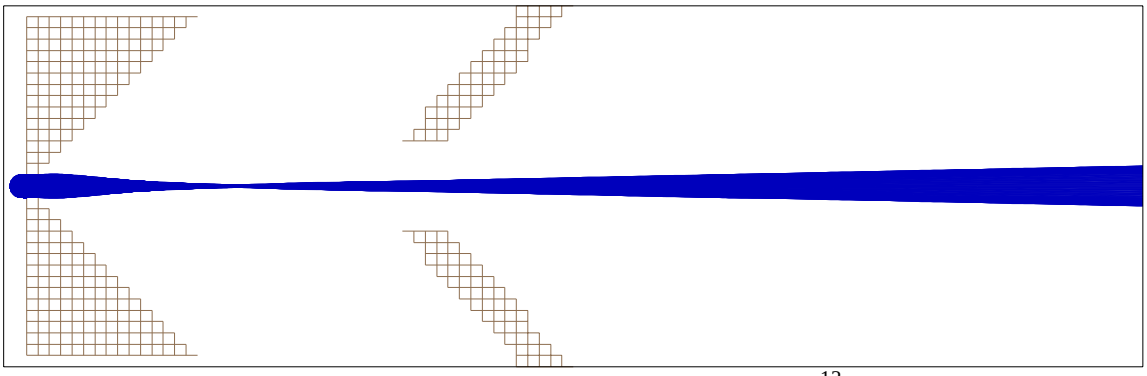

Figure IV-3. The transport of a beam initially formed from 0.3-eV $^{12}C^-$ ions from a concave meniscus whose radial diameter was located 0.5 mm behind the plasma electrode aperture and extended axially 1 mm away from the plasma electrode.

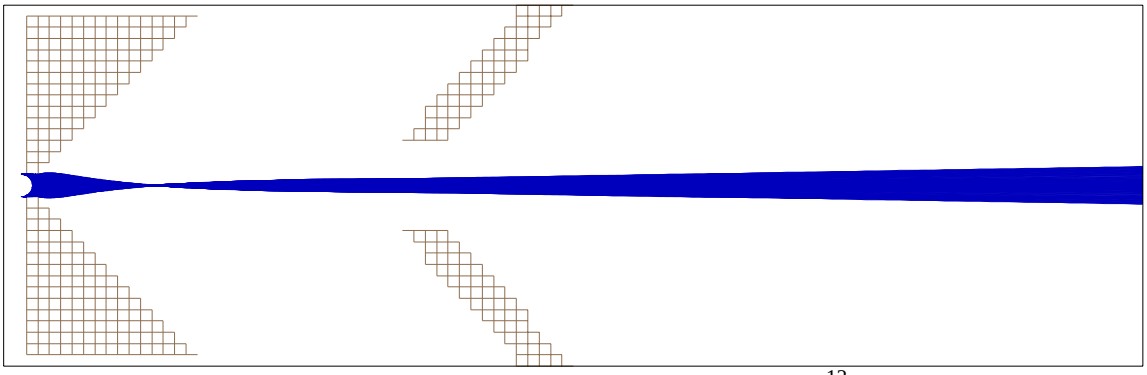

Figure IV-4. The transport of a beam initially formed from 0.3-eV $^{12}C^-$ ions from a convex meniscus whose radial diameter was located 0.5 mm behind the plasma electrode aperture and extended axially 1 mm towards the plasma electrode.

Another important parameter that was investigated with the model was the position of the plasma electrode with respect to the extractor cone. When the electrode was close to the extractor cone (Figure IV-5), the voltage gradient was higher so the beam was focused very sharply in front of the extraction electrode, which resulted in a very divergent beam entering the extractor. This beam was so divergent that even when the focus element was fully biased, a focused image could not be formed at the object position of the ESA. In the case where the plasma electrode was far away from the extractor (Figure IV-6), the beam was focused to the object position of the ESA, however, the beam was divergent as it passed through the plasma electrode aperture. As

a result, a portion of the ions were lost as they struck the electrode. In order to balance these two effects, an intermediate position was selected, as shown in Figure IV-7.

Figure IV-5. The extraction of 0.3-eV $^{12}C^-$ ions from the ion source with the plasma electrode positioned 18 mm from the front tip of the extraction electrode cone.

Figure IV-6. The extraction of 0.3-eV $^{12}C^-$ ions from the ion source with the plasma electrode positioned 48 mm from the front tip of the extraction electrode cone.

Figure IV-7. The extraction of 0.3-eV $^{12}C^-$ ions from the ion source with the plasma electrode positioned 33 mm from the front tip of the extraction electrode cone.

The final parameter that was investigated with the model was the size of the plasma electrode aperture since the efficiency of the ion source is strongly influenced by the size of the aperture. While an aperture size of 2 mm represents an upper limit with respect to the gas load on the beamline, it was instructive to determine what the upper limit would be from a beam transport standpoint. As shown by Figure IV-8, an 8-mm aperture produced a beam that almost completely filled the extractor. This beam could still be focused onto the object position of the ESA; however, the beam nearly filled the acceptance aperture of the ESA. Consequently, while the first generation of the ion source used a 2-mm aperture, if the vacuum pumping capacity is increased to allow larger apertures in future generations, the aperture size should be kept below 8 mm.

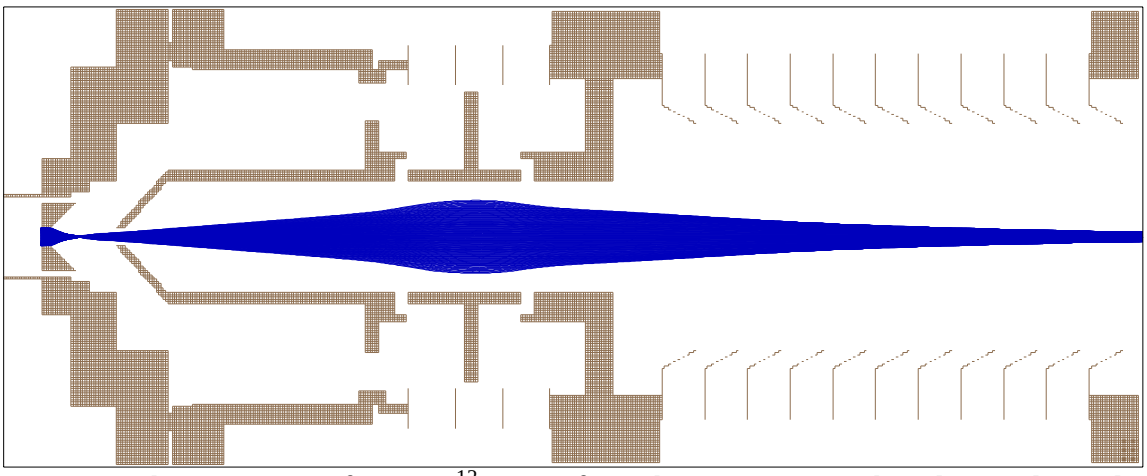

Figure IV-8. The extraction of 0.3-eV $^{12}C^-$ ions from the ion source with a plasma electrode aperture size of 8 mm.

IV.2 Preliminary Results

IV.2.A Effect of Pressure

Before attempting to extract an ion beam from the source, some basic characterization of the plasma behavior was performed (93). Not only did this provide experience with the generation of a plasma, but also allowed for troubleshooting of the experimental setup. Since the Langmuir probe had yet to be implemented and no visual line of sight to the plasma volume was possible, the only diagnostic tool available was the measurement of current on the anode, also referred to as the plasma discharge current. The three main parameters of interest are the gas pressure in the source, the composition of the gas, and the presence of magnetic confinement. Being a noble gas, with a mass close to that of carbon dioxide, argon was selected as the test case with which to compare future source performance. To evaluate the influence of gas pressure, the source was loaded with various pressures of argon by adjusting the metering valve between the chamber and the gas cylinder. A plasma was then struck by running approximately 100 W (10 V/10 A) through the filament and then increasing the anode voltage until a measurable current was noticed. The anode voltage was then adjusted to various points

and the discharge current at each point was recorded to generate the plot shown in Figure IV-9.

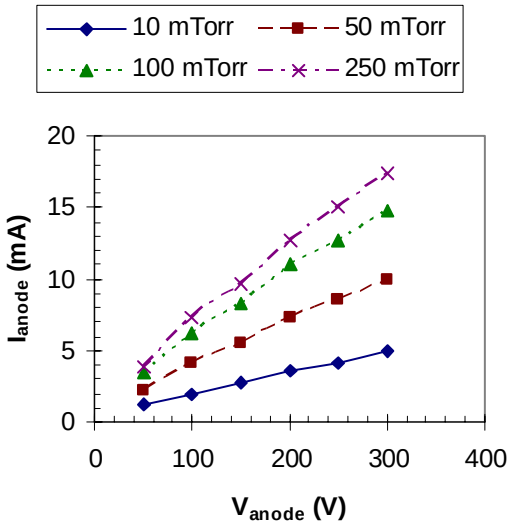

Figure IV-9. The measured plasma discharge current versus applied voltage on the anode for argon at various pressures.

As expected, the discharge current increased as the anode voltage increased since more electrons can be extracted from the plasma. The increase was not linear, but rather logarithmic and started to flatten out at higher values of anode voltage. The discharge current increased as the pressure in the source was increased since there were more argon atoms to fuel the plasma. Another way to express these data is by plotting the discharge current versus the source pressure for various voltage settings, as shown in Figure IV-10. The discharge current flattened out with increasing pressure, presumably because the argon atoms began to quench the plasma by interfering with secondary ionization.

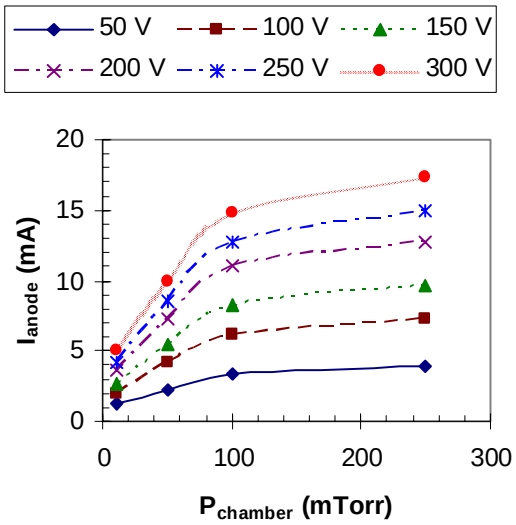

Figure IV-10. The measured plasma discharge current versus source pressure of argon at various applied anode voltages.

IV.2.B Effect of Magnetic Confinement

The second parameter that was investigated was the addition of magnetic confinement. Negative ion yield from a plasma ion source of this type is enhanced by approximately an order of magnitude with the addition of a multi-cusp magnetic field. Figure IV-11 shows the plasma discharge current for argon (50 mTorr, 100 W filament power) for various settings of anode voltage with no magnets and with magnets in the multi-cusp arrangement. While both cases had the same general trend, the multi-cusp arrangement yielded a hundred times higher discharge current. This increase corresponds to the increase in electron density within the plasma due to the magnetic confinement.

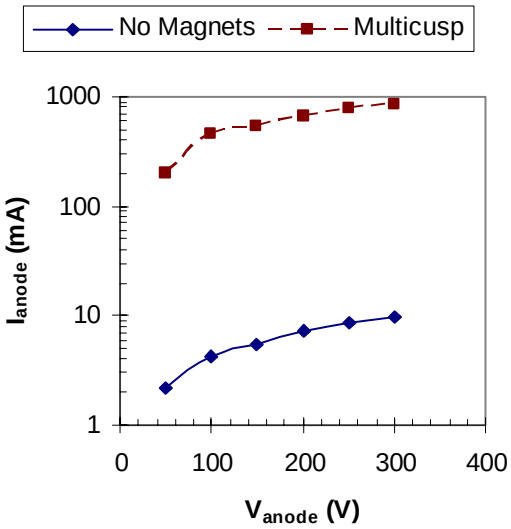

Figure IV-11. The measured plasma discharge current versus applied anode voltage for argon at 50 mTorr with no magnets and magnets in a multi-cusp arrangement.

IV.2.C Effect of Gas Composition

The third parameter that was investigated was the behavior of different gases. Since ultimately carbon dioxide will be used with the ion source to produce a carbon beam for AMS, it is important to understand its behavior compared to argon. Again, the source was loaded with a fixed pressure of gas, in this case 50 mTorr, by adjusting the metering valve. Magnets were installed in a multi-cusp arrangement. The filament power was again 100 W, and the plasma was ignited by adjusting the anode voltage. Figure IV-12 shows the measured discharge current for both argon and carbon dioxide at various values of anode voltage. While both species exhibit the same general shape in the plot, carbon dioxide yielded approximately an order of magnitude less discharge current than argon. This feature can be explained by noting that carbon dioxide has more degrees of freedom than argon, and therefore has more modes of interaction with the plasma electrons. While this feature is not surprising, it is important since it implies that the plasma will be greatly influenced by the composition of the gas.

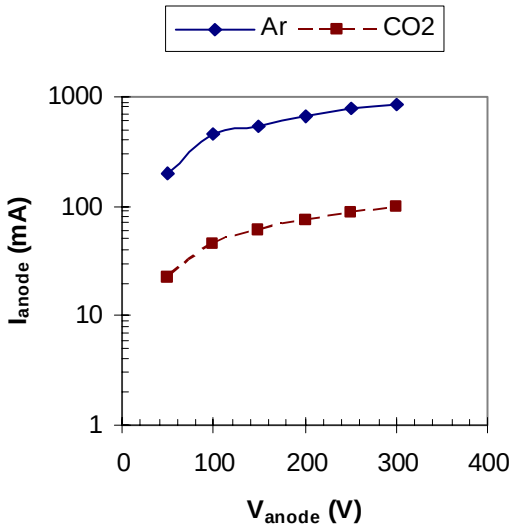

Figure IV-12. The measured plasma discharge current versus applied anode voltage for argon and carbon dioxide at 50 mTorr

V Modifications

V.1 Plasma Electrode

V.1.A Thermal Concerns

While the preliminary results from the ion source presented in Section IV.2 were promising, there were several limitations that required modifications to the initial design. The most important modifications made were to the plasma electrode. First, it was noticed that the Macor ceramic shroud that insulated the electrode from the walls of the chamber was cracking during operation. As the electrode was heated, both by absorbed heat from the plasma and resistive heating from the current flow necessary to maintain the anode bias, a mismatch of thermal expansion created stress on the insulator. Apparently, the wire that connected the electrode to the BNC feedthrough provided insufficient thermal contact to conduct the heat away, so a better method of providing this connection was necessary.

V.1.B Optical Concerns

In addition to the thermal aspect, there was an optical reason to redesign the plasma electrode. Due to space limitations, the wire which provided electrical connection between the BNC feedthrough and the electrode had to be in close proximity to the extraction cone. Since the wire is at the anode potential, which is 15 kV below the extractor potential, its presence caused a major distortion of the electric field lines in the extraction region. This distortion would have pulled the ion beam away from its natural trajectory and would have made transport very difficult. For this reason, a less pervasive means of making the connection to the electrode was needed.

V.1.C New Design

To solve the two major problems described, a modification to the source chamber was made, as shown in Figure V-1. This arrangement differed from the original by the addition of another 1/4" Ultra-Torr fitting that allowed a 3/16" copper rod to be inserted into the source chamber. The tip of the rod was threaded (10-32 NF) so that it could be screwed into an appropriately drilled and tapped hole in the modified plasma electrode, shown in Figure V-2. This union provided a solid electrical and thermal connection. By using a thick copper rod rather than a wire, thermal conduction from the plasma electrode was greatly enhanced. In addition, since the wire that was interfering with the field lines between the anode and the extraction electrode was removed, the optical problem relating to beam extraction was solved. The addition of this new feedthrough created a physical obstruction to the magnets, so the length was adjusted by cutting them in a diamond saw. A new aluminum yolk was also constructed to match this new reduced length.

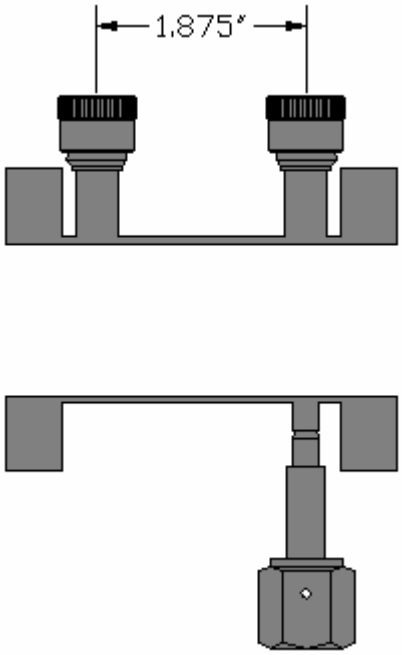

Figure V-1. A side view of the modified source chamber.

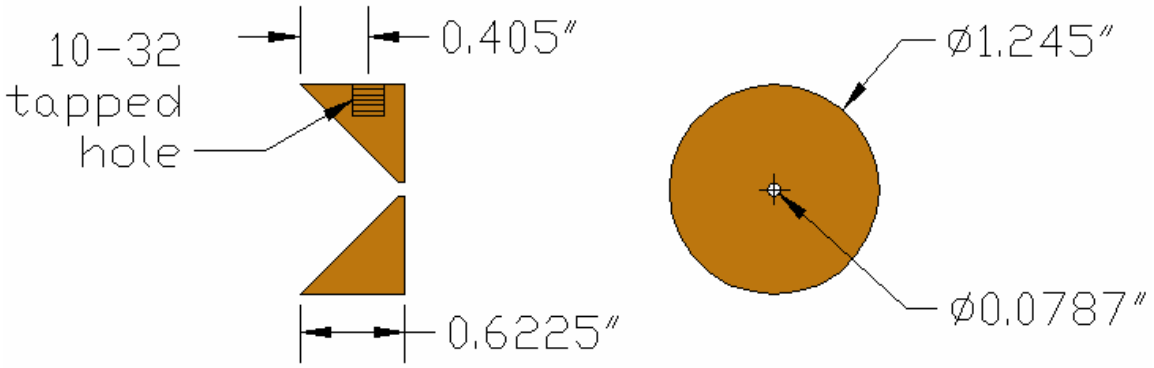

Figure V-2. A side and front view of the modified plasma electrode.

V.1.D New Insulator

In order to accommodate this new connection to the plasma electrode, a modification to the Macor insulator was necessary. While this modification could have been accomplished by merely drilling a clearance hole through the wall of the insulator, a more substantial redesign was selected to improve its performance. The original design

caused filament material to deposit on the surface of the insulator resulting in electrical shorts between the plasma electrode and the chamber wall. Initially, these shorts manifested as an increase in leakage current that made consistent measurements of the plasma discharge current problematic. Eventually, sufficient filament material would coat the insulator to create a dead short, thus requiring disassembly and cleaning of the entire source. Source cleaning was accomplished by using a Scotchbrite pad to polish the inner surface of the chamber as well as the copper anode. The insulator was soaked in aqua regia overnight to dissolve the deposited tungsten. To alleviate this problem, the insulator was redesigned, as shown in Figure V-3. By creating an inner channel with no line of sight to the filament, as well as increasing the overall surface area of the insulator, the shorting problem was practically eliminated.

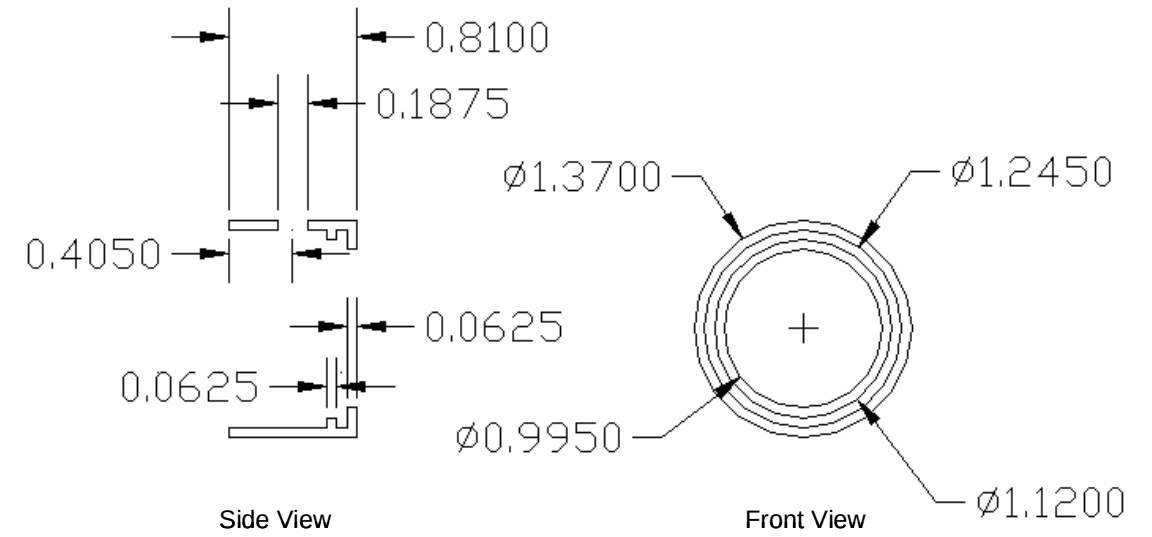

Figure V-3. A side and front view of the new insulating ring for the plasma electrode.

V.2 Filament

V.2.A Geometry

The second group of changes to the ion source involved the filament. During preliminary testing, filament life was on the order of a few hours. This presented

a problem of convenience since the entire first section of the testbench had to be vented to air in order to change the filament, and the subsequent pump-down required 8-10 hours to reach the baseline vacuum level of 2×10^{-7} Torr. However, instabilities in performance were experienced as the filament burned down. After comparing the operating parameters of the filament to those of other filament-driven ion sources, it was concluded that the filament temperature was very high, which lead to an increased evaporation rate thus shortening filament lifetime. A higher than normal filament temperature indicates that some of the primary electrons were not used by the plasma, but lost to the chamber walls. To solve this problem the filament shape was changed from the simple hair pin discussed in Section III.1.B, to the spiral geometry shown in Figure V-4. This configuration concentrated electron emission in the center of the chamber rather than at the edges, thus reducing the loss of electrons. As a result, the same yield of useable electrons was obtained at a lower temperature.

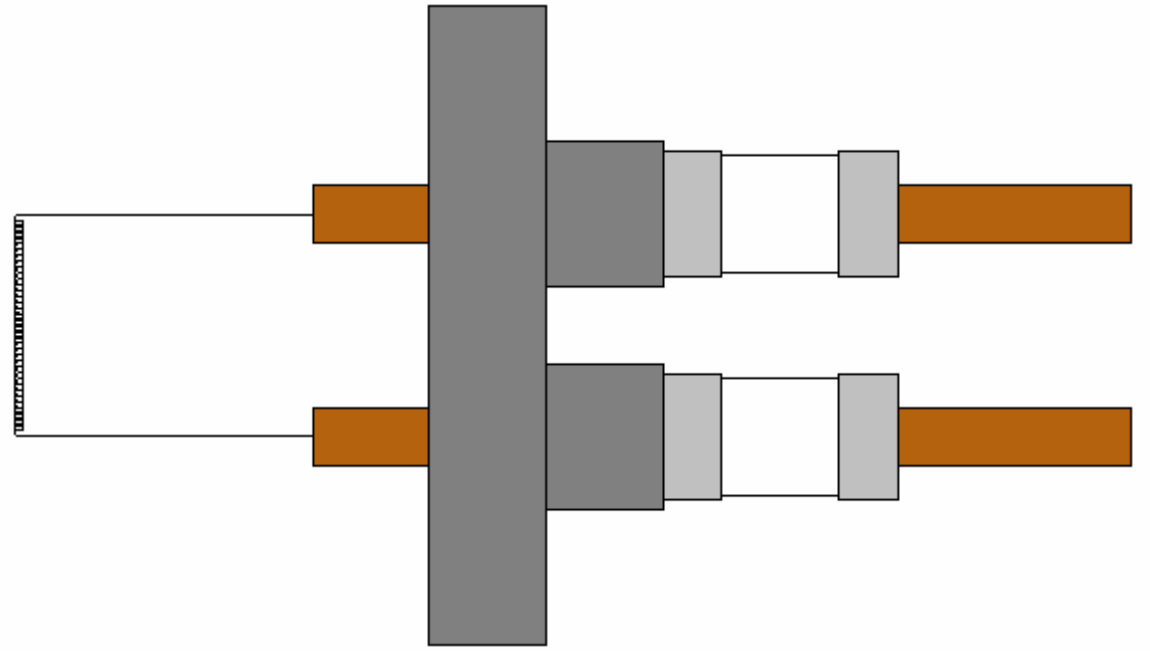

Figure V-4. A side view of the new filament geometry with the feedthrough flange.

V.2.B Material

In addition to the shape, the filament material was changed. It was noticed that the burnt out filaments suffered from significant drooping caused by gravity. In some cases, the filament drooped enough to touch the source chamber, which shorted the electrical connection. By changing the shape of the filament the drooping will be lessened since the filament temperature will be lower. However, to ensure maximum structural integrity, the filament material was changed from pure tungsten to tungsten impregnated with 2% of thorium. Since thorium has a much higher melting point, it remains in the filament as the tungsten evaporates, creating a sort of atomic frame to support the weight of the filament. Additionally, in order to lessen the heat load on the source, the filament diameter was reduced from 0.508 mm to 0.254 mm, thus reducing

the power required to attain a given filament temperature. Figure V-5 shows the entire source assembly with all of the modifications described in this section.

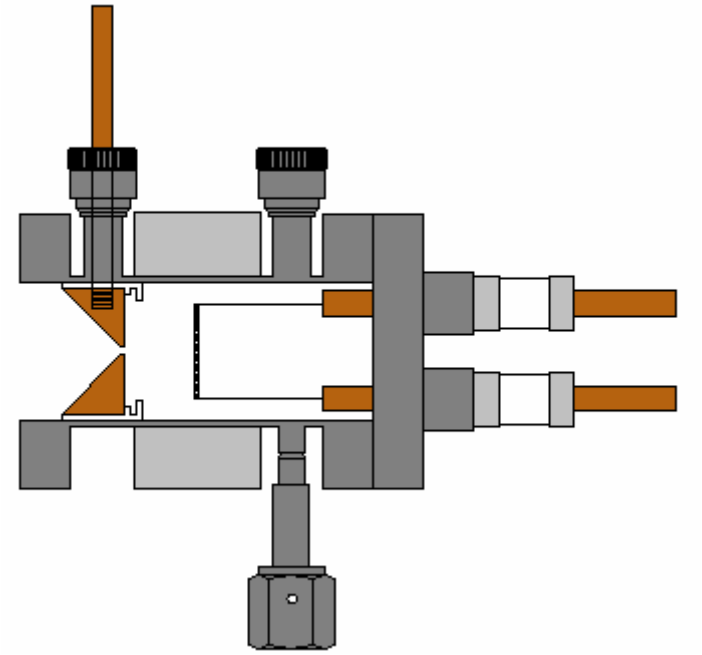

Figure V-5. A side view of the assembled, modified ion source.

V.3 Power Supplies

V.3.A Filament Power

Besides the mechanical redesign of the ion source, changes were necessary to the electrical configuration due to observed limitations with the original layout. First, since the filament was changed to a thinner wire, the increased resistance would have created a higher voltage drop across it for the same current. While the original supply was capable of delivering 50 A, well above what was needed, the voltage limit of 10 V was routinely reached in order to generate a plasma. It was feared that voltage limitation would prevent sufficient current to pass through the thinner filament to

obtain the temperature necessary to strike the plasma. As a result, the filament supply was replaced (HP, Model 6286) with a 24 V, 12 A supply.

V.3.B Cathode Bias

During conversations with other researchers at an international ion source conference, it was suggested that a new power supply be added to the system. This power supply was to bias the filament negatively with respect to the chamber, and is referred to as the filament or cathode bias supply. The effect of this bias was to increase the energy of electrons emitted from the filament, which yielded two advantages. First, the anode required less applied voltage in order to maintain the plasma, thus lowering the overall plasma potential and the power draw on the anode supply. Second, it increased the vibrational state of neutrals in the plasma since the excitation cross section peaks at an electron energy around 40 eV. Since vibrationally excited molecules more readily undergo dissociative attachment, the production of negative ions was enhanced. The power supply selected for the cathode bias was a 60 V, 10 A supply (HP Model 6038A). Figure V-6 shows the updated electrical connections for the source assembly.

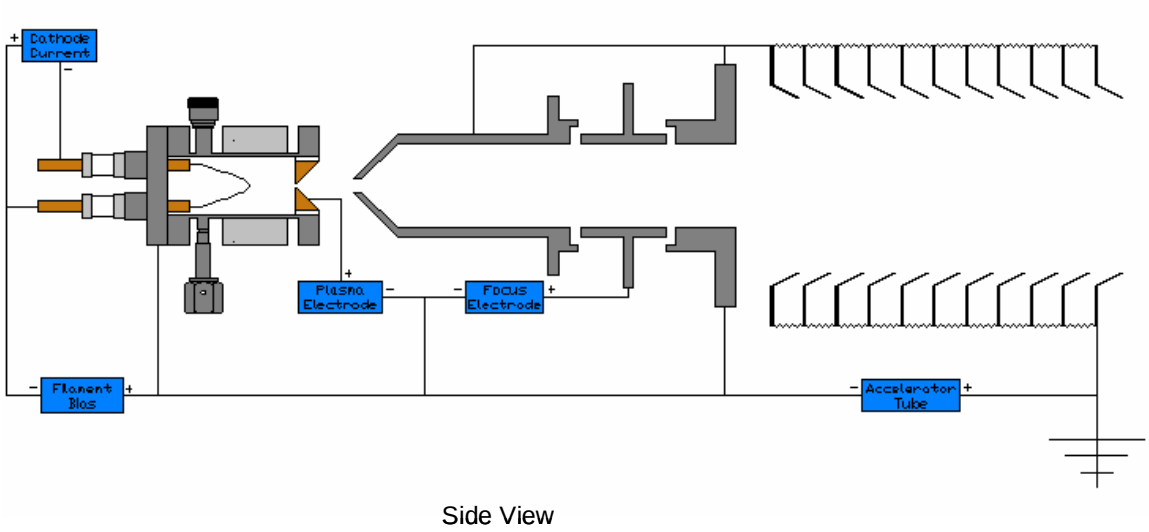

Figure V-6. A schematic drawing of the electrical configuration of the ion source assembly reflecting the addition of the filament bias power supply.

VI Langmuir Probe

VI.1 Background

VI.1.A Theory of Operation

A Langmuir probe is a diagnostic device used to determine several basic plasma parameters, including temperature and density. In the simplest form it consists of a biased thin wire inserted into the plasma. Depending on the specific probe voltage, electrons, ions, or a combination of the two are collected. The collected current is measured as the voltage on the probe is swept positively and negatively to generate an I-V probe trace, an example of which is shown in Figure VI-1. The trace can be broken into three main regions. Starting from the left, the first region is the ion saturation region where the probe has sufficient negative bias that all electrons are repelled and the collected current reflects only ions. As the probe voltage is made more positive, some primary electrons start to be collected, thus causing a slight positive increase in the probe current. The point where the measured current is zero is referred to as the floating potential since the collection of ion and electrons is balanced. Due to the different mobility between ions and electrons, this point is not the same as the plasma potential. The next region is a transition region, where more primary electrons are being collected, and secondary electrons start to be collected. The point at which the trace shifts from the transition region to the next region, the electron saturation region, is the plasma potential. In the electron saturation region, electrons are being collected almost exclusively, and ions are being repelled. The slope in the electron saturation region is steeper than in the ion saturation region because ions are heavier than electrons and not repelled as easily.

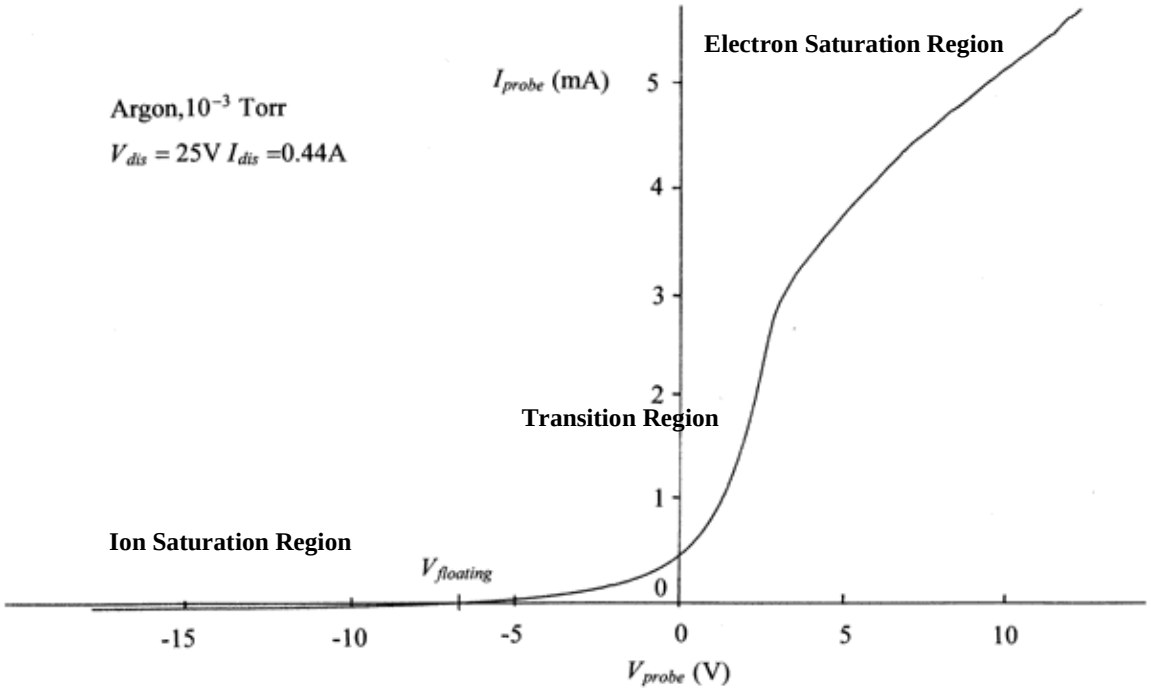

Figure VI-1. A sample Langmuir probe trace.

Analysis of the Langmuir probe trace is performed by first taking the natural logarithm of the probe current and fitting straight lines through the three regions, as shown in Figure VI-2. The plasma potential is given by the voltage at the intersection of the transition region and electron saturation region lines. The current at this point is called the electron saturation current I_{es}. The electron temperature T_e can be inferred from the slope of the line through the transition region which is equal to $\frac{e}{kT_e}$. Once I_{es} and T_e are determined, the plasma density n_e can be calculated from:

$$n_e = \frac{I_{es}}{Ae\sqrt{\frac{kT_e}{2\pi m_e}}}, \qquad \text{(VI-I)}$$

where A is the probe area, e is the charge of an electron, k is the Boltzmann constant, and m_e is the mass of an electron.

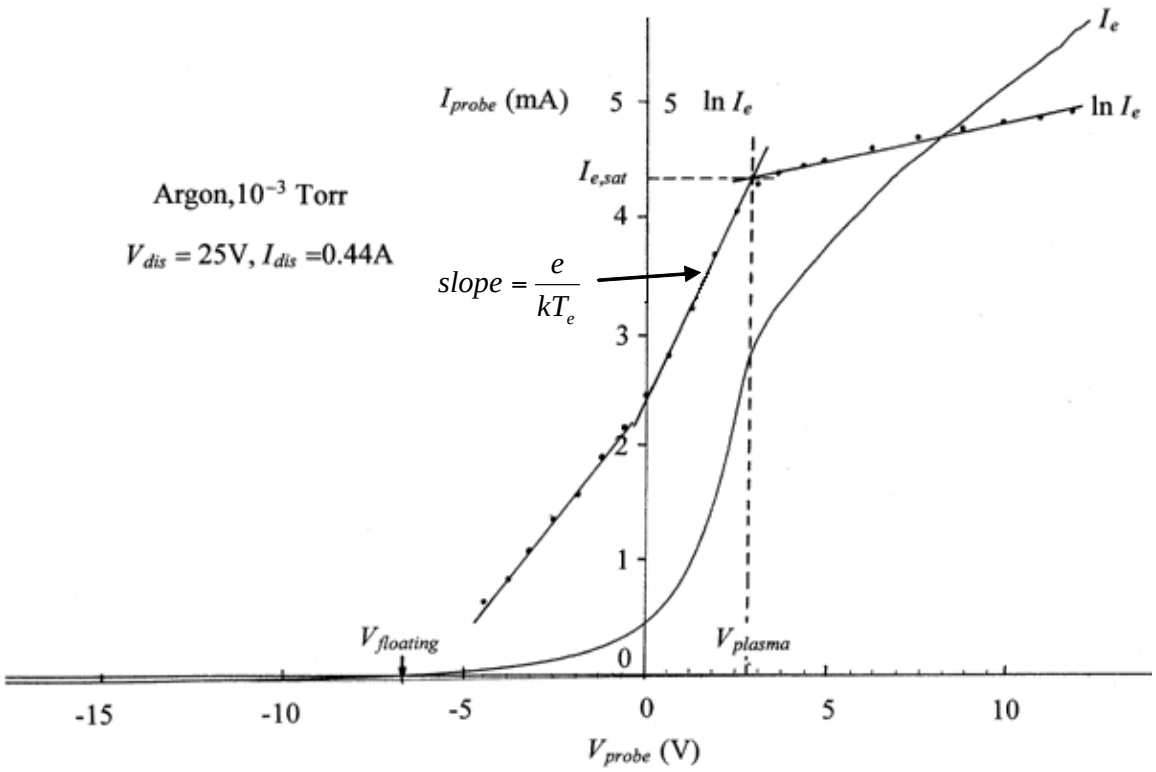

Figure VI-2. The analysis of a Langmuir probe trace.

VI.1.B Construction

The description of the Langmuir probe represents the most general design. More sophisticated probes are commercially available that not only offer more sensitivity and stability, but also allow more thorough analysis to yield additional plasma parameters. However, these probes, and the accompanying analysis packages, are expensive and not necessary for the basic plasma characterization for evaluation of the performance of this ion source. For this reason a simple design was employed, shown in Figure VI-3.

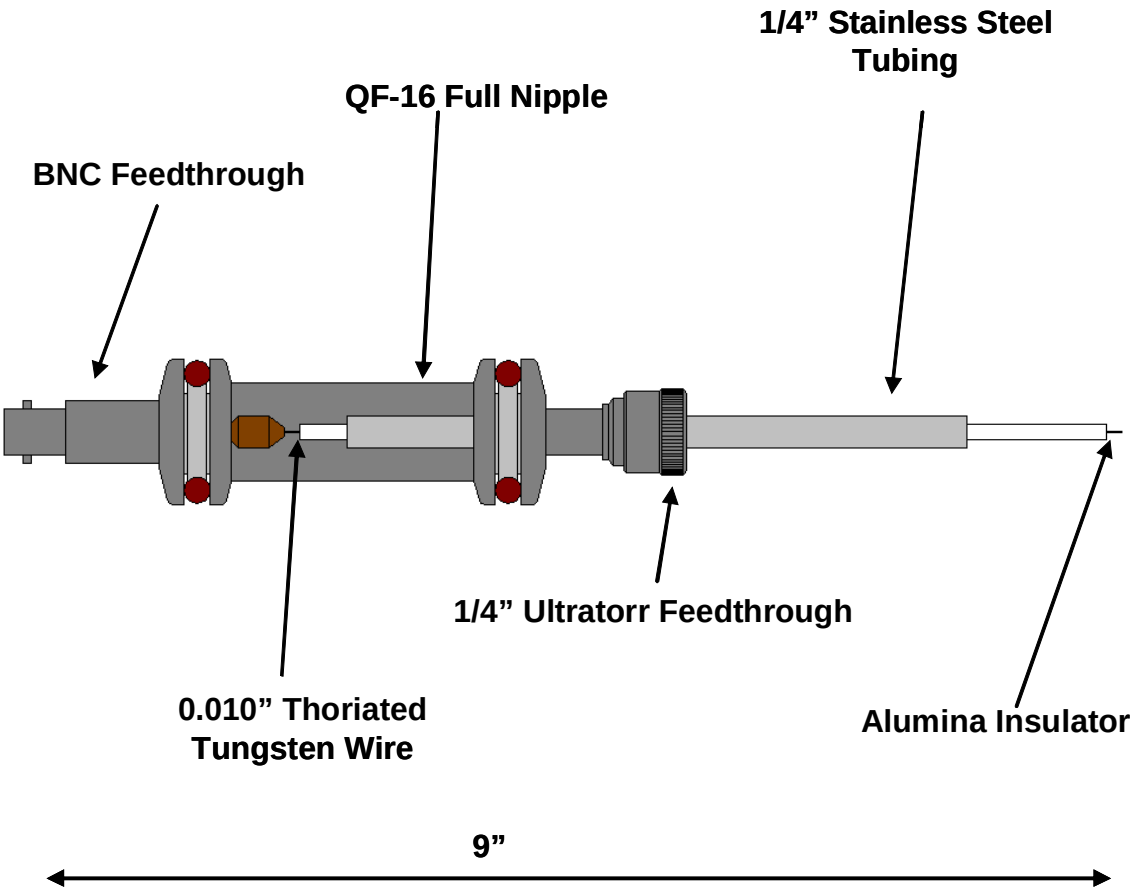

Figure VI-3. The Langmuir probe built to measure basic plasma parameters in the ion source.

The probe consisted of a standard QF-16 full nipple, with a BNC feedthrough flange on one end, and a 1/4” Ultra-Torr fitting flange on the other end. A piece of tungsten wire (0.010”) was attached to the connector pin of the BNC feedthrough and fed through the bore of an alumina insulator. The insulator was then inserted into a length of 1/4” stainless steel tubing that was mounted in the Ultra-Torr fitting. The entire assembly was then inserted into the 1/4” Ultra-Torr feedthrough on the top of the source chamber described in Section III.1.E. The stainless steel tubing not only provided a vacuum connection, but also a reference connection to deck ground. The alumina insulator prevented the tungsten wire from shorting to ground, and allowed only a short length (~ 1/16”) of the wire to be directly exposed to the plasma. It is important

to point out that due to mechanical limitations the probe had to be positioned behind the main spiral portion of the filament, which was not the ideal location since the plasma conditions may be different in this region of the plasma than in the region closest to the plasma electrode. The data obtained from the probe were still instructive in determining general tends of the plasma in the ion source. The probe was instrumented with a Keithley Model 2400 Sourcemeter which allowed for simultaneous biasing of the probe and measurement of the collected current.

VI.2 Data

VI.2.A Effect of Anode Voltage

Several ion source parameters were investigated using the Langmuir probe in order to understand their influence on the behavior of the plasma. Since no provisions were made for operating the Keithley Sourcemeter at high voltage, the following data was taken without powering the extractor, focus, or source bias power supplies. While the plasma behavior will be different in the absence of these supplies, general trends with respect to the key source parameters could be identified. The first parameter investigated was the anode voltage. Figure VI-4 shows the response of T_e and n_e with respect to the anode potential.

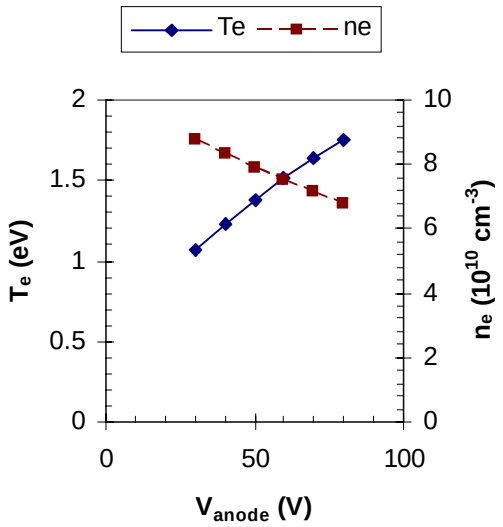

Figure VI-4. The plasma electron temperature T_e and density n_e within the plasma as a function of the anode voltage (Argon: $P_{chamber}$ = 50 mTorr, $V_{cathode}$ = 0 V, $P_{filament}$ = 47.5 W).

As the anode voltage was increased, the potential difference between it and the filament also increased which yielded greater acceleration of the electrons leaving the filament, and hence an increase in T_e. Since the electrons had a higher energy, the likelihood that they will be lost from the plasma to the anode is higher, which is consistent with the increased current collected on the anode shown in Section IV.2. This increased loss of electrons from the plasma resulted in a decrease in n_e since the filament power, and therefore the electron emission, was held constant. As n_e decreased, the plasma potential increased because it contained less negative charge. Since the absolute plasma potential also increased because of the increasing anode voltage, it is more instructive to look at the difference between the plasma potential and the anode potential ΔV, as illustrated in Figure VI-5.

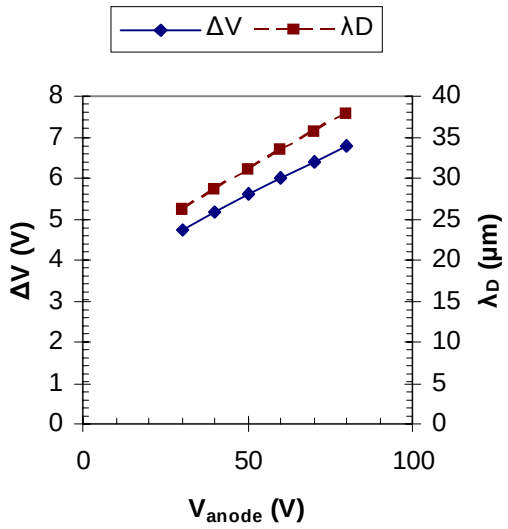

Figure VI-5. The plasma anode potential difference ΔV and the Debye length λ_D as a function of the anode voltage (Argon: $P_{chamber}$ = 50 mTorr, $V_{cathode}$ = 0 V, $P_{filament}$ = 47.5 W).

Another way to explain the behavior of the plasma is to look at the thickness of the plasma sheath, also referred to as the Debye length λ_D which is defined by:

$$\lambda_D^2 = \frac{\varepsilon_0 k T_e}{e^2 n_e}, \tag{VI-2}$$

where ε_0 is the permittivity of free space, k is the Boltzmann constant, and e is the charge of an electron. As T_e increases and n_e decreases, the plasma sheath gets thicker. Since electron extraction can occur only from the plasma sheath, a thicker sheath results in a higher anode current corresponding to a higher electron flux from the plasma which causes the plasma potential to float higher above the anode voltage as observed in Figure VI-5.

VI.2.B Effect of Cathode Voltage

The addition of the cathode bias power supply described in Section V.3 allowed for an alternate means to increase electron energy. As with the anode, T_e

increased with increasing voltage applied to the cathode, as illustrated in Figure VI-6. This plot also shows the corresponding decrease in n_e as more electrons escaped the plasma. Additionally, ΔV and λ_D also increased, as shown in Figure VI-7. While these trends were consistent with the behavior observed from the anode, it is important to point out that the magnitude of the functional behavior was not as great. This feature was due to the fact that the anode provided an external electrostatic field to the plasma, whereas the cathode (filament) was positioned inside the plasma. As the anode voltage was increased the plasma sheath got thicker, not only because the electron temperature increased, but also because there was more potential difference from the anode to pull electrons from the plasma sheath. Alternatively, when the cathode voltage was increased the plasma sheath got thicker only because of the increased electron temperature, thus resulting in a less dramatic functional dependence.

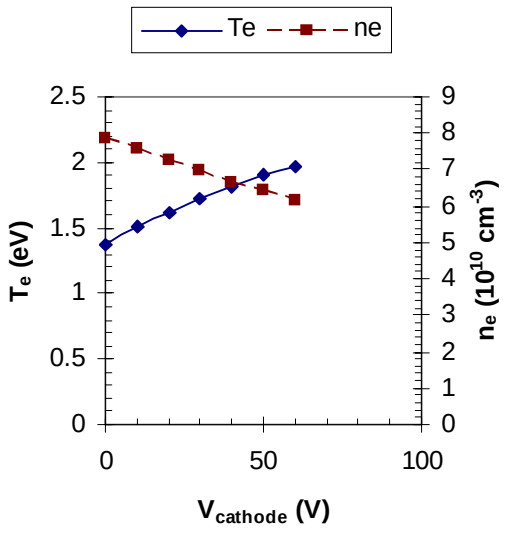

Figure VI-6. The plasma electron temperature T_e and density n_e as a function of the cathode voltage (Argon: $P_{chamber}$ = 50 mTorr, V_{anode} = 50 V, $P_{filament}$ = 47.5 W).

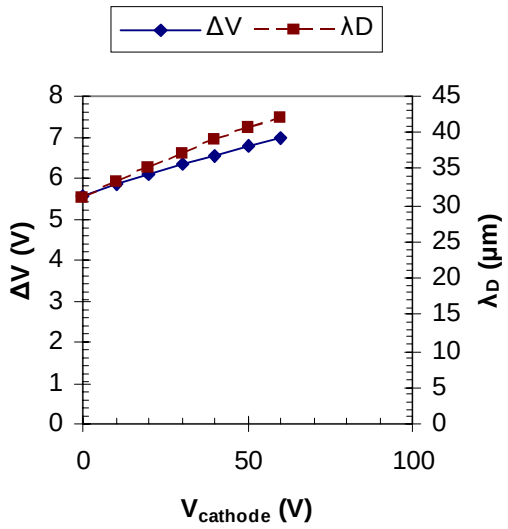

Figure VI-7. The plasma-anode potential difference ΔV and the plasma sheath thickness λ_D as a function of the applied cathode voltage (Argon: $P_{chamber}$ = 50 mTorr, $V_{cathode}$ = 0 V, $P_{filament}$ = 47.5 W).

VI.2.C Effect of Filament Power

Besides the bias applied to it, the current flowed through the filament can be varied. As more current was passed through the filament, the power through it increased as I^2R which resulted in a temperature increase. The resistivity of the filament was not constant, but increased with temperature which magnified the power increase and thus the heating of the filament. Equation II-1 showed that electron emission from a filament increases exponentially with temperature. These two factors made the electron yield from the filament very sensitive to small changes in current.

Figure VI-8 shows the response of T_e and n_e as the filament power was increased. The higher filament temperature resulting from increased power yielded a greater flux of electrons into the plasma which caused a dramatic increase in the electron density. The electron temperature also increased because of the greater voltage drop across the filament as more current was passed through it. The magnitude of this increase

was less than was observed with the anode and cathode voltages. According to Equation IV-2, the increase in electron temperature and density should yield a thinner plasma sheath, as evidenced by Figure VI-9.

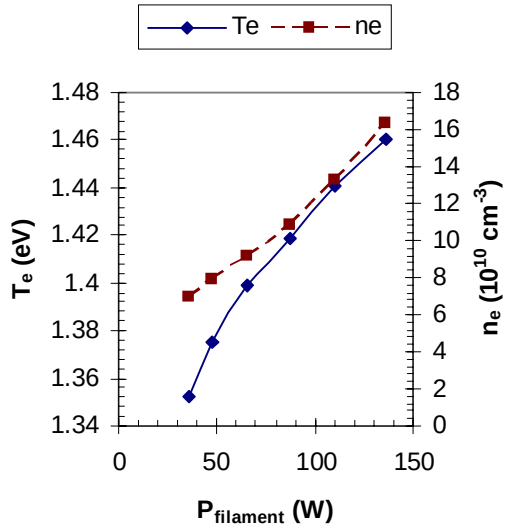

Figure VI-8. The plasma electron temperature T_e and density n_e as a function of filament power (Argon: $P_{chamber}$ = 50 mTorr, $V_{cathode}$ = 0 V, V_{anode} = 0 V).

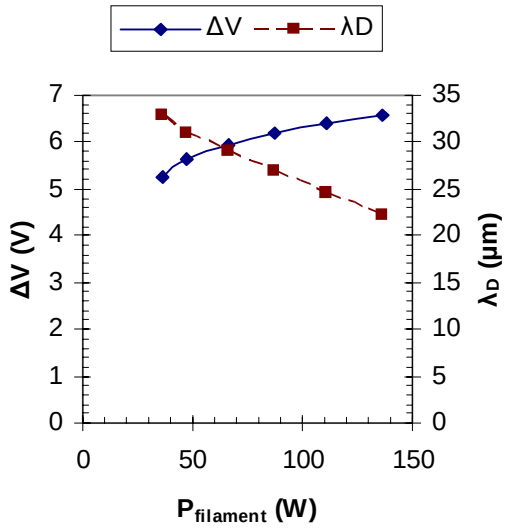

Figure VI-9. The plasma-anode voltage difference ΔV and the plasma sheath thickness λ_D as a function of the filament power (Argon: $P_{chamber}$ = 50 mTorr, $V_{cathode}$ = 0 V, V_{anode} = 0 V).

It was shown in Sections VI.2.A and VI.2.B that as the plasma sheath got thicker, the plasma potential floated higher since more electrons were being extracted from the plasma. However, in those cases the input of electrons was constant since the filament temperature was constant, which was not the case in this test. Even though the plasma sheath was thinner, the plasma potential still increased because of the increased electron density, as shown in Figure VI-9.

VI.2.D Effect of Gas Pressure

Gas pressure is an important parameter in the operation of the source since it is the hardest to control. Whereas the power supplies could be fixed to a specific, reproducible setting, the pressure in the source varied as the flow rate into the chamber changed. As a result, the behavior of the plasma with respect to gas pressure was an important parameter to study. Figure VI-10 shows the response of electron temperature and density in the plasma as a function of the argon pressure in the chamber.

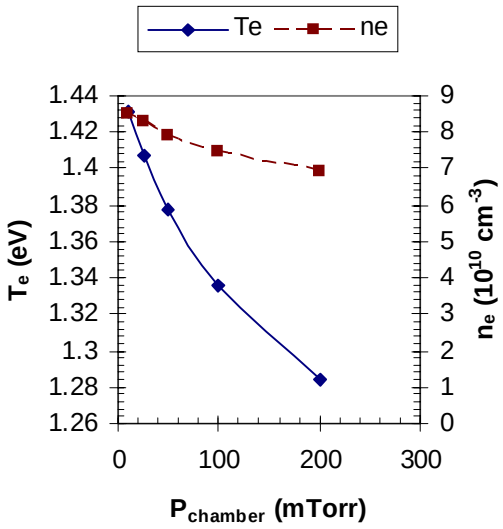

Figure VI-10. The plasma electron temperature T_e and density n_e as a function of argon pressure in the source chamber ($P_{filament}$ = 47.5 W, $V_{cathode}$ = 0 V, V_{anode} = 0 V).

The electron temperature gradually decreased as the pressure was increased due to the presence of more argon atoms which act to cool the electrons. The value T_e is not the exact energy of all electrons in the plasma, but rather a measure of the peak in the Boltzmann distribution. As more argon atoms were introduced into the chamber, more of the lower energy electrons were absorbed via excitation or ionization reactions, effectively lowering T_e. In Sections VI.2.A and VI.2.B it was shown that n_e was inversely related to T_e. In those cases, the chamber pressure was constant, so the probability of an ion-electron interaction was mostly constant. Therefore, an increase in T_e caused more electrons to escape the plasma, resulting in the decrease in n_e. However, as the chamber pressure was increased, the probability of electron adsorption increased which resulted in a decrease in n_e. Since n_e decreased at a faster rate than T_e, λ_D, and therefore ΔV, increased as the chamber pressure was increased, as shown in Figure VI-11. The increase in λ_D resulted in an increase in the anode current, which is consistent with the results described in Section IV.2.

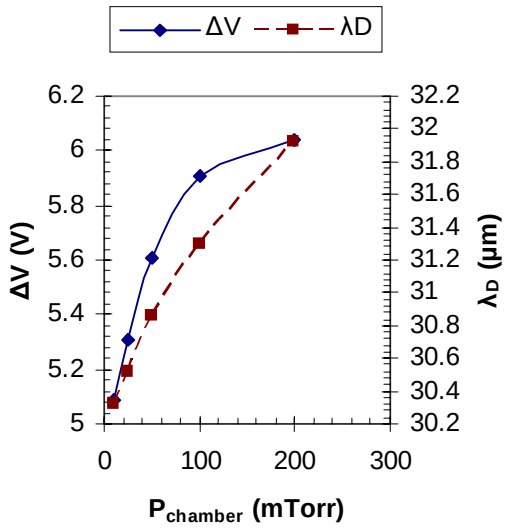

Figure VI-11. The plasma-anode voltage difference ΔV and the plasma sheath thickness λ_D as a function of argon pressure in the source chamber ($P_{filament}$ = 47.5 W, $V_{cathode}$ = 0 V, V_{anode} = 0 V).

VI.2.E Effect of Gas Composition

Besides the pressure in the source chamber, the plasma behavior was also influenced by the specific composition of the gas injected into it. The Langmuir probe measurements thus far have been limited to argon, but were expanded to include nitrogen and carbon dioxide. Studying the behavior of nitrogen showed differences between atomic and molecular species. Since the ion source was developed for production of carbon beams, it was also important to study the behavior of carbon dioxide in plasma as well. Figure VI-12 shows the dependence of T_e on the chamber pressure for these three gases. The most obvious feature of this plot is the electron cooling that appeared for nitrogen and, to a greater extent, for carbon dioxide. Not only was T_e lower for nitrogen than for argon at a given pressure, but the decrease experienced as the pressure increased was more pronounced. This electron cooling effect resulted in a decrease in n_e, as illustrated in Figure VI-13.

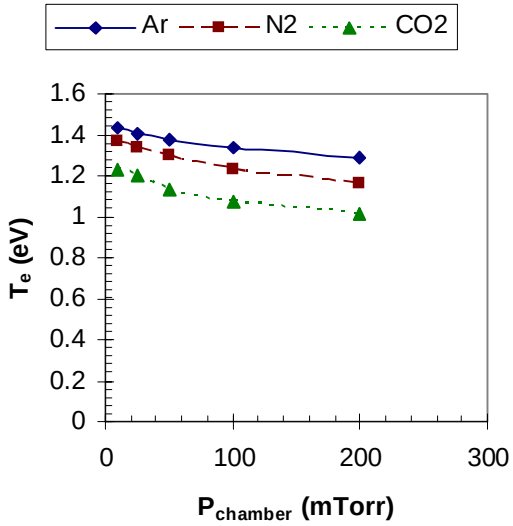

Figure VI-12. The plasma electron temperature T_e with respect to chamber pressure for argon, nitrogen, and carbon dioxide ($P_{filament}$ = 47.5 W, $V_{cathode}$ = 0 V, V_{anode} = 0 V).

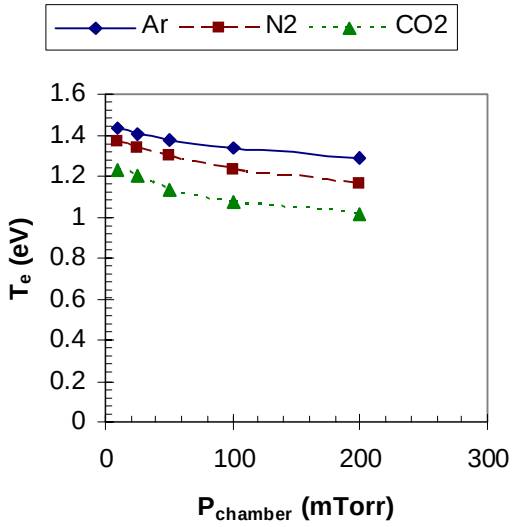

Figure VI-13. The plasma electron density n_e with respect to the chamber pressure for argon, nitrogen, and carbon dioxide ($P_{filament}$ = 47.5 W, $V_{cathode}$ = 0 V, V_{anode} = 0 V).

Since T_e and n_e were both smaller for nitrogen than for argon, and smaller yet for carbon dioxide, the plasma sheath thickness and consequently the plasma-anode potential difference were also smaller, as shown in Figure VI-14 and Figure VI-15. This

feature implies that less current would be collected on the anode, which is in agreement with the results obtained in Section IV.2.

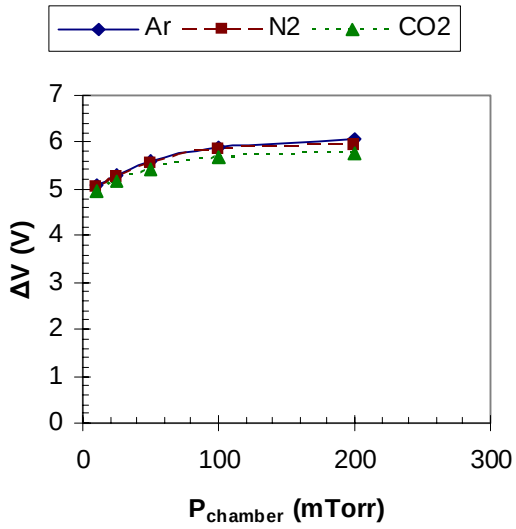

Figure VI-14. The plasma-anode potential difference ΔV with respect to the chamber pressure for argon, nitrogen, and carbon dioxide ($P_{filament}$ = 47.5 W, $V_{cathode}$ = 0 V, V_{anode} = 0 V).

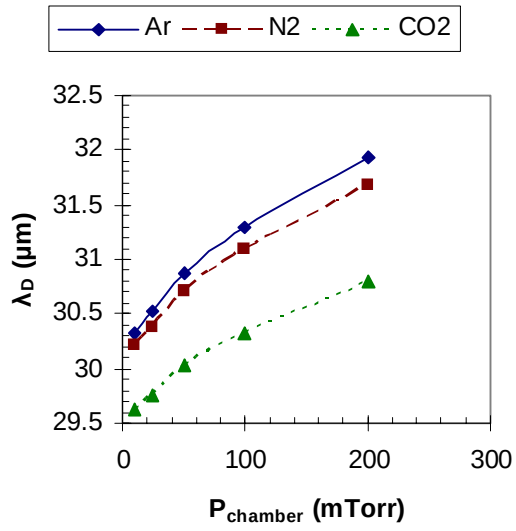

Figure VI-15. The Debye length λ_D with respect to chamber pressure for argon, nitrogen, and carbon dioxide ($P_{filament}$ = 47.5 W, $V_{cathode}$ = 0 V, V_{anode} = 0 V).

VII Ion Source Characterization

VII.1 Positive Ion Mode

VII.1.A Argon

Even though it is intended to produce negative ion beams, it was decided to operate the ion source in positive ion mode for initial diagnosis and characterization. Since positive ions are formed more readily in plasma, the extracted beam will naturally be more intense than the corresponding negative beam. This made it easier to find the beam at each point throughout the testbench. The ion source can be easily switched between positive and negative mode by switching the polarity of the extractor, focus, and source bias power supplies which can be accomplished in less than an hour. The polarity of the switching electrostatic analyzer and the pretzel magnet must also be changed in order for the beam to be properly transported through these components. Additionally, the polarity of the amplifiers used to measure current on the Faraday cups must be reversed. The electrostatic focusing and steering elements of the testbench can retain their normal polarities.

Characterization and diagnosis of the ion source began with investigation of argon since it provides the simplest mass spectrum, an example of which is shown in Figure VII-1, with mass peaks tabulated in Table VII-1. In addition to the expected argon peaks, peaks corresponding to nitrogen and oxygen were observed. It was determined that the presence of these species was due to a leak in the source chamber. Once this leak was identified and repaired, the nitrogen and oxygen peaks disappeared from the mass spectrum, as shown in Figure VII-2, with mass peaks tabulated in Table VII-2.

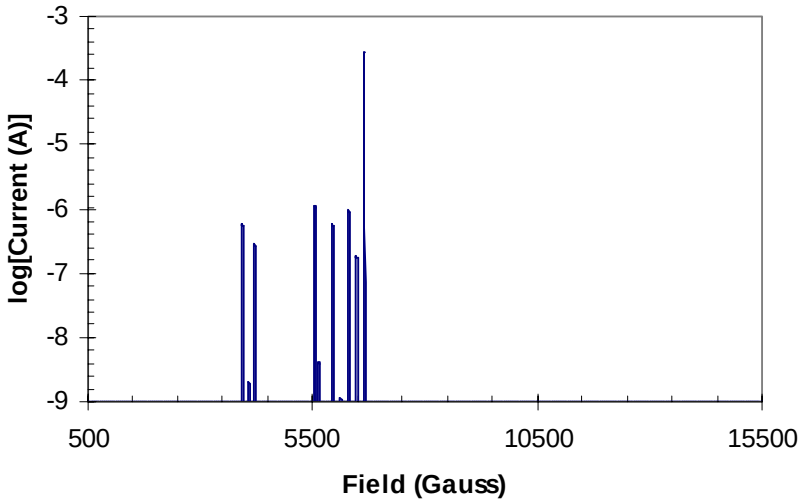

Figure VII-1. Mass Spectrum of argon prior to identification and repair of a leak in the source chamber ($P_{chamber}$ = 50 mTorr; V_{anode} = 50 V; $V_{cathode}$ = 0 V; $P_{filament}$ = 47.5 W).

Table VII-1. List of Peaks in Mass Spectrum Shown in Figure VII-1.

Field (Gauss)	Calculated Mass (amu)	Predicted Species	Intensity (A)
3937.6	13.99	$^{14}N^+$	572n
4069.7	14.96	$^{15}N^+$	2.08n
4208.0	16.02	$^{16}O^+$	285n
5549.4	27.98	$^{14}N_2^+$	1.15μ
5650.8	29.00	$^{14}N^{15}N^+$	4.21n
5939.3	32.02	$^{16}O_2^+$	570n
6124.1	34.02	$^{16}O^{18}O^+$	1.14n
6302.6	36.00	$^{36}Ar^+$	968n
6480.4	38.02	$^{38}Ar^+$	180n
6654.1	40.04	$^{40}Ar^+$	284μ

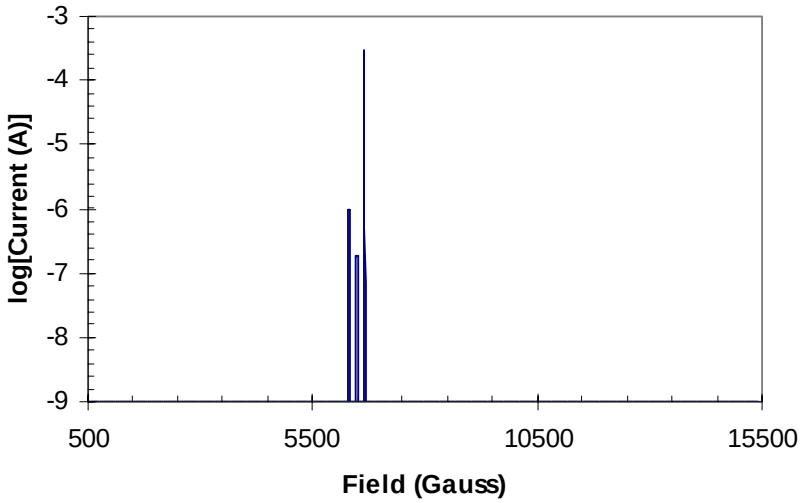

Figure VII-2. Mass spectrum of argon after repair of the leak in the source chamber ($P_{chamber}$ = 50 mTorr; V_{anode} = 50 V; $V_{cathode}$ = 0 V; $P_{filament}$ = 47.5 W).

Table VII-2. List of Peaks in the Mass Spectrum Shown in Figure VII-2.

Field (Gauss)	Calculated Mass (amu)	Predicted Species	Intensity (A)
6301.4	35.98	$^{36}Ar^{+}$	993n
6478.7	38.00	$^{38}Ar^{+}$	188n
6648.9	39.98	$^{40}Ar^{+}$	296μ

It is important to note that the mass spectrum shown in Figure VII-2 was obtained immediately following a thorough cleaning of the ion source. During operation of the ion source, evaporated filament material condenses out on the inner surface of the source chamber, providing a porous medium for gaseous species to adsorb onto. When the ion source is vented for maintenance (e.g. to change a burned out filament), air collects on this surface and does not outgas readily once the chamber is pumped out again. The gas molecules then desorb during operation of the ion source and manifest as interference peaks in the mass spectrum, shown in Figure VII-3 and Table VII-3, which was taken following service to the source. During the characterization and testing phase of this ion source, these interference peaks do not pose a major problem. However, given the sensitivity of the technique, it will be critical to clean the source every time the

chamber is vented in order to ensure high quality AMS measurements. A more important consequence of the adsorption phenomenon is the possibility of cross-contamination of samples which will be investigated later.

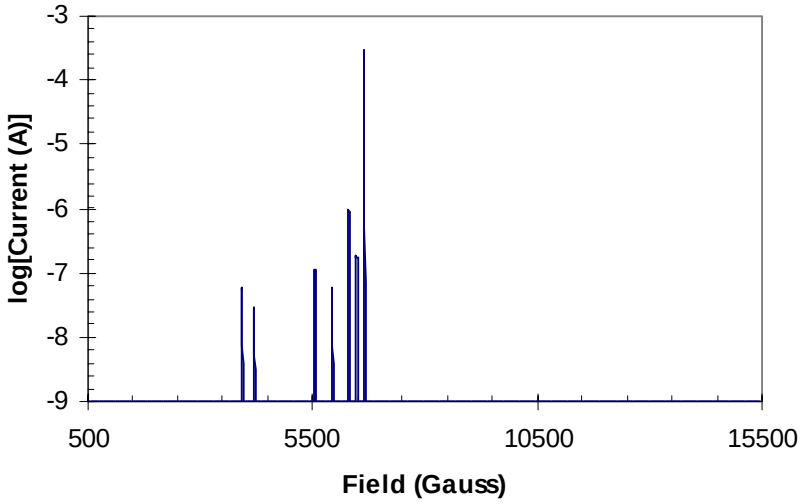

Figure VII-3. Mass spectrum of argon following servicing of the ion source without cleaning ($P_{chamber}$ = 50 mTorr; V_{anode} = 50 V; $V_{cathode}$ = 0 V; $P_{filament}$ = 47.5 W).

Table VII-3. A List of Peaks in the Mass Spectrum Shown in Figure VII-3.

Field (Gauss)	Calculated Mass (amu)	Predicted Species	Intensity (A)
3935.5	13.98	$^{14}N^+$	57.3n
4205.3	16.00	$^{16}O^+$	28.8n
5549.5	27.98	$^{14}N_2^+$	115n
5940.0	32.02	$^{16}O_2^+$	57.7n
6301.7	35.99	$^{36}Ar^+$	975n
6478.0	37.99	$^{38}Ar^+$	183n
6648.1	39.97	$^{40}Ar^+$	288μ

VII.1.B Nitrogen

After initial evaluation with argon, nitrogen was selected for further characterization of the ion source because it is molecular rather than atomic, but produces a simple mass spectrum, as shown in Figure VII-4 and Table VII-4. The first parameter studied was the anode voltage. In the mass spectrum shown in Figure VII-4, the molecular nitrogen peak is much larger than the atomic nitrogen peak which indicates

that the electron temperature T_e in the plasma is too low to cause significant dissociation of the molecular bond. In Section VI.2.A it was shown that increasing the anode voltage results in an increase in T_e. A consequence of this behavior is an increase in the molecular dissociation, as evidenced by Figure VII-5 and Table VII-5 in which the relative intensities of the atomic and molecular nitrogen peaks have been shifted to favor the atomic species. Another important feature is the enhanced overall output from the source which is caused by the thicker plasma sheath λ_D.

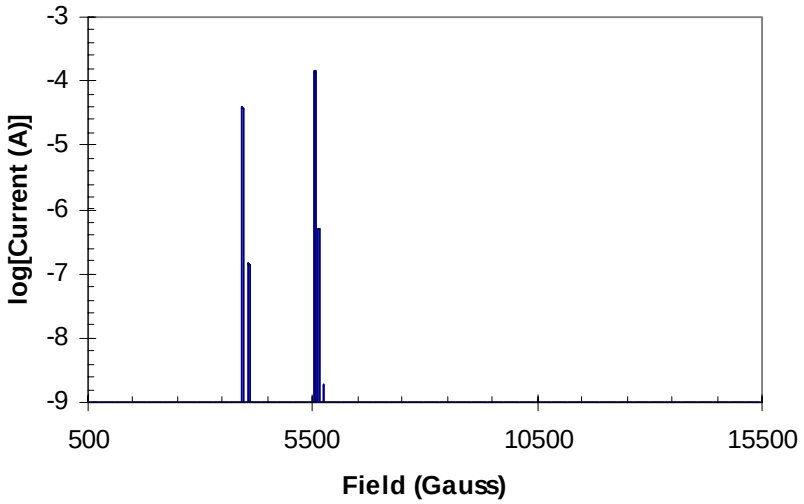

Figure VII-4. Mass spectrum of nitrogen ($P_{chamber}$ = 50 mTorr; V_{anode} = 50 V; $V_{cathode}$ = 0 V; $P_{filament}$ = 47.5 W).

Table VII-4. List of Peaks in the Mass Spectrum Shown in Figure VII-4.

Field (Gauss)	Calculated Mass (amu)	Predicted Species	Intensity (A)
3939.4	14.00	$^{14}N^+$	4.06μ
4071.2	14.98	$^{15}N^+$	148n
5554.6	28.03	$^{14}N_2^+$	142μ
5649.8	28.99	$^{14}N^{15}N^+$	519n
5745.3	29.98	$^{15}N_2^+$	1.92n

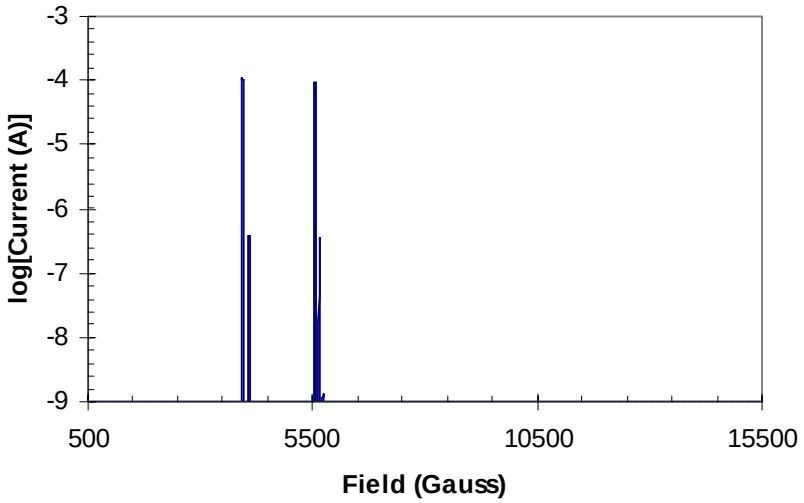

Figure VII-5. Mass spectrum of nitrogen ($P_{chamber}$ = 50 mTorr; V_{anode} = 110 V; $V_{cathode}$ = 0 V; $P_{filament}$ = 47.5 W).

Table VII-5. List of Peaks in the Mass Spectrum Shown in Figure VII-5.

Field (Gauss)	Calculated Mass (amu)	Predicted Species	Intensity (A)
3935.8	13.98	$^{14}N^+$	107μ
4076.0	15.01	$^{15}N^+$	393n
5555.8	28.04	$^{14}N_2^+$	96.0μ
5651.2	29.01	$^{14}N^{15}N^+$	355n
5747.1	29.99	$^{15}N_2^+$	1.30n

Besides the anode voltage, T_e and λ_D are also affected by the cathode voltage. As illustrated in Figure VII-6 and Table VII-6, when the cathode voltage was increased the relative intensities of the molecular and atomic nitrogen peaks shifted to favor the atomic species as was the case with the anode voltage. However, there was a much more dramatic increase in the overall beam output when the cathode voltage was increased. This can be explained by looking at the beam transmission measured at the three Faraday cups in the testbench, as shown in Table VII-7. Beam currents measured at the first and second Faraday cups represent the total output from the source. Beam currents measured at the third (post-pretzel) cup reflects the mass analyzed intensity of

$^{14}N^{+}$. Even though the beam extracted from the ion source was more intense with the higher anode voltage, transmission actually decreased because of poorer focusing caused by the increased plasma potential. Since the plasma potential stays near the anode potential, beam focusing was more uniform as the cathode voltage was increased resulting in more stable transmission.

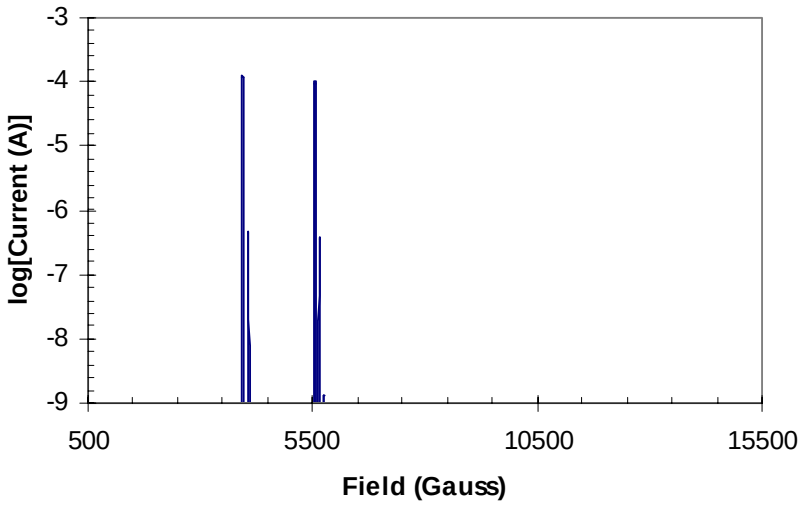

Figure VII-6. Mass spectrum of nitrogen ($P_{chamber}$ = 50 mTorr; V_{anode} = 50 V; $V_{cathode}$ = 60 V; $P_{filament}$ = 47.5 W).

Table VII-6. List of Peaks in the Mass Spectrum Shown in Figure VII-6.

Field (Gauss)	Calculated Mass (amu)	Predicted Species	Intensity (A)
3938.1	14.00	$^{14}N^{+}$	128μ
4076.5	15.02	$^{15}N^{+}$	464n
5553.8	28.02	$^{14}N_2^{+}$	102μ
5651.6	29.01	$^{14}N^{15}N^{+}$	375n
5745.1	29.97	$^{15}N_2^{+}$	1.38n

Table VII-7. Beam Transmission Measured at the Three Faraday Cups in the Ion Source Testbench.

Source Mode	First Faraday Cup Current (A)	Second Faraday Cup Current (A)	Transmission (%)	Third Faraday Cup Current (A)	Transmission (%)
Anode: 50 V Cathode: 0 V	168μ	156μ	92.9	4.06μ	2.60

Anode: 110 V Cathode: 0 V	267μ	221μ	82.8	107μ	45.2
Anode: 50 V Cathode: 60 V	274μ	254μ	92.7	128μ	51.4

VII.1.C Methane

The ultimate goal of this ion source is to produce carbon beams. With previous gas-injection ion sources used for AMS, analytes were passed through an oxidation furnace prior to injection into the ion source. By injecting only carbon dioxide, consistent source behavior was ensured which maximized sample efficiency and instrumental precision. Therefore it was important to investigate the behavior of this ion source with different carbonaceous species to determine if an oxidation furnace will be required. The first species selected for study was methane, a mass spectrum of which is shown in Figure VII-7 with peaks tabulated in Table VII-8. As was the case with nitrogen, the molecular peaks are more intense than the atomic peaks with the anode voltage set to 50 V and no bias on the cathode. When the cathode voltage was increased to 60 V, the relative intensities of these peaks are shifted to favor the atomic species, as evidenced in Figure VII-8 and Table VII-9.

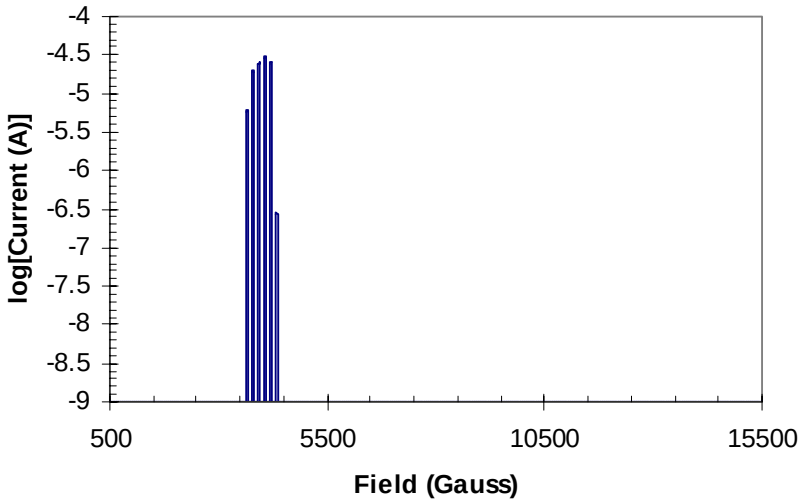

Figure VII-7. Mass spectrum of methane ($P_{chamber}$ = 50 mTorr; V_{anode} = 50 V; $V_{cathode}$ = 0 V; $P_{filament}$ = 47.5 W).

Table VII-8. List of Peaks in the Mass Spectrum Shown in Figure VII-7.

Field (Gauss)	Calculated Mass (amu)	Predicted Species	Intensity (A)
3651.2	11.99	$^{12}C^{+}$	6.19μ
3798.4	13.00	$^{12}C^{1}H^{+}$, $^{13}C^{+}$	19.9μ
3943.3	14.03	$^{12}C^{2}H^{+}$, $^{12}C^{1}H_{2}^{+}$, $^{13}C^{1}H^{+}$	25.5μ
4074.8	15.00	$^{12}C^{1}H^{2}H^{+}$, $^{13}C^{1}H_{2}^{+}$, $^{12}C^{1}H_{3}^{+}$	31.0μ
4208.1	16.02	$^{12}C^{1}H_{2}{}^{2}H^{+}$, $^{13}C^{1}H_{3}^{+}$, $^{12}C^{1}H_{4}^{+}$	26.1μ
4331.8	16.99	$^{12}C^{1}H_{3}{}^{2}H^{+}$, $^{13}C^{1}H_{4}^{+}$	291n

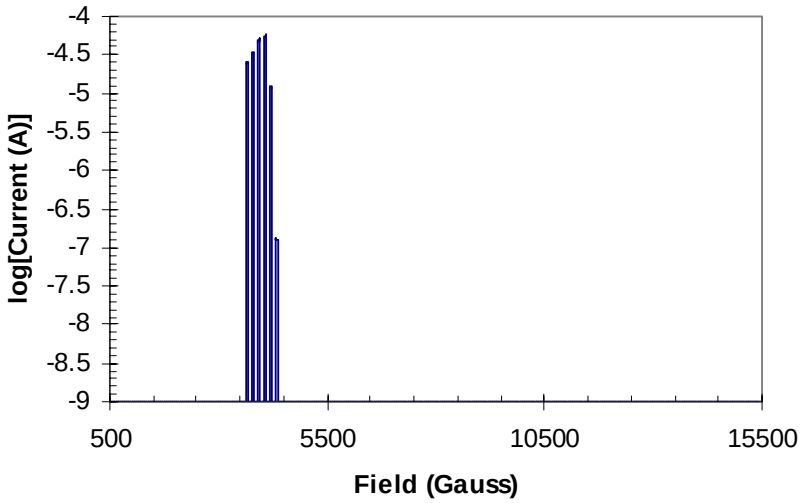

Figure VII-8. Mass spectrum of methane ($P_{chamber}$ = 50 mTorr; V_{anode} = 50 V; $V_{cathode}$ = 60 V; $P_{filament}$ = 47.5 W).

Table VII-9. List of Peaks in the Mass Spectrum Shown in Figure VII-8.

Field (Gauss)	Calculated Mass (amu)	Predicted Species	Intensity (A)
3650.9	11.99	$^{12}C^{+}$	25.7μ
3801.9	13.03	$^{12}C^{1}H^{+}$, $^{13}C^{+}$	34.5μ
3941.1	14.02	$^{12}C^{2}H^{+}$, $^{12}C^{1}H_{2}^{+}$, $^{13}C^{1}H^{+}$	50.7μ
4076.2	15.01	$^{12}C^{1}H^{2}H^{+}$, $^{13}C^{1}H_{2}^{+}$, $^{12}C^{1}H_{3}^{+}$	57.2μ
4207.3	16.01	$^{12}C^{1}H_{2}{}^{2}H^{+}$, $^{13}C^{1}H_{3}^{+}$, $^{12}C^{1}H_{4}^{+}$	12.2μ
4332.5	16.99	$^{12}C^{1}H_{3}{}^{2}H^{+}$, $^{13}C^{1}H_{4}^{+}$	132n

Methane has a couple of drawbacks which may limit its effectiveness for AMS. The first drawback is the presence of significant hydride peaks. Even though the hydrides will be destroyed in the stripper canal of the accelerator, the background observed in the ^{14}C particle detector could be elevated due to the increased stray particles caused by scattering and charge-changing reactions. It might be possible to reduce this effect by using a higher voltage power supply for the cathode bias. This would have the added benefit of increasing the mass usage efficiency of the ion source since fewer carbon atoms would be tied up by molecules.

Another feature affected the performance of methane. It was noticed that the plasma was much more unstable during operation of the ion source with methane. While Figure VII-7 and Figure VII-8 represent the best data collected, it was difficult to obtain an entire mass spectrum without the anode power supply sporadically shorting to ground over the course of the measurement (~10 min). Upon dismantling the ion source, a thick layer of ash was observed on the inner surfaces. Presumably, some of the methane was combusting around the periphery of the plasma and forming a conducting path of carbon between the chamber body and the plasma electrode. This phenomenon presents a serious problem in the consistent operation of the ion source for AMS. It is possible that the impact of this difficulty would be lessened if samples were introduced into the ion source with a carrier gas thus lowering their overall concentration in the chamber.

VII.1.D Carbon Dioxide

The final species selected for study in positive ion mode was carbon dioxide since it has been the most successful carbonaceous substance used in gas-injection ion sources for AMS. A mass spectrum of carbon dioxide is shown in Figure VII-9 with peaks tabulated in Table VII-10. As was the case with nitrogen and methane, the atomic carbon peaks are less intense than the molecular oxide peaks. It was shown with nitrogen and methane that as the cathode voltage was increased, the relative intensities of the peaks shifted to favor the atomic rather than molecular species. This same trend was observed with carbon dioxide and the magnitude of the effect was measured by the ^{12}C to $^{12}C^{16}O_2$ ratio, as shown in Figure VII-10. While a cathode voltage of 60 V yielded atomic carbon peaks that were more intense than the molecular

oxide peaks, a significant portion of carbon atoms were still bound in the molecules. Increasing the cathode voltage further would increase the electron temperature in the plasma and therefore dissociate more of the molecules, thus increasing the atomic carbon fraction. However, the plot in Figure VII-10 shows that increasing the cathode voltage beyond 60 V yields diminishing returns on the enhancement of the atomic peaks. This feature is directly related to the behavior of the electron temperature with respect to the cathode voltage discussed in Section VI.2.B.

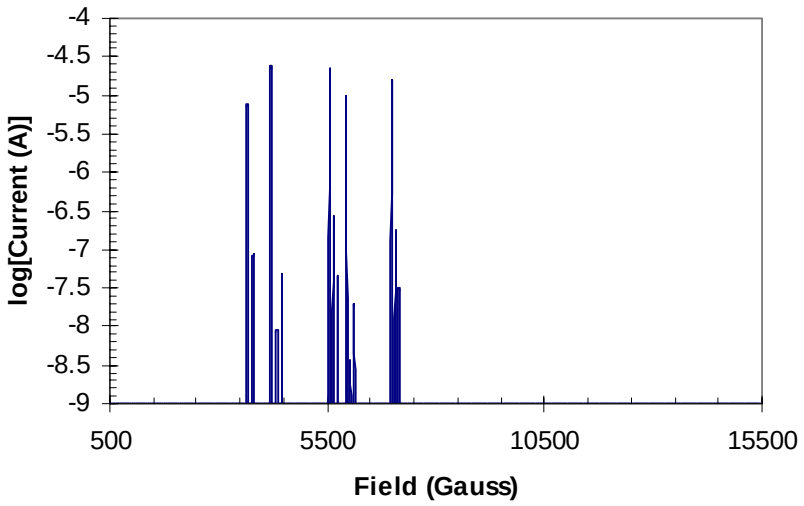

Figure VII-9. Mass spectrum of carbon dioxide ($P_{chamber}$ = 50 mTorr; V_{anode} = 50 V; $V_{cathode}$ = 0 V; $P_{filament}$ = 47.5 W).

Table VII-10. List of Peaks in the Mass Spectrum Shown in Figure VII-9.

Field (Gauss)	Calculated Mass (amu)	Predicted Species	Intensity (A)
3651.5	11.99	$^{12}C^{+}$	7.80µ
3799.3	13.01	$^{13}C^{+}$	87.1n
4205.5	16.00	$^{16}O^{+}$	24.3µ
4332.3	16.99	$^{17}O^{+}$	9.15n
4454.3	17.98	$^{18}O^{+}$	48.8n
5550.0	27.98	$^{12}C^{16}O^{+}$	23.0µ
5649.3	28.99	$^{12}C^{17}O^{+}$, $^{13}C^{16}O^{+}$	270n
5748.0	30.00	$^{12}C^{18}O^{+}$	46.6n
5938.7	32.01	$^{16}O_2^{+}$	9.82µ

6033.0	33.02	$^{16}O^{17}O^{+}$	3.78n
6119.7	33.97	$^{16}O^{18}O^{+}$	19.8n
6980.4	43.96	$^{12}C^{16}O_2^{+}$	15.7μ
7073.9	45.11	$^{12}C^{16}O^{17}O^{+}$, $^{13}C^{16}O_2^{+}$	183n
7149.1	46.05	$^{12}C^{16}O^{18}O^{+}$	31.6n

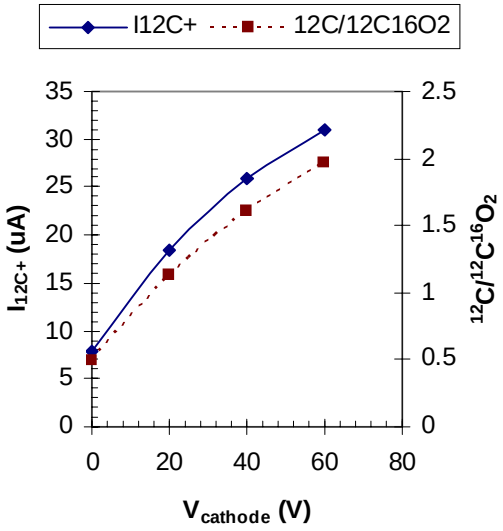

Figure VII-10. The $^{12}C^{+}$ and ^{12}C to $^{12}C^{16}O_2$ ratio as a function cathode voltage for carbon dioxide ($P_{chamber}$ = 50 mTorr; V_{anode} = 50 V; $P_{filament}$ = 47.5 W).

Besides the anode and cathode voltages, the influence of filament power on ion source behavior was also investigated, as shown in Figure VII-11. As more power was passed through the filament, the overall output from the source increased since the electron density in the plasma increased, which resulted in an enhancement in the $^{12}C^{+}$ current. As illustrated in Section VI.2.C, the electron temperature also increased slightly with more filament power, which resulted in a slight increase in the ^{12}C to $^{12}C^{16}O_2$ ratio causing a further enhancement of the $^{12}C^{+}$ current. Since the overall filament power was limited by insufficient cooling, this trend represents a potential source of significant increase in the performance of the ion source.

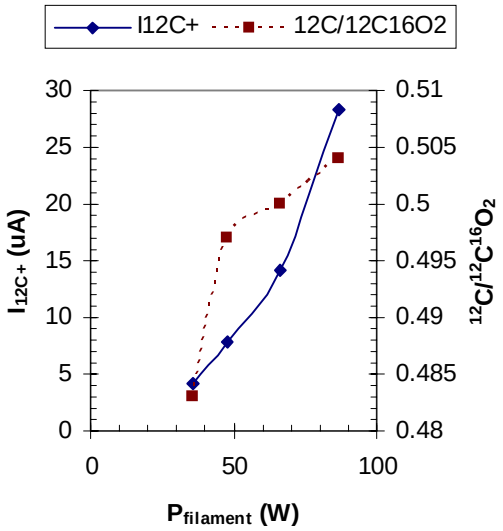

Figure VII-11. The $^{12}C^{+}$ current and the ^{12}C to $^{12}C^{16}O_2$ ratio as a function of filament power ($P_{chamber}$ = 50 mTorr; V_{anode} = 50 V; $V_{cathode}$ = 0 V).

In contrast to the filament power, as the gas pressure in the source chamber was increased, the overall beam output from the ion source decreased since the electron density in the plasma decreased, as shown in Section VI.2.D. Additionally, the plasma electron temperature decreased resulting in a decrease in the ^{12}C to $^{12}C^{16}O_2$ ratio which also contributed to the lower $^{12}C^{+}$ current. This trend indicates that running the ion source with lower chamber pressure should result in higher mass efficiency, a conclusion that will be evaluated later in this chapter.

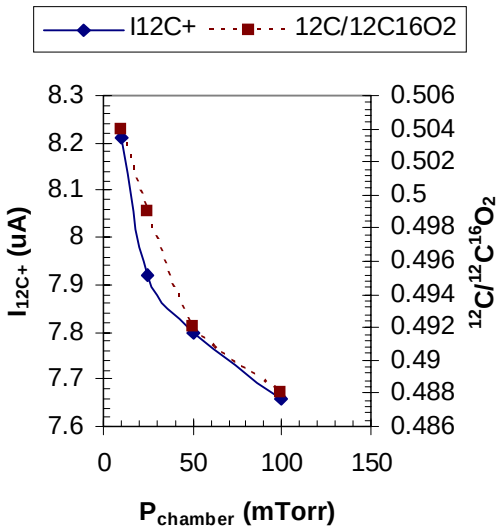

Figure VII-12. The $^{12}C^{+}$ current and the ^{12}C to $^{12}C^{16}O_2$ ratio as a function of chamber pressure (V_{anode} = 50 V; $V_{cathode}$ = 60 V; $P_{filament}$ = 47.5 W).

VII.2 Negative Ion Mode

VII.2.A Sample Injection Manifold

After diagnosing the ion source and characterizing its behavior in positive ion mode, the bias was reversed on the power supplies and current amplifiers (see Section VII.1.A) so that negative ion beams could be extracted and measured from the ion source. Of the gases studied, only methane and carbon dioxide are of interest since nitrogen and argon do not form stable negative ions. Furthermore, since methane was problematic, it was decided to focus on the performance of the ion source with carbon dioxide.

Characterization of the ion source thus far has been limited to loading the source chamber with a specific pressure of a single gas using the 1/4" Swagelok port described in Section III.1.E. In order to further evaluate the performance of the ion source, a sample injection manifold was built. This manifold consisted of two MKS Model 2159B (10 sccm N_2 range) mass flow controllers connected in parallel. A lecture bottle fitted with a dual stage regulator was attached to the input and a shut-off valve was

installed on the output of each flow controller. While these flow controllers were designed to control mass flow down to 1% of full scale, it was impossible to operate them below about 20% of full scale because even with the control valve overridden to the fully closed position, a flow rate of ~2 standard cubic centimeters per minute (scccm) of N_2 was observed. It is not clear whether this represented a design flaw or a mechanical defect with these particular devices. In order to allow flow control below this limit, a throttle valve was installed following the junction between the two flow controllers. By fixing the control valve of one of the controllers in the fully open position, the maximum flow rate into the source chamber could be fixed by adjusting the throttle valve. With the maximum flow rate fixed to 2 sccm N_2, the flow controllers were able to control down to their specified value of 0.1 sccm N_2. Approximately 1 m of methyl-deactivated glass fused silica capillary tubing (ID = 0.53 mm, OD = 0.68 mm) was connected to the throttle valve and fed up to the 1/16" Ultra-Torr fitting on the source body.

The setup of this manifold allowed for injection of a known flow rate of gas into the source chamber which allowed several important measurements. The first important benefit of this manifold was the ability to inject a known flow rate of gas into the ion source. Up to this point, the performance of the source could only be quantified by the intensity of the extracted ion beam. While maximizing the intensity of the ion beam is important for rapid AMS measurements, of equal importance is the mass efficiency. By injecting a known flow of sample gas into the ion source it was possible to calculate the mass efficiency of the ion source. The second benefit of the sample injection manifold was the ability to inject gas mixtures with specific mixing ratios. This allowed for evaluation of ion source performance with carbon dioxide in the presence of

inert carrier gases, such as helium, which simulated the composition of an effluent from a gas chromatograph. Finally, the manifold allowed for the carbon dioxide stream to be quickly turned off in order to evaluate the memory effect characteristics of the ion source.

VII.2.B Mass Efficiency

The mass efficiency of the ion source is defined as the number of $^{12}C^-$ ions that are extracted from the ion source compared to the number of molecules of CO_2 that are injected per unit time, and is calculated by:

$$Efficiency = \frac{1.0112 I_{^{12}C^-}}{e} \cdot \frac{60RT}{0.7 N_A F}, \qquad \text{(VII-1)}$$

where $I_{^{12}C^-}$ is the $^{12}C^-$ current measured at the Faraday cup following the pretzel magnet, e is the charge of an electron, R is the ideal gas constant, T is the temperature, N_A is Avogadro's number, and F is the flow rate of gas into the ion source. Since the beam current is measured in amperes and the flow rate has units of sccm N_2, the factor 60 is needed to match the time units. Additionally, the gas correction factor 0.7 is needed to convert the flow rate from units of sccm N_2 into sccm CO_2. Finally, the factor 1.0112 accounts for the isotopic abundance of ^{12}C.

The behaviors of $^{12}C^-$ current and the calculated mass efficiency with varying flow rates of CO_2 injected into the source are shown in Figure VII-13. Since beam intensity shows a strong dependence on filament power, the ion source was operated with a filament power of 87 W. The current decreased with increasing flow rate, which resulted in an exponential decrease in mass efficiency due to the form of Equation IV-1. This behavior is expected since there is a constant ionization rate within a static plasma. As the flow rate of CO_2 molecules was increased this ionization rate

changed very little, so most of the additional CO_2 flux was simply pumped away without being ionized, thus lowering the overall efficiency.

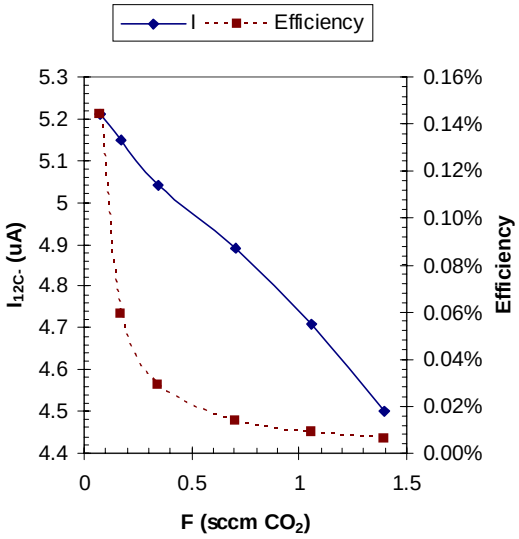

Figure VII-13. The $^{12}C^-$ current and the calculated mass efficiency as a function of the flow rate of CO_2 injected into the source (V_{anode} = 50 V; $V_{cathode}$ = 60 V; $P_{filament}$ = 87 W).

The decrease in beam intensity was also expected because of the influence of chamber pressure illustrated in Section VII.1.D. The increased flow rate caused an increase in chamber pressure which cooled the plasma and decreased beam output. While the chamber pressure was not monitored directly during this experiment, it can be estimated from the following:

$$P_{chamber} = \frac{0.7F}{C} \tag{VII-2}$$

where F is the flow rate and C is the conductance of the plasma electrode aperture. Again, the gas correction factor 0.7 is needed since the flow rate is measured in units of sccm N_2. The conductance of the plasma electrode aperture can be estimated by:

$$C = 3.64A\sqrt{\frac{T}{M}} \tag{VII-3}$$

where A is the area of the aperture, T is the temperature, and M is the molecular weight. By using Equations IV-2 and IV-3, the abscissa in Figure VII-13 can be transformed into chamber pressure, as shown in Figure VII-14. This plot shows the same dependence of beam intensity on chamber pressure, as illustrated earlier in Figure VII-12.

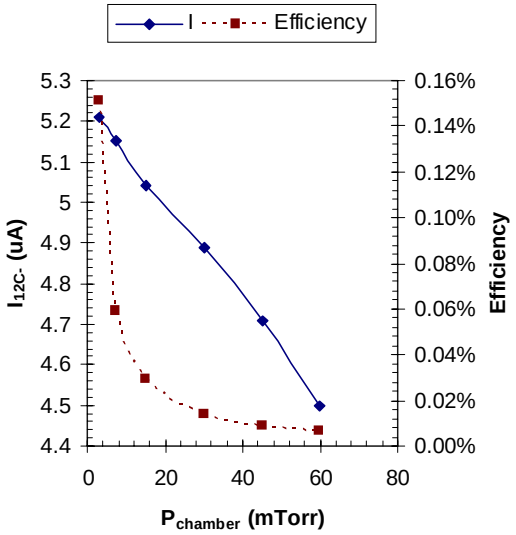

Figure VII-14. The $^{12}C^-$ current and the calculated mass efficiency as a function of the calculated pressure in the source chamber (V_{anode} = 50 V; $V_{cathode}$ = 60 V; $P_{filament}$ = 87 W).

VII.2.C Mixing Ratios

An important use for this ion source will be the coupling to the output of a gas chromatograph. These effluents are composed of a small fraction of a sample entrained with an inert carrier gas such as helium. Other ion source designs have used an on-line sample concentration technique, such as jet enrichment in order to minimize the carrier gas that was injected into the source chamber. This step was necessary to maximize sample ionization efficiency, so it was important to investigate the influence of carrier gas on the performance of this ion source. To accomplish this, carbon dioxide was injected into the ion source with a stream of helium by the gas manifold described in Section VII.2.A. By keeping the carbon dioxide flow constant, the mixing ratio of carbon

dioxide to helium was varied by adjusting the flow of helium. It was important to keep the carbon dioxide flow constant so that its influence on mass efficiency shown in Section VII.2.B did not interfere with this measurement.

The dependence of both beam current and mass efficiency on the mixing ratio is shown in Figure VII-15. While helium is a very poor negative ion producer, helium atoms compete for plasma electrons, which resulted in a dramatic drop-off in both $^{12}C^-$ current and efficiency as the mixing ratio approached the level found in the effluent of a gas chromatograph. At higher values of the mixing ratio the mass efficiency began to approach the value obtained for pure CO_2. Despite having a limited range of mixing ratio due to the limited control range of the flow controllers, it is clear that sample enrichment is necessary in order to maximize the mass efficiency of the ion source. Increased CO_2 flow rates would have been required to investigate higher mixing ratios, but the data would have been convoluted with the negative effect of flow rate on mass efficiency discussed in Section VII.2.B.

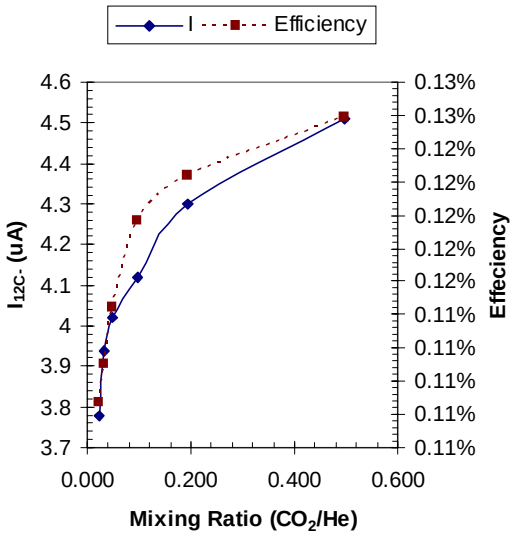

Figure VII-15. The $^{12}C^-$ current and the calculated mass efficiency as a function of the mixing ratio of CO_2 to He injected in the source chamber for a constant flow rate of 0.1 sccm CO_2 (V_{anode} = 50 V; $V_{cathode}$ = 60 V; $P_{filament}$ = 87 W).

VII.2.D Memory Effects

Another key performance parameter is the magnitude of memory effects between injections of sample into the ion source. There are two main concerns regarding memory effects. The first concern is the decay time of the signal from the ion source following sample injection. A long decay time would make it difficult for the ion source to be coupled to the output of a gas chromatograph since the retention time of individual analytes would have to be quite different in order to prevent overlapping of peaks. The second concern is background elevation caused by buildup of sample material in the ion source. The impact of these two features was investigated using the sample injection manifold described earlier. By flowing a fixed rate of helium into the ion source, a static plasma discharge was created. Injections of carbon dioxide were made by opening the mass flow controller for approximately five seconds. The resulting $^{12}C^-$ current on the Faraday cup following the pretzel magnet was recorded.

Figure VII-16 shows the signal obtained from a single injection of carbon dioxide into the ion source. There was a very quick response followed by an exponential decay taking about 20 seconds to return to baseline. Upon closer inspection, it was noticed that the decay was not a simple one-component exponential, but rather appeared to have two contributing influences, as shown in Figure VII-17. It is interpreted that this behavior reflects the time necessary for the carbon dioxide to flow through the length of the capillary tube between the manifold and the ion source. Additionally, during this time, the mixing ratio of carbon dioxide to helium was decreasing which influenced the mass efficiency of the ion source. These two factors resulted in the convoluted exponential decay observed.

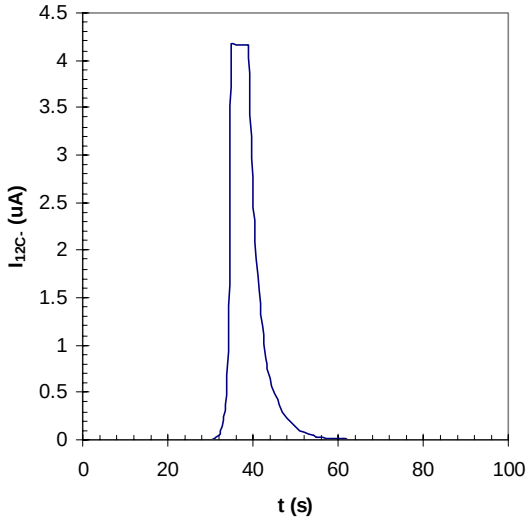

Figure VII-16. The $^{12}C^-$ current pulse resulting from a 5-second injection of carbon dioxide into the ion source with a constant flow of helium (F_{He} = 0.146 sccm He, F_{CO2} = 0.072 sccm CO_2, V_{anode} = 50 V; $V_{cathode}$ = 60 V; $P_{filament}$ = 87 W).

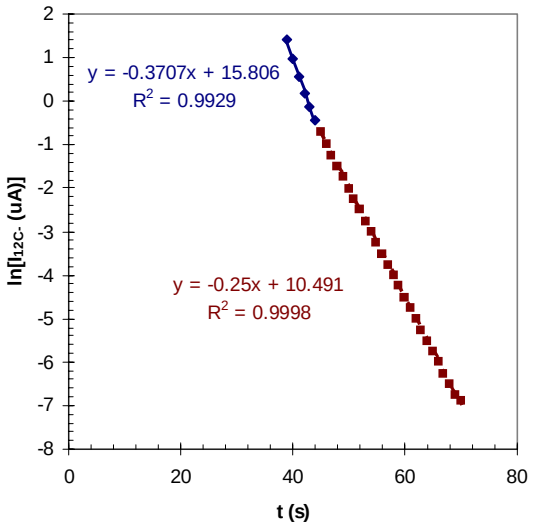

Figure VII-17. The two decay components of the signal pulse shown in Figure VII-16.

The next effect studied was the background elevation effect. This was accomplished observing the impact of repeated injections of carbon dioxide into the ion source, as shown in Figure VII-18. While each of the peaks showed the decay pattern observed previously, there was no apparent increased in the baseline of the Faraday cup signal. It is important to note however, that the threshold for the log-amp used with this Faraday cup was 1 nA. So it is possible that there was an increase in the baseline that was too small to be detected on this Faraday cup, but would be large enough to interfere with the measurement of ^{14}C for AMS.

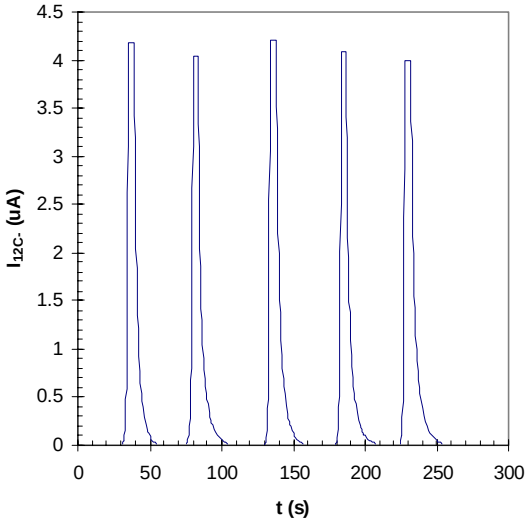

Figure VII-18. The $^{12}C^-$ current pulses resulting from repeated injections of carbon dioxide into the ion source with a constant flow of helium (F_{He} = 0.146 sccm He, F_{CO2} = 0.072 sccm CO_2, V_{anode} = 50 V; $V_{cathode}$ = 60 V; $P_{filament}$ = 87 W).

In previous tests it was noticed that after venting the source following operation, filament material deposited on the inside of the source chamber would trap air which would later show up as interference peaks in the mass spectra. While the pressure in the source chamber during operation is orders of magnitude below atmospheric pressure, it was important to determine if sample gas would adsorb onto the inside of the chamber and interfere with subsequent samples. Figure VII-16 and Figure VII-18 have shown the $^{12}C^-$ current in response to short injections of carbon dioxide so it is possible that there was not enough material to create a noticeable increase in the background signal. Therefore, the effect of an injection of ~30 minutes rather than 5 seconds was investigated, as shown in Figure VII-19. The long term decrease in current observed during the 30-minute injection reflected the degradation of the filament. The decay following termination of the injection was much longer than with the 5-second injections and, as shown in Figure VII-20, the decay was again a multi-component exponential. As opposed to the short injection case where the decay appeared to have two components,

there were three apparent components in this decay. The third component most likely corresponds to desorption of carbon dioxide from the inner surface of the chamber. While in practice, injections from a gas chromatograph would be closer to 5 seconds than 30 minutes, this behavior could pose a memory effect problem for doing AMS. Further investigation is clearly necessary.

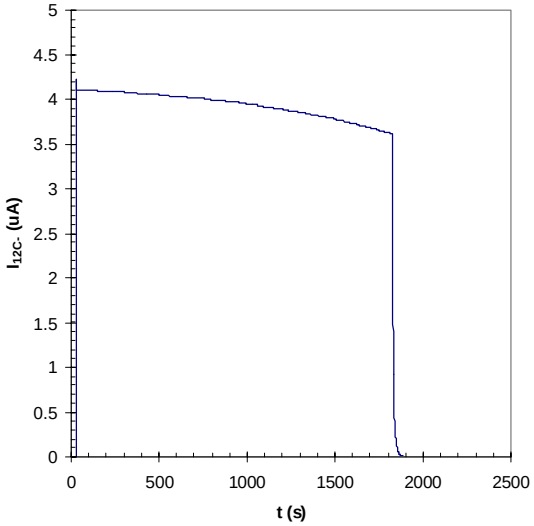

Figure VII-19. The $^{12}C^-$ current profile resulting from a continuous flow of carbon dioxide with helium into the ion source for approximately 30 minutes with subsequent decay after the carbon dioxide flow was stopped (F_{He} = 0.144 sccm He, F_{CO2} = 0.073 sccm CO_2, V_{anode} = 50 V; $V_{cathode}$ = 60 V; $P_{filament}$ = 87 W).

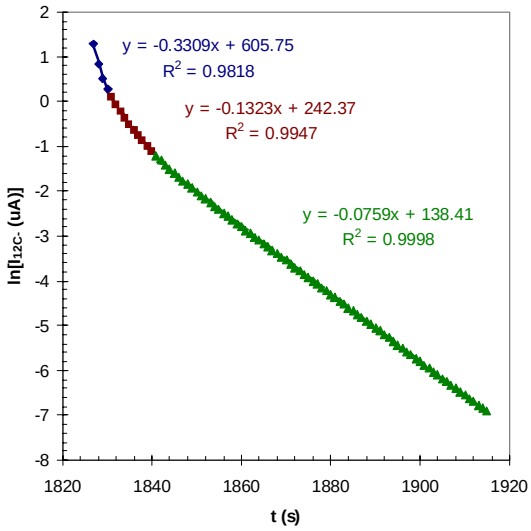

Figure VII-20. The three components the decay of the signal shown in Figure VII-19.

VII.2.E Magnetic Confinement

All of the measurements presented so far were taken without the use of magnetic confinement. By installing permanent magnets to form a multi-cusp pattern as described in Section II.3.B, the performance of the ion source should be greatly improved because of the increased electron density. However, the opposite effect was observed. For example, when the ion source was operated with typical parameters (F_{CO2} = 0.072 sccm CO_2, V_{anode} = 50 V; $V_{cathode}$ = 60 V; $P_{filament}$ = 87 W), the $^{12}C^-$ beam current decreased from 4.2 μA to 2.7 μA when the magnets were installed. This result was very troubling and a significant effort was made to ascertain the cause.

It was determined that during the modification of the source described in Section V.1.C, the chamber became out of round. This prevented the plasma electrode aperture from being radially centered within the chamber, and therefore caused a misalignment with respect to the aperture on the extractor cone. Upon sighting down the beamline, it was observed that, while the extractor cone aperture was perfectly in line

with the rest of the beamline, the plasma electrode aperture was approximately 3 mm below the axis of the beamline.

This misalignment explains the vertical steering that was required to optimally tune the beam through the system. It also explains the decrease in beam current observed in the presence of the magnets. The multi-cusp field confined the plasma electrons, thus concentrating them in the center of the chamber. However, ions could only be extracted from the region of the plasma surface that the plasma electrode aperture projected onto. Since the plasma electrode was 3 mm below the center of the chamber, the plasma electron density in that region was not at a maximum which resulted in a less intense ion beam. This hypothesis was tested by installing the magnets in a quadrupole rather than octopole arrangement. While the four magnets still created a multi-cusp pattern, the field lines were not a dense. This resulted in less concentration of the plasma electrons. As a result, the $^{12}C^-$ current measured in this configuration was slightly higher: 4.5 μA as opposed to 2.7 μA with the octopole arrangement. Since the plasma electrode was not designed to allow for corrections to its alignment, it was not possible to easily fix this problem. Clearly, precise alignment of future generations of this source is important.

VIII Conclusions

VIII.1 Ion Source Performance

VIII.1.A Summary of Characterization

The behavior of the NRL ion source was characterized by measuring the fundamental plasma parameters, electron temperature (T_e) and electron density (n_e), as various source parameters were varied. These parameters were then used to explain trends in the ion beams extracted from the source. The results of the NRL ion source characterization are summarized Table VIII-1.

Table VIII-1. A Summary of the Characterization of the NRL Ion Source.

Parameter	Effect on T_e	Effect on n_e	Effect on Ion Beam
Increased anode voltage	Increased Linearly	Decreased linearly	Increased output; decreased transmission; increased intensity of atomic species relative to molecular species
Increased cathode bias	Increased linearly	Decreased linearly	Increased output; maintained transmission; increased intensity of atomic species relative to molecular species
Increased filament power	Increased slightly	Increased exponentially	Dramatic increase in beam output
Increased gas pressure	Decreased slightly	Decreased slightly	Decreased beam output; decreased intensity of atomic species relative to molecular species

VIII.1.B Beam Output

Now that the ion source has been studied and characterized, it is important to compare its performance to the existing gas-injection ion sources for AMS. The maximum $^{12}C^-$ beam produced by this ion source was around 4.5 μA. This level of output is comparable to that achieved by the Woods Hole ECR source, however is about an order of magnitude lower than the beam obtained from the Newton Scientific hybrid cesium sputter source. While AMS measurements would be feasible with this level of

beam intensity, the time required to make the measurement would be sufficiently long to make analysis of older samples difficult. However, there are numerous improvements that can be made to this ion source that should greatly improve its performance. These improvements are discussed later in this chapter.

VIII.1.C Mass Efficiency

While the beam intensity produced by this ion source is lower than that desired for routine, high-throughput AMS measurements, a more important performance parameter is the mass efficiency (defined Section VII.2.B). This ion source was able to attain a mass efficiency of over 0.15% which is nearly a factor of 2 higher than the efficiency obtained by the Woods Hole ECR source, but about an order of magnitude lower than the efficiency of the Newton Scientific hybrid cesium-sputter source which has been estimated to be around 1-2%. One promising feature of this ion source was the dramatic increase in efficiency that was observed as the flow rate of gas into the source chamber was decreased. The range of the mass flow controller used for the sample injection manifold was too high to allow investigation of flow rates below about 0.1 sccm N_2, but the results indicate that flow rates below this level would yield a significant increase in mass efficiency. Typical flow rates from a capillary GC are in the range of 1 to 10 mL/min which is higher than the optimal value for the NRL ion source. However, the effluent from a GC is comprised of mostly inert carrier gas. It was shown that optimal mass efficiency for the NRL ion source is achieved when the injected gas is enriched in carbon dioxide. As a result, in order to couple the NRL ion source to the output of a GC, a form of sample enrichment would be necessary as is the case in the interface of a GC to a traditional mass spectrometer. By removing a significant fraction

of the carrier gas, such interfaces reduce the overall flow rate into the ion source which would help maximize the mass efficiency of the NRL ion source.

VIII.1.D Memory Effects

Another important performance parameter is the presence and magnitude of memory effects. This ion source performed well with regard to memory effects. Unlike the Newton Scientific hybrid cesium-sputter source, which showed significant build-up of sample material, this ion source showed very little carry-over following repeated injections of carbon dioxide. However, there was some build-up of material on the inner surface of the source chamber following prolonged (30 min.) sample injection. Given that in practice sample injections from a GC will be very short, this memory effect behavior should not represent a major limitation of this source. The decay time of the ion source was also quite good compared to the Woods Hole ECR source which required several minutes for the ion beam signal to return to baseline. In the NRL ion source, a short (5 second) injection of carbon dioxide required less than 20 seconds were required for the ion beam signal to return to baseline.

VIII.2 Future Work

VIII.2.A Enhanced Cooling

One major limitation to this ion source was the heat load generated by the filament. Since the cooling provided by the fan was insufficient, it was necessary to use thinner filaments than are normally used with this type of ion source. The thin filament required less power to attain the temperature needed for sufficient electron emission to generate a plasma, which kept the chamber temperature at a reasonable level. The drawback to using the thin filament was the noticeably lower filament lifetime at a given

temperature. By upgrading the cooling system thicker filaments could be used which would allow for higher temperatures, thus yielding much higher electron emission. Since the source output and mass efficiency were exponentially related to the electron density within the plasma, better cooling would represent a marked enhancement in the performance of this ion source.

The most effective cooling method would be to reconstruct the source chamber out of copper. A jacket could then be silver soldered around the perimeter of the chamber which would allow a coolant to be flowed around the source. Since the ion source operates at high voltage, the coolant would have to be a very good insulator. In most ion sources Freon is used as the coolant and is circulated by a simple pump fixed with water cooling lines wrapped around the Freon reservoir. This type of system would be capable of delivering several hundred watts of cooling, which would be a factor of 5 or 6 higher than the current cooling system.

VIII.2.B Magnetic Confinement

Another shortcoming of this ion source was the lack of expected performance enhancement when a multi-cusp magnetic confinement field was added. With the multi-cusp field, the source output and mass efficiency actually decreased. It was shown that this result was likely caused by a considerable misalignment between the plasma electrode aperture and the extractor cone aperture. Unfortunately, the current plasma electrode does not allow for easy corrections to the alignment. By reducing the diameter of the plasma electrode and the accompanying insulator, the vertical position could be adjusted by raising and lowering its position within the chamber. However, this would increase the conductance through the ion source and decrease the residence time of

sample molecules, in the source which would decrease the mass efficiency. Additionally, more filament material would be able to migrate from the ion source into the extractor, which might pose a problem with electrical shorts.

A new magnetic confinement strategy, demonstrated by Huck et al (91) and Somocal et al (92), exceeded the performance of a multi-cusp field. Rather than orienting the array of permanent magnets in an alternating pattern to produce the multi-cusp field, the magnets were placed so that the like poles all pointed in the same direction. An ion source using this strategy was able to achieve a factor of forty increase in ion beam intensity. The authors believe this increase is due to better plasma confinement leading to higher plasma electron density. It is important to point out that the ion source they used was operated in positive ion mode with hydrogen. However, if their explanation is correct, the symmetric rather than multi-cusp arrangement should also yield an increase in performance for the NRL ion source, which is intended to operate in negative ion mode and with carbon dioxide. Regardless of which magnetic confinement strategy is used, correct alignment of the plasma electrode with the extractor cone is critical.

Besides the use of magnets to confine the plasma, a magnetic filter can also provide enhancement to source performance. The filter would divide the plasma into a region of high electron temperature and a region of low electron energy. High energy electrons are efficient at increasing the vibrational excitation of sample molecules, which increases the cross section for dissociative attachment by the low energy electrons. By positioning the filter so that the dissociative attachment reaction occurs near the plasma

electrode, the extraction of negative ions from the plasma would be maximized, thus increasing the beam output and mass efficiency of the ion source.

VIII.2.C Cesium Seeding

Introduction of cesium into the plasma is a well documented technique to increase in the performance of negative ion plasma sources even though the exact mechanism is not fully understood. Unfortunately, due to time and funding restrictions, cesium seeding was never employed on this ion source. However, due to the available connection on the ion source, installation of a cesium reservoir would be a simple matter.

VIII.2.D Projected Future

The NRL ion source performance was very promising when compared with the existing gas-fed AMS ion sources. There are also many improvements that could be made to enhance the performance of the ion source. By increasing the cooling capacity to the source, correcting the alignment of the plasma electrode, installing a magnetic filter, and implementing cesium seeding, it is likely that the overall output and mass efficiency could be increased to match or even exceed those of the Newton Scientific hybrid cesium sputter source, while maintaining the desirable absence of memory effects. Such an enhancement would allow this ion source to become a viable alternative to most current AMS ion source that only allow solid samples while still maintaining a high level of sensitivity and precision. The ultimate goal of the NRL ion source would be the coupling to the output of a gas chromatograph, an application for which it seems well suited.

References

1. Tuniz, C. *Accelerator mass spectrometry: ultrasensitive analysis for global science;* CRC Press: Boca Raton, Fla, 1998.

2. Donahue, D. J. *Inter. J. of Mass Spec. and Ion Proc.* **1995**, 143, 235.

3. Tuniz, C.; Zoppi, U.; Barbetti, M. *Proc. of the Inter. School of Phys.* **2004**, 154, 385-406.

4. Clark, B. M.; Mangelson, N. F.; St. Clair, L. L.; Rees, L. B.; Bench, G. S.; Southon, J. R. *The Lichenologist* **2000**, 32(4), 399-403.

5. Frantz, B. R.; Kashgarian, M.; Coale, K. H.; Foster, M. S. *Limnol. Oceanogr.* **2000**, 45(8), 1773.

6. Grabowski, K. S.; Knies, D. L.; Tumey, S. J.; Pohlman, J. W.; Mitchell, C. S.; Coffin, R. B. *Nucl. Inst. & Meth. in Phys. Res. B* **2004**, 223, 435.

7. Hallett, D. J.; Hills, L. V.; Clague, J. J. *Canad. Journ. of Earth Sci.* **1997**, 34(9), 1202.

8. Jull, A. J.; Burr, G. S.; Beck, J. W.; Donahue, D. J.; Biddulph, D.; Hatheway, A. L.; Lange, T. E.; McHargue, L. R. *J. Environ. Radioact.* **2003**, 69(1-2), 3-19.

9. Vance, R. E.; Telka, A. M. *J. Paleolimnol.* **1998**, 19(3), 329.

10. Weissenbok, R. H.; Currie, L. A.; Grollert, C.; Kutschera, W.; Marolf, J.; Priller, A.; Puxbaum, H.; Rom, W.; Steier, P. *Radiocarbon* **2000**, 42(2), 285.

11. Young; Ellis; Ayrton; Hussey; Adamkiewicz *Xenobiotica* **2001**, 31(8/9), 619-632.

12. Buchholz, B.; Arjomand, A.; Dueker, S.; Schneider, P.; Clifford, A.; Vogel, J. *Anal. Biochem.* **1999**, 269(2), 348.

13. Garner, R. C.; Goris, I.; Laenen, A. A. E.; Vanhoutte, E.; Meuldermans, W.; Gregory, S.; Garner, J. V.; Leong, D.; Whattam, M.; Calam, A.; Snel, C. A. W. *Drug Metabolism and Disposition: The Biological Fate of Chemicals* **2002**, 30(7), 823.

14. Lappin, G.; Garner, R. C. *Anal. and Bioanal. Chem.* **2004**, 378(2), 356.

15. Mani, C.; Freeman, S.; Nelson, D.; Vogel, J.; Turteltaub, K. *Toxicol. Appl. Pharmacol.* **1999**, 159(2), 83.

16. Martin, E. A.; Brown, K.; Gaskell, M.; Al-Azzawi, F.; Garner, R. C.; Boocock, D. J.; Mattock, E.; Pring, D. W.; Dingley, K.; Turteltaub, K. W.; Smith, L. L.; White, I. N. H. *Cancer research : the official organ of the American Association for Cancer Research, Inc* **2003**, 63(23), 8461.

17. White, I. N. H.; Brown, K. *Trends Pharmacol. Sci.* **2004**, 25(8), 442.

18. Gove, H. E. *From Hiroshima to the iceman : the development and applications of accelerator mass spectrometry;* Institute of Physics: Bristol, England; Philadelphia, 1999.

19. Zoppi, U.; Hua, Q.; Jacobsen, G.; Sarkissian, G.; Lawson, E. M.; Tuniz, C.; Laurencich Minelli, L. *Nucl. Inst. & Meth. in Phys. Res. B* **2000**, 172, 756.

20. Jacobsen, G. E.; Hotchkis, M. A. C.; Fink, D.; Child, D. P.; Tuniz, C.; Sacchi, E.; Levins, D. M.; Povinec, P. P.; Mulsow, S. *Nucl. Inst. & Meth. in Phys. Res. B* **2000**, 172, 666.

21. Broecker, W. S.; Peng, T. *Nucl. Inst. & Meth. in Phys. Res. B* **2000**, 172, 473.

22. Clapp, E.; Bierman, P.; Nichols, K.; Pavich, M.; Caffee, M. *Quatern. Res.* **2001**, 55(2), 235-245.

23. Shibata, Y.; Tanaka, A.; Yoneda, M.; Uehiro, T.; Kawai, T.; Morita, M.; Kobayashi, K. *Nucl. Inst. & Meth. in Phys. Res. B* **2000**, 172, 827.

24. Marsden, O. J.; Livens, F. R.; Day, J. P.; Fifield, L. K.; Goodall, P. S. *Analyst* **2001**, 126(5), 633-636.

25. Brown, T. A.; Marchetti, A. A.; Martinelli, R. E.; Cox, C. C.; Knezovich, J. P.; Hamilton, T. F. *Nucl. Inst. & Meth. in Phys. Res. B* **2004**, 223, 788.

26. Friedrich, M.; Pilz, W.; Sun, G.; Behrisch, R.; Garcia-Rosales, C.; Bekris, N.; Penzhorn, R. *Nucl. Inst. & Meth. in Phys. Res. B* **2000**, 161, 216.

27. Hui, S. K.; Paul, M.; Berkovits, D.; Boaretto, E.; Ghelberg, S.; Hass, M.; Hershkowitz, A.; Navon, E. *Nucl. Inst. & Meth. in Phys. Res. B* **2000**, 172, 642.

28. Grabowski, K. S.; Knies, D. L.; Hubler, G. K.; Enge, H. A. *Nucl. Inst. & Meth. in Phys. Res. B* **1997**, 123(1-4), 566.

29. Grabowski, K. S.; Knies, D. L.; Deturck, T. M.; Treacy, D. J.; Pohlman, J. W.; Coffin, R. B.; Hubler, G. K. *Nucl. Inst. & Meth. in Phys. Res. B* **2000**, 172, 34.

30. Knies, D. L.; Grabowski, K. S.; Cetina, C.; Hubler, G. K.; Getaneh, M.; Tumey, S. J. *Nuclear Nucl. Inst. & Meth. in Phys. Res. B* **2004**, 223, 72.

31. Knies, D. L.; Grabowski, K. S.; Hubler, G. K.; Enge, H. A. *Nucl. Inst. & Meth. in Phys. Res. B* **1997**, 123(1-4), 589.

32. Knies, D. L.; Grabowski, K. S.; Hubler, G. K.; Treacy, D. J. *AIP conference proceedings* **1997**(392/PT2), 783.

33. DeTurck, T. M.; Treacy, D. J.; Knies, D. L.; Grabowski, K. S. *AIP conference proceedings* **1999**(2), 668.

34. Dahl, D. *SIMION 3D Version 6.0;* 1995.

35. Alton, G. D.; Johnson, M. T. *Nucl. Inst. & Meth. in Phys. Res. A* **1993**, A328(1-2), 202.

36. Alton, G. D.; Mills, G. D.; Dellwo, J. *Rev. Sci. Instrum.* **1994**, 65(6), 2006.

37. Middleton, R.; Klein, J. *Phys. Rev. A* **1999**, 60(5), 3786.

38. Hughey, B. J.; Klinkowstein, R. E.; Shefer, R. E.; Fried, N. A. In *Synthesis and applications of isotopes and isotopically labeled compounds;* Heys, J. R., Melillo, D. G., Eds.; Wiley: Chichester, 1997.

39. Hughey, B. J.; Klinkowstein, R. E.; Shefer, R. E.; Skipper, P. L.; Tannenbaum, S. R.; Wishnok, J. S. *Nucl. Inst. & Meth. in Phys. Res. B* **1997**, 123(1-4), 153.

40. Purser, K. H. *Nucl. Inst. & Meth. in Phys. Res. B* **1994**, 92(1/4), 201.

41. Davis, T. Tutorial of Ion Sources. *http://www.pelletron.com/tutor.htm.*

42. Boaretto, E.; Bryant, C.; Carmi, I.; Cook, G.; Gulliksen, S.; Harkness, D.; Heinemeier, J.; McClure, J.; McGee, E.; Naysmith, P.; Possnert, G.; Scott, M.; Plicht, H. v. d.; Strydonck, M. v. *Antiquity* **2003**, 77(295), 146.

43. Zenin, V. N.; Plicht, J. v. d.; Orlova, L. A.; Kuzmin, Y. V. *Nucl. Inst. & Meth. in Phys. Res. B* **2000**, 172, 745.

44. Mcnichol, A. P.; Schneider, R. J.; von Reden, K. F.; Gagnon, A. R.; Elder, K. L.; Nosams; Key, R. M.; Quay, P. D. *Nucl. Inst. & Meth. in Phys. Res. B* **2000**, 172, 479.

45. Brown, L.; Cook, G. T.; Mackenzie, A. B.; Naysmith, P.; Anderson, R.; Thomson, J.; Nixon, S. *Nucl. Inst. & Meth. in Phys. Res. B* **2000**, 172, 490.

46. Hajdas, I.; Bonani, G.; Thut, J.; Leone, G.; Pfenninger, R.; Maden, C. *Nucl. Inst. & Meth. in Phys. Res. B* **2004**, 223, 267.

47. Kwong, L. L. W.; Povinec, P. P.; Jull, A. J. T. *Radiocarbon* **2004**, 46(2), 133.

48. Morgenroth, G.; Kerscher, H.; Kretschmer, W.; Klein, M.; Reichel, M.; Tully, T.; Wrzosok, I. *Nucl. Inst. & Meth. in Phys. Res. B* **2000**, 172, 416.

49. Ognibene, T. J.; Bench, G.; Vogel, J. S.; Peaslee, G. F.; Murov, S. *Anal. Chem.* **2003**, 75(9), 2192.

50. Pohlman, J. W.; Knies, D. L.; Grabowski, K. S.; Deturck, T. M.; Treacy, D. J.; Coffin, R. B. *Nucl. Inst. & Meth. in Phys. Res. B* **2000**, 172, 428.

51. Hughey, B. J.; Skipper, P. L.; Klinkowstein, R. E.; Shefer, R. E.; Wishnok, J. S.; Tannenbaum, S. R. *Nucl. Inst. & Meth. in Phys. Res. B* **2000**, 172, 40.

52. Liberman, R. G.; Tannenbaum, S. R.; Hughey, B. J.; Shefer, R. E.; Klinkowstein, R. E.; Prakash, C.; Harriman, S. P.; Skipper, P. L. *Anal. Chem.* **2004**, 76(2), 328.

53. Mehl, J. T.; Skipper, P. L.; Wishnok, J. S.; Tannenbaum, S. R.; Hughey, B. J.; Klinkowstein, R. E.; Shefer, R. E. In *Synthesis and applications of isotopes and isotopically labelled compounds;* Voges, R., Pleiss, U., Eds.;;John Wiley: 2000.

54. Donahue, D. J.; Beck, J. W.; Biddulph, D.; Burr, G. S.; Courtney, C.; Damon, P. E.; Hatheway, A. L.; Hewitt, L.; Jull, A. J. T.; Lange, T.; Lifton, N.; Maddock, R.; McHargue, L. R.; O'Malley, J. M.; Toolin, L. J. *Nucl. Inst. & Meth. in Phys. Res. B* **1997**, 123(1-4), 51.

55. Roberts, M. L.; Bench, G. S.; Brown, T. A.; Caffee, M. W.; Finkel, R. C.; Freeman, S. P. H. T.; Hainsworth, L. J.; Kashgarian, M.; McAninch, J. E.; Proctor, I. D.; Southon, J. R.; Vogel, J. S. *Nucl. Inst. & Meth. in Phys. Res. B* **1997**, 123(1-4), 57.

56. Roberts, M. L.; Culp, R. A.; Dvoracek, D. K.; Hodgins, G. W. L.; Neary, M. P.; Noakes, J. E. *Nucl. Inst. & Meth. in Phys. Res. B* **2004**, 223, 1.

57. Steier, P.; Golser, R.; Kutschera, W.; Priller, A.; Vockenhuber, C.; Winkler, S. *Nucl. Inst. & Meth. in Phys. Res. B* **2004**, 223, 67.

58. von Reden, K. F.; Donoghue, J. C.; Elder, K. L.; Gagnon, A. R.; Gerlach, D. S.; Griffin, V. S.; Healy, R. J.; Long, P.; Mcnichol, A. P.; Percy, D.; Roberts, M. L.; Schneider, R. J.; Xu, L.; Hayes, J. M. *Nucl. Inst. & Meth. in Phys. Res. B* **2004**, 223, 50.

59. Hedges, R. E. M.; Ramsey, C. B. *Nucl. Inst. & Meth. in Phys. Res. B* **1994**, 92(1/4), 217.

60. Ramsey, C. B.; Hedges, R. E. M. *Nucl. Inst. & Meth. in Phys. Res. B* **1994**, 92(1/4), 100.

61. Ramsey, C. B.; Hedges, R. E. M. *Nucl. Inst. & Meth. in Phys. Res. B* **1994**, 92(1/4), 105.

62. Ferry, J. A.; Loger, R. L.; Norton, G. A.; Raatz, J. E. *Nucl. Inst. & Meth. in Phys. Res. A* **1996**, 382(1-2), 316.

63. Kim, S.; Schneider, R. J.; von Reden, K. F.; Hayes, J. M.; Wills, J. S. C. *Rev. Sci. Instrum.* **2002**, 73(2), 846.

64. Schneider, R. J.; Kim, S.; von Reden, K. F.; Hayes, J. M.; Wills, J. S. C.; Griffin, V. S.; Sessions, A. L.; Sylva, S. *Nucl. Inst. & Meth. in Phys. Res. B* **2004**, 223, 149.

65. Schneider, R. J.; von Reden, K. F.; Wills, J. S. C.; Diamond, W. T.; Lewis, R.; Savard, G.; Schmeing, H. *Nucl. Inst. & Meth. in Phys. Res. B* **1997**, 123(1-4), 546.

66. Schneider, R. J.; von Reden, K. F.; Hayes, J. M.; Wills, J. S. C. *AIP conference proceedings* **1999**(473), 422.

67. Schneider, R. J.; von Reden, K. F.; Hayes, J. M.; Wills, J. S. C.; Kern, W. G. E.; Kim, S. *Nucl. Inst. & Meth. in Phys. Res. B* **2000**, 172, 252.

68. Jacquot, C.; Pamela, J.; Riz, D.; Belchenko, Y. *Rev. Sci. Instrum.* **1996**, 67(3), 1036.

69. Kuo, T.; Yuan, D.; Jayamanna, K.; McDonald, M. In *Ion Sources;* Ciavola, G., Gammino, S., Eds.; American Institute of Physics: 1998; Vol. 69, pp 959-961.

70. Leitner, M. A.; Gough, R. A.; Leung, K. N.; Rickard, M. L.; Scott, P. K.; Wengrow, A. B.; Williams, M. D.; Wutte, D. C. *Rev. Sci. Instrum.* **1998**, 69(2), 962.

71. Leitner, M. A.; Leung, K. N. *Nucl. Inst. & Meth. in Phys. Res. A* **1999**, 427(1), 250.

72. Leitner, M. A.; Wutte, D. C.; Leung, K. N. *Nucl. Inst. & Meth. in Phys. Res. A* **1999**, 427(1), 242.

73. Leitner, M. A.; Wutte, D. C.; Leung, K. N. *Rev. Sci. Instrum.* **1998**, 69(2), 965.

74. Perkins, L. T.; Vries, G. J. D.; Herz, P. R.; Kunkel, W. B.; Leung, K. N.; Pickard, D. S.; Wengrow, A.; Williams, M. D. *Rev. Sci. Instrum.* **1996**, 67(3), 1057.

75. Saadatmand, K.; Arbique, G.; Hebert, J.; Valicenti, R.; Leung, K. N. *Rev. Sci. Instrum.* **1995**, 66(6), 3438.

76. Takeiri, Y.; Kaneko, O.; Oka, Y.; Tsumori, K.; Asano, E.; Akiyama, R.; Kawamoto, T.; Kuroda, T.; Ando, A. *Rev. Sci. Instrum.* **1996**, 67(3), 1021.

77. Scipioni, L.; Stewart, D.; Ferranti, D.; Saxonis, A. *J. of Vac. Sci. & Tech.B* **2000** 18(6), 3194.

78. Lee, Y.; Gough, R. A.; Kunkel, W. B.; Leung, K. N. In *Micro and Nanofabrication;* Hatzakis, M., Gogolides, E., Eds.; Elsevier: 1998; Vol. 41/42.

79. Lee, Y.; Gough, R. A.; Kunkel, W. B.; Leung, K. N.; Perkins, L. T.; Pickard, D. S.; Sun, L.; Vujic, J.; Williams, M. D.; Wutte, D. *Nucl. Inst. & Meth. in Phys. Res. B* **1996**, 119(4), 543.

80. Lee, Y.; Leung, K. N.; Williams, M. D.; Bruenger, W. H.; Fallmann, W.; Loschner, H.; Stengl, G. In *Particle accelerator;* Luccio, A., MacKay, W., Eds.; IEEE: 1999.

81. Zhang, H. *Ion sources;* Science Press : Springer: New York, 1999.

82. Shirai, M.; Ogasawara, M.; Koishimine, T.; Hatayama, A. *Rev. Sci. Instrum.* **1996**, 67(3), 1085.

83. Holmes, A. J. T. *Rev. Sci. Instrum.* **1982**, 53(10), 1517-6.

84. Holmes, A. J. T.; McAdams, R.; Proudfoot, G.; Cox, S.; Surrey, E.; King, R. *Rev. Sci. Instrum.* **1994**, 64(4), 1153-6.

85. Morishita, T.; Kashiwagi, M.; Hanada, M.; Okumura, Y.; Watanabe, K.; Hatayama, A.; Ogasawara, M. *Proc. of the Symp. on Ultrasonic Elect.* **2001**, 40(7), 4709.

86. Takeiri, Y.; Tsumori, K.; Kaneko, O.; Oka, Y. In *Plasma Physics;* Sugai, H., Hayashi, T., Eds.; Japan Society of Plasma Science and Nuclear Fusion Research: 1996; Vol. 1.

87. Bacal, M.; Bruneteau, A. M.; Deniset, C.; Elizarov, L. I.; Sube, F.; Tontegode, A. Y.; Whealton, J. H. *Rev. Sci. Instrum.* **2000**, 71(2), 1082.

88. Ogasawara, M. *Rev. Sci. Instrum.* **2002**, 73(2), 943.

89. Wolf, B. *Handbook of ion sources;* CRC Press: Boca Raton, Fla, 1995.

90. Roth, A. *Vacuum technology;* Elsevier North-Holland: Amsterdam ; New York; New York, 1982.

91. Huck, H.; Digregorio, D. E.; Fernandez Niello, J. O.; Halac, E. B.; Igarzabal, M.; Orecchia, J.; Reinoso, M. E. *Nucl. Inst. & Meth. in Phys. Res. B* **2001**, 175(1), 772.

92. Somacal, H.; Huck, H.; Di Gregorio, D. E.; Fernandez Niello, J. O.; Igarzabal, M. *Nucl. Inst. & Meth. in Phys. Res. A* **2002**, 490(1), 9.

93. Tumey, S. J.; Mignerey, A. C.; Grabowski, K. S.; Knies, D. L.; Leonhardt, D. *Rev. Sci. Instrum.* **2004**, 75(5), 1910.